# RÉPUBLIQUE ALGÉRIENNE DÉMOCRATIQUE ET POPULAIRE MINISTÈRE DE L'ENSEIGNEMENT SUPÉRIEUR ET DE LA RECHERCHE SCIENTIFIQUE

# FERHAT ABBAS UNIVERSITY – SETIF1 FACULTY OF SCIENCES DEPARTMENT OF PHYSICS

## **THESIS**

Presented for the degree of

# DOCTORATE 3<sup>rd</sup> cycle

In: Physics

Specialty: Theoretical Physics

By: Ayoub TAMIN

#### TITLE

Electron Impact Ionization of atoms and molecules: Role of post collision interaction and distortion effects

Publicly defended on 09/10/2025 before the examination committee: :

Pr Abdelaziz MANSOURI UFA Sétif-1 Chair Pr Nassima Hosni ALLAL **USTHB** Alger Examiner Pr Hocine AOUCHICHE UMM Tizi Ouzou Examiner Pr Kamel BENCHEIKH UFA Sétif-1 Examiner Pr Salim HOUAMER UFA Sétif-1 Supervisor Co-Supervisor Pr Lorenzo Ugo ANCARANI Univ. Lorraine France

Pr Mohamed FELLAH Professor Emeritus (Retired), USTHB Alger Invited

# Acknowledgement

My doctoral research was conducted within the Laboratory of Quantum Physics and Dynamic Systems (LPQSD) at Ferhat Abbas University, Setif 1. The work and results presented in this thesis were carried out under the supervision of Professor Salim Houamer and Professor Lorenzo Ugo Ancarani.

I am deeply grateful to Professor Salim Houamer for proposing such an inspiring research topic and for his patient guidance and continuous support throughout these years, which have been a constant source of motivation. My heartfelt thanks also go to Professor Lorenzo Ugo Ancarani for his valuable guidance, insightful advice, and scientific expertise. His professionalism, kindness, and availability have greatly enriched the quality of this work.

I would also like to express my sincere gratitude to Professor Claude Dal Cappello for his valuable support and enriching discussions, as well as to Professor Abdelaziz Mansouri and Dr. Imene Kada for their encouragement and advice.

My appreciation extends to the members of the jury Professor Kamal Bencheikh, Professor Nassima Hosni Allal, and Professor Hocine Aouchiche — for their constructive feedback and insightful comments as examiners.

Finally, I wish to express my warmest thanks to my colleagues and friends from the LPQSD laboratory Omar Zaidi, Tarek Khatir, Sana Mekhalfa, Imene Khiat, Wafa Sakhraoui, and Maroua Attia for their unwavering support, friendship throughout this journey. Your encouragement and companionship have made these years of research more rewarding and enjoyable. Thank you for the shared moments, your valuable advice.

#### ملخص

تم دراسة تأين الذرات و الجزيئات نتيجة اصطدام الإلكترونات عند مستويات الطاقة المتوسطة و المنخفضة بإستعمال نموذج نظري تحت اسم 3CWZ/M3CWZ في هذا النموذج الذي يأخذ في الاعتبار تأثيرات التبادل و تفاعلات مابعد التصادم، و يتم وصف الالكترونات (الوارد، المتشتت والمطرود) جميعها بواسطة موجة تمثل شحنات تعتمد على المسافة ناتجة عن خصائص الهدف، حيث تقلد هذه الطريقة المتغيرة للشحنة تأثيرات التشويه بشكل تقريبي

الكلمات المفتاحية: تأين، اصطدام الإلكترونات، تأثيرات التشويه

#### Abstract

The electron impact ionization of atoms and molecules at intermediate and low impact energies is investigated using a theoretical approach named 3CWZ/M3CWZ. In this model, which takes into account exchange effects and post collision interaction, the continuum electrons (incident, scattered and ejected) are all described by a Coulomb wave that correspond to distance dependent charges generated from the target properties, this variable charge approach mimics the distortion effects in an approximate manner.

**Keywords:** ionization, electron impact, distortion effects

#### Résumé

L'ionisation par impact d'électrons des atomes et des molécules à des énergies d'impact intermédiaires et faibles est étudiée à l'aide d'une approche théorique nommée 3CWZ/M3CWZ. Dans ce modèle, qui prend en compte les effets d'échange et l'interaction post-collision, les électrons du continuum (incident, diffusé et éjecté) sont tous décrits par une onde de Coulomb correspondant à des charges dépendantes de la distance générées par les propriétés de la cible, cette approche à charge variable imitant de manière approximative les effets de distorsion.

Mots-clés: Ionisation, Impact d'electron, effets de distorsion

# Contents

List of Figures				
Li	ist of	Table	${f s}$	vii
Li	ist of	Acror	nyms	viii
In	trod	uction		1
	Bibl	iograpł	ny	. 4
1	$\operatorname{Th}\epsilon$	eoretic	al Background and Advancements in Ionization Theory	6
	1.1	Scatte	ering Theory	. 7
		1.1.1	Born Approximation	9
		1.1.2	Partial wave analysis	. 10
	1.2	Ioniza	tion theory $\ldots$	. 11
		1.2.1	Description of (e,2e) reaction	. 11
	1.3	Geom	etries and kinematics	. 12
		1.3.1	Experimental techniques	. 12
		1.3.2	Geometries	13
	1.4	Poten	tials and interactions	15
		1.4.1	Coulomb interaction	15
		1.4.2	Distortion Potential	. 17
		1.4.3	Correlation and Polarization:	. 18
		1.4.4	Post Collisional Interactions:	. 18
	1.5	Differ	ential Cross Sections	. 19
		1.5.1	Single Differential Cross Section:	. 19
		1.5.2	Doubly Differential Cross Section:	20
		1.5.3	Triply Differential Cross Section:	20
	1.6	Theor	retical Models	20
		1.6.1	The Plane Wave Born Approximation:	. 20

		1.6.2 The Distorted Wave Born Approximation	21
		1.6.3 Brauner, Briggs, and Klar (BBK) Model:	22
		1.6.4 Three-Body Distorted Wave:	23
		1.6.5 Molecular 3-Body Distorted Wave:	23
		1.6.6 Multicenter Three-Distorted-Wave approach:	26
		1.6.7 The Generalized Sturmian Function Approach (GSF):	27
	1.7	Target wave functions	28
		1.7.1 For atoms	28
		1.7.2 For molecules	29
	1.8	SUMMARY	30
	Bibl	liography	31
2	$Th\epsilon$	e 3CWZ and M3CWZ models	<b>34</b>
	2.1	Introduction	34
	2.2	Asymptotic charge models	35
		2.2.1 1-Coulomb wave 1CW	35
		2.2.2 BBK model	36
	2.3	The concept of variable charge	40
		2.3.1 Variable charge as a distortion approximation	42
	2.4	Previous theoretical models	43
		2.4.1 BBK2CWZ model	43
	2.5	Three coulomb waves with a variable charge model 3CWZ	45
	2.6	Molecular three coulomb waves with a variable charge model M3CWZ	46
	2.7	Conclusion	47
	Bibl	liography	49
3	App	plication on Atoms: Argon and Neon	<b>51</b>
	3.1	Introduction	51
	3.2	Neon	51
		3.2.1 Target wave function and variable charge	52
		3.2.2 Results and Discussion	53
	3.3	Argon	56
		3.3.1 Target wave function and variable charge	57
		3.3.2 Results and discussion	59
	3.4	Conclusion	63
	Bibl	liography	64

4	$\mathbf{Ele}$	ctron-impact ionization of water molecule	<b>65</b>
	4.1	Introduction	65
	4.2	Importance of water molecules	66
	4.3	Theoretical description of the water molecule	66
	4.4	Theoretical model	70
	4.5	Results and discussions	71
	4.6	Ongoing work: developing a hybrid approach	81
		4.6.1 Theory	82
	4.7	Conclusion	84
	Bibl	liography	86
5	Elec	ctron-Impact Ionization of the Methane Molecule	89
	5.1	Introduction	89
	5.2	Theoretical description of the methane molecule	90
		5.2.1 The wave function	90
		5.2.2 Variable charge	91
	5.3	Results and discussions	92
	5.4	Conclusion	98
	Bibl	liography	99
Co	onclu	ısion	100
$\mathbf{A}$	The	e scattering amplitude in BBK model	$\mathbf{A}$

# List of Figures

Scattering process	8
Single ionization process	11
The XZ plane is the scattering plane, which is also referred to as coplanar	
geometry. The incident, scattered and ejected electrons are $e_i$ , $e_s$ and $e_e$	
respectively, the scattering and ejection angles are $\theta_s$ and $\theta_e$ respectively	14
The XY plane is the full-perpendicular plane, same notations as figure 1.3	
for electrons and angles, and $\phi_e$ is ejected electron azimuthal angle	14
The YZ plane is the half-perpendicular plane, same notations as figures 1.3	
and 1.4	14
Scattering or coplanar plane when $\Psi = 0^{\circ}$ , perpendicular plane when $\Psi =$	
90°	15
The long range Coulomb interaction	16
The figure illustrates how the electron wave function is distorted due to the	
inclusion of the short-range potential, particularly at small distances from	
the target	17
Post Collisional Interactions	19
TDCS for the ionization of He as a function of the ejection angle at 500	
· · · · · · · · · · · · · · · · · · ·	
	36
· · · · · · · · · · · · · · · · · · ·	
are black circles	38
	Single ionization process

2.3	TDCS for the ionization of hydrogen as a function of the ejection angle	
	at 250 eV impact energy, The projectile is scattered at an angle $\theta=8^{\circ}$ in	
	coincidence with the ejected electron with $E_e = 5 \text{ eV}$ . Theoretical result is	
	the red solid line (BBK), and the absolute experimental data from [6] are	
	black circles	38
2.4	TDCS for the ionization of Ne $2p^6$ as a function of the ejection angle at	
	500 eV scattering energy, The projectile is scattered at an angle $\theta_s = 6^{\circ}$	
	in coincidence with the ejected electron with $E_e = 37$ , 74 and 205 eV in	
	panels (a), (b), and (c) respectively. Theoretical result is the red solid line	
	(BBK), and the normalized experimental data from $[5]$ are black circles	39
2.5	TDCS for the ionization of Ar $3p^6$ as a function of the ejection angle: (a) at	
	1 keV impact energy, with a scattered angle $\theta_s = 1.2^{\circ}$ in coincidence with	
	the ejected electron of energy $E_e=13$ eV. The right panel (b) a scattering	
	energy of 500 eV, a scattering angle $\theta_s=3^{\circ}$ , and an ejected electron energy	
	of $E_e = 13$ eV. Theoretical results are shown as red solid line (BBK), while	
	the normalized experimental data from $[7,8]$ are represented by black circles.	40
2.6	Partial radial wave functions for the ionization of Ar $3p^6$ as a function of	
	distance r, plotted for $\ell=0$ to $\ell=5$ . The results compare a distorted wave	
	(DW, solid black line) with a spherical Coulomb wave of variable charge	
	(CWZ, solid red line) at an ejection energy of $E=74$ eV	42
2.7	TDCS for the ionization of Ar $3p^6$ as a function of the ejection angle, at	
	a scattering energy of 500 eV, a scattering angle of $\theta = 3^{\circ}$ , and an ejected	
	electron energy of $E_e = 13$ eV. Theoretical results are shown as the red	
	solid line (BBK2CWZ1), dashed blue line (BBK2CWZ0), and dash-dot	
	green line (BBK), while the normalized experimental data from [8] are	
	represented by black circles	44
3.1	Variable charge experienced by the incident electron, the scattered electron,	
9.2	and the ejected electron during the ionization process of Ne $2p$	53
3.2	Absolute TDCS for the ionization of neon 2s at an incident energy of 150eV,	
	as a function of the ejection angle at scattering angles $\theta_s = 15^{\circ}$ for panel	
	(a), and $\theta_s = 5^{\circ}$ for panel (b), and ejected electron energy fixed at $E_e = 10$	
	eV. Theoretical results are represented by a red solid line (3CWZ), the	
	absolute experimental data are shown as black circles from [2]	54

3.3	Absolute TDCS for the ionization of neon $2p$ as a function of the ejection	
	angle at a fixed scattering angle $\theta_s = 6^{\circ}$ for panel (a), and $\theta_s = 5^{\circ}$ for	
	panel (b). The incident and ejected electrons have respective energies: (a)	
	$E_i = 599.6eV$ and $E_e = 74eV$ , (b) $E_i = 150eV$ and $E_e = 10eV$ . Theoretical	
	results are represented by a red solid line (3CWZ), a blue dashed line (DW2-	
	RM) [2], a green dash-dot line (DWBA) [2]. The absolute experimental	
	data are shown as black circles from [2]	55
3.4	TDCS for the ionization of neon $2p$ as a function of the ejection angle at	
	a fixed scattering angle $\theta_s = 20^{\circ}$ , and incident energy 65 eV, and ejection	
	energies (a) $E_e=2$ eV, (b) 4.5 eV, (c) 8 eV . Theoretical results are rep-	
	resented by a red solid line (3CWZ), a blue dashed line (3DW) [3]. The	
	relative experimental data are shown as black circles from [3]	56
3.5	Variable charge experienced by the incident electron , the scattered elec-	
	tron, and the ejected electron during the ionization process of Ar $3p$	58
3.6	TDCS for the ionization of argon 3p as a function of the ejection angle, at	
	fixed scattering and ejected energies 500 eV and 205 eV, respectively. The	
	scattering angles are fixed at (a) $\theta_s = 3^{\circ}$ , (b) $\theta_s = 6^{\circ}$ , and (c) $\theta_s = 9^{\circ}$ .	
	Theoretical results are red solid line (3CWZ), green dash-dot line (DWBA-	
	G), and green dashed line (DWB2-RM). The experimental data shown as	
	black circles from [6], have been normalized for the best visual fit with theory.	60
3.7	Absolute TDCS for the ionization of argon $3p$ as a function of the ejec-	
	tion angle at a fixed scattering angle $\theta_s = 15^{\circ}$ . The incident and ejected	
	electrons have respective energies: (a) $E_i = 200 eV$ and $E_e = 5 eV$ , (b)	
	$E_i = 200eV$ and $E_e = 10eV$ , (c) $E_i = 113.5$ and $E_e = 5eV$ . Theoreti-	
	cal results are represented by a red solid line (3CWZ), a blue dashed line	
	(3DW), a green dash-dot line (DWB2-RM), and a green dash-dot-dot line	
	(DWBA). The experimental data are shown as black circles	60
3.8	Absolute TDCS, shown as cuts of the 3D image, for the ionization of argon	
	$3p$ at an incident energy of $E_i = 195$ eV, plotted as a function of the	
	ejection angles $(\theta_e, \phi_e)$ . The projectile is scattered at angles of 5°, 10°, 15°,	
	and 20°, in coincidence with an ejected electron of $E_e = 10$ eV. The left,	
	center, and right columns correspond to the scattering $(xz)$ plane, half-	
	perpendicular $(yz)$ plane, and full-perpendicular $(xy)$ plane, respectively.	
	Theoretical results are shown as a black solid line (3CWZ) and a red dashed	
	line (DWB2-RM), while experimental data (black circles) are taken from [7].	62

4.1	Molecular orbital diagram of water $H_2O$ (Adapted from ChiralJon , licensed under CC BY 2.0)	67
4.2	Variable charge $Z(r)$ felt by the incident electron (a) and the outgoing	0.
1.2	electrons (b) during the ionization process for the $3a_1$ molecular orbital of	
	$H_2O$	71
4.3	TDCS for electron-impact ionization of molecular orbitals of $H_2O$ at 250 $eV$	
1.0	impact energy. The projectile is scattered at an angle $\theta_s = 15^{\circ}$ in coinci-	
	dence with the ejected electron with energy $E_e = 10 \text{ eV}$ (except for $3a_1$	
	orbital where $E_e = 8 \ eV$ ). Theoretical results of M3CWZ model (red solid	
	line) [29] are compared with the relative scale measurements [13] normal-	
	ized to the M3CWZ calculation in the binary region	72
4.4	The orthogonal planes: the scattering (xz) plane, the half perpendicular	12
7.7	(yz) plane and the full perpendicular (xy) plane	73
4.5	Summed TDCS (presented as cuts of the 3D image) for the ionization of	10
1.0	$1b_1$ and $3a_1$ orbitals of $H_2O$ as a function of the ejection angle at 81 $eV$	
	impact energy. The projectile is scattered at angles $\theta_s = 6^{\circ}$ , or $\theta_s = 10^{\circ}$	
	in coincidence with the ejected electron with $E_e = 5 \ eV$ or $10 \ eV$ . Left-	
	hand column in the full perpendicular (xy) plane. Central column: in the	
	scattering (xz) plane. Right-hand column: in the half perpendicular (yz)	
	plane. Theoretical results are red solid line (M3CWZ) [29], blue dashed line	
	(M3DW as rescaled in [30]) and green dashed-dotted line (MCTDW) [30].	
	The cross normalized experimental data are black circles taken from [14].	
	In the central column (scattering plane), the direction of the momentum	
	transfer $\mathbf{K}$ and its opposite direction $-\mathbf{K}$ are both indicated by an arrow.	75
4.6	Absolute summed TDCS (presented as a cut of the 3D image in the scat-	
	tering $xz$ plane) for the ionization of $1b_1$ and $3a_1$ orbitals of $H_2O$ as a	
	function of the ejection angle at $65 \text{ eV}$ impact energy. The projectile is	
	scattered at angles $\theta_s = 10^{\circ}$ , $15^{\circ}$ , or $20^{\circ}$ from top to bottom, respectively,	
	in coincidence with the ejected electron with energies $E_s = 5$ eV (left-hand	
	column), $E_s = 10$ eV (middle column), and $E_s = 15$ eV (right-hand col-	
	umn). Theoretical results are red solid line (M3CWZ) [29], blue dashed	
	line (M3DW), [15] and green dashed-dotted line (MCTDW-WM). [15] The	
	absolute experimental data are black circles taken from Ref. [15]. The di-	
	rection of the momentum transfer $K$ and its opposite direction $-K$ are	
	both indicated by an arrow.	77
4.7	Same as Fig. 4.6 for the half perpendicular yz plane	78
4.8	Same as Fig. 4.6 for the half perpendicular xy plane	80

4.9	Absolute summed TDCS for the ionization of $1b_1$ and $3a_1$ orbitals of H2O	
	as a function of the ejection angle at 65 eV impact energy. The projectile is	
	scattered $\theta_s = 10^{\circ}$ in coincidence with the ejected electron with $E_e = 5$ eV.	
	Left-hand column: in the full perpendicular (xy) plane; central column: in	
	the scattering (xz) plane; right-hand column: in the half perpendicular (yz)	
	plane. Theoretical results are red solid line (M3CWZ) and dashed blue line	
	(BBK). The absolute experimental data are black circles taken from [15].	81
4.10		
	ergy. The projectile is scattered at an angle $\theta_s = 15^{\circ}$ in coincidence with	
	the ejected electron with energy $E_e = 10 \ eV$ (except for $3a_1$ orbital where	
	$E_e = 8 \ eV$ ). Theoretical results of M3CWZ model (red dashed line), and	
	MDCWZ model (blue solid line) [29] are compared with the relative scale	
	measurements [13] normalized to the M3CWZ calculation in the binary	
	region	83
4.11		
	ization of $1b_1$ and $3a_1$ orbitals of $H_2O$ as a function of the ejection angle	
	at 65 eV impact energy. The projectile is scattered at angles $\theta_s = 10^{\circ}$ , in	
	coincidence with the ejected electron with energy $E_s = 15$ eV. Theoretical	
	results are red dashed line (M3CWZ) [29], blue solid line (MDCWZ). The	
	absolute experimental data are black circles taken from Ref. [15]	84
5.1	Molecular orbital diagram of methane $CH_4$ (Adapted from ChiralJon ,	
	licensed under CC BY 2.0)	90
5.2	Variable charge $Z(r)$ felt by the outgoing electrons (a) and the incident	
	electron (b) during the ionization process for the $1t_2$ molecular orbital of	
	$CH_4$	92
5.3	TDCS for the ionization of the $1t_2$ orbital of $CH_4$ as a function of the	
	ejection angle at 500 $eV$ scattering energy, with scattering angle of $6^{\circ}$ . The	
	ejected electron energy are $12 \ eV$ , $37 \ eV$ , and $74 \ eV$ . Theoretical results	
	are represented by the red solid line (M3CWZ), green dot-dashed line for	
	(cGTOs-dist) [2], blue dashed line for (CKM) [8], and experimental data	
	are shown as black circles [4]. The dot-dashed vertical lines indicates the	
	direction of the momentum transfer ${\bf K}$ and its opposite direction $-{\bf K}.$	93

5.4	TDCS for the ionization of the 1t <sub>2</sub> orbital of CH <sub>4</sub> as a function of the	
	ejection angle at 250 $eV$ impact energy. The scattering angles are 20°, 22.5°,	
	$25^{\circ}$ , $27.5^{\circ}$ , and $30^{\circ}$ . The ejected electron energy is $30~eV$ for the left panel	
	and $50~eV$ for the right panel. Theoretical results are represented by the red	
	solid line (M3CWZ), blue dashed line (M3DW) [9], and green dash-dot line	
	(GSF) [9], while experimental data are shown as black circles from [5]. The	
	dot-dashed vertical line indicates the direction of the momentum transfer ${\bf K}$	94
5.5	TDCS for the ionization of the $1t_2$ orbital of $CH_4$ as a function of the	
	ejection angle at 54.4 $eV$ impact energy, with scattering angles of $20^{\circ}$ , $25^{\circ}$ ,	
	$40^{\circ}$ , and $55^{\circ}$ . The scattered and ejected electron energies are $30~eV$ and	
	$10\ eV,$ respectively. Theoretical results are red solid line (M3CWZ), blue	
	dashed line (M3DW-PA) [6], and green dash-dot line (M3DW-OAMO) [10],	
	while experimental data are shown as black circles [10]	96
5.6	TDCS for the ionization of the $2a_1$ orbital of $CH_4$ as a function of the	
	ejection angle at 500 $eV$ scattering energy, with scattering angle of $6^{\circ}$ .	
	The ejected electron energy are $12~eV$ , $37~eV$ , and $74~eV$ respectively.	
	Theoretical results are represented by the red solid line (M3CWZ), and	
	experimental data are shown as black circles [4]	97

# List of Tables

3.1	Parameters of Clementi's wave functions and ionization energies of the	
	atomic orbitals of the neon atom	52
3.2	Parameters of Clementi's wave functions and ionization energies of the	
	atomic orbitals of the argon atom	57
4.1	Comparison of calculated molecular properties of H <sub>2</sub> O from Moccia [21]	
	with corresponding experimental values. (more deatils in $[22]$ )	69
4.2	Values of coefficients $a_{ij}$ and exponents $\xi_{ij}$ for the molecular orbitals of	
	water as provided by Moccia [23]	69
5.1	Parameters of Moccia's wave functions and ionization energies for the	
	molecular orbitals of $CH_4$ [7]	91

# List of Acronyms

Acronym	Meaning
1CW	One Coulomb Wave
$3 \mathrm{CWZ}$	Three Coulomb Waves with Variable Charge
3DW	Three-Body Distorted Wave
BBK	Brauner, Briggs, and Klar model
BBK1CWZ	BBK with One Variable Charge Coulomb Wave
BBK2CWZ	BBK with Two Variable Charges Coulomb Waves
COLTRIMS	Cold Target Recoil Ion Momentum Spectroscopy
DDCS	Doubly Differential Cross Section
DWBA	Distorted Wave Born Approximation
$\mathbf{EMS}$	Electron Momentum Spectroscopy
$\mathbf{FBA}$	First Born Approximation
GSF	Generalized Sturmian Function
M3CWZ	Molecular Three Coulomb Waves Variable Charge
M3DW	Molecular Three-Body Distorted Wave
MCTDW	Multicenter Three-Distorted-Wave
PCI	Post Collisional Interaction
PWBA	Plane Wave Born Approximation
SDCS	Single Differential Cross Section
TDCS	Triply Differential Cross Section
$\mathbf{P}\mathbf{A}$	Proper Average
OMAO	Orientation-Averaged Molecular Orbital

# Introduction

The interaction of electrons with matter is a central topic in modern physics and chemistry, influencing a wide range of natural phenomena and technological applications. One of the most fundamental processes in this context is the electron-impact ionization, in which an incoming electron collides with an atom or molecule and ejects one or more of its electrons. This process is widespread and plays a critical role in environments ranging from astrophysical plasmas and planetary atmospheres to practical applications such as plasma etching and gas discharges. In particular, the ionization of molecules by electron impact is of great importance, as its significance also extends into biology. Low-energy secondary electrons produced by ionizing radiation are known to damage DNA, making the study of electron-molecule interactions essential for radiation biology and medical physics. Kinematically complete (e,2e) experiments where the energies and momenta of all outgoing particles are measured offer the most detailed view of the ionization reaction through the triple differential cross section (TDCS). However, studies on (e,2e) processes involving molecules are comparatively less common than those involving atomic targets. Experimentally, this is due to challenges like the close spacing of electronic states and the additional contributions from rotational and vibrational excitations. Theoretically, it is difficult to accurately describe multicenter continuum states and the correlated motion of the two outgoing electrons interacting with each other and the residual ion.

In recent decades, significant experimental progress has been made, and with the emergence of new instrumentation, more efficient measurements have become possible. The COLTRIMS reaction microscope (C-REMI) is an imaging device developed to perform (e,2e) measurements with high efficiency [1–3]; with multi-coincidence, high-resolution momentum equipment, a nearly full solid angle TDCS collection is achieved. From the 3D pattern, one may extract simultaneously cuts in the scattering plane as well as out of the scattering plane, offering a more stringent test for theory, and thus gaining further insight into the collision dynamics leading to the development of theoretical models [4]. Measurements of TDCS have been reported for small molecules [5–8] and, more recently, for increasingly complex systems [3,9–14].

On the theoretical side, most models for molecules are based on perturbative methods. Currently, the M3DW (molecular three-body distorted-waves) model [15] is considered to be one of the most powerful approaches for describing the electron-impact ionization of molecular targets. This model uses a full distorted-wave description of the continuum with an isotropic distorting potential and treats post-collision interactions (PCI) exactly at all orders of perturbation theory. In contrast, the recently developed MCTDW (multicenter three-distorted-wave) model [16] derives continuum wave functions from a multicenter potential, and although it treats PCI approximately, this model offers a reasonably accurate description of differential ionization cross sections for a variety of molecules. Although advanced theoretical methods such as the M3DW and MCTDW models exist, they often require heavy computational resources.

The approach explored in this thesis is based on a variable-charge Coulomb wave description for the continuum electrons. Building on previous work, we reintroduce the Three Coulomb Waves with Variable Charge (3CWZ) model for atomic targets, which was discussed in great details in [17], and its new extension, the Molecular Three Coulomb Waves with Variable Charge (M3CWZ) model. These models are used to calculate TDCS for benchmark atomic systems (neon, argon) and, crucially, for biologically relevant molecules (water, methane) across a range of intermediate and low-energy kinematic conditions. Theoretical predictions [18–20] are rigorously compared with available experimental data and with results from other established theoretical approaches. The main goal of this work is to assess the capabilities and limitations of the variable-charge approach, especially the M3CWZ model in reproducing the complex dynamics observed in (e,2e) experiments on molecules. By balancing physical insight with computational feasibility, this research offers a useful theoretical tool for investigating electron-impact ionization in increasingly complex systems, contributing to a better understanding of fundamental collision processes and their applications in various scientific fields.

This thesis is organized as follows:

Chapter 1 provides an overview of the theoretical foundations of scattering and ionization phenomena. It introduces fundamental concepts of scattering theory, details the kinematics and geometries relevant to (e,2e) experiments, discusses the various potentials and interactions involved, defines the different types of differential cross sections, and reviews established theoretical models as well as with methods used for describing target wave functions.

Chapter 2 delves into the core theoretical development of this work: the variable-charge Coulomb wave models. It traces the historical development from simpler asymptotic charge models (1CW, BBK), introduces the concept of variable charge as an approximation for distortion, discusses intermediate models (BBK1CWZ, BBK2CWZ), and

finally presents the detailed formalism of the 3CWZ model for atoms and its extension, the M3CWZ model, for molecules.

Chapter 3 focuses on the application of the 3CWZ model to atomic targets. TDCS calculations are presented for the electron-impact ionization of neon and argon across various kinematic regimes. The results are compared with experimental data and other theoretical predictions (DWBA, DWB2-RM, 3DW) to evaluate the model's performance.

Chapter 4 extends the investigation to molecular targets, specifically focusing on the electron-impact ionization of the water molecule  $(H_2O)$  using the M3CWZ model. The importance of water in contexts like radiobiology is highlighted. TDCS calculations for different molecular orbitals  $(1b_1, 3a_1)$  are presented and compared with recent experimental data obtained using reaction microscopes and with results from the M3DW and MCTDW-WM models, particularly at low impact energies.

Chapter 5 further explores the capabilities of the M3CWZ model by applying it to the electron-impact ionization of the methane molecule  $(CH_4)$ . Calculations for the  $1t_2$  orbital are performed under various kinematic conditions, ranging from intermediate to low impact energies, and compared with experimental data as well as GSF and M3DW (PA and OAMO) results.

Finally, a general conclusion summarizes the main findings of the thesis, discusses the strengths and limitations of the developed models (3CWZ and M3CWZ), and outlines potential directions for future research.

# **Bibliography**

- [1] H. Schmidt-Böcking, J. Ullrich, R. Dörner, and C. L. Cocke. *Ann. Phys.*, **533**:2100134, 2021.
- [2] X. Ren, A. Senftleben, T. Pflüger, A. Dorn, K. Bartschat, and J. Ullrich. J. Phys. B, 83:052714, 2011.
- [3] E. Ali, X. Ren, A. Dorn, C. Ning, J. Colgan, and D. Madison. *Phys. Rev. A*, **93**:062705, 2016.
- [4] A. Tamin, S. Houamer, T. Khatir, L. U. Ancarani, and C. Dal Cappello. J. Chem. Phys., 161:164305, 2024.
- [5] K. Jung, D. Schubert, D. A. L. Paul, and H. Ehrhardt. J. Phys. B, 8:313, 1975.
- [6] L. Avaldi, R. Camilloni, E. Fainelli, and G. Stefani. J. Phys. B, 25:3551, 1992.
- [7] J. Yang and J. P. Doering. Phys. Rev. A, 63:032717, 2001.
- [8] S. Rioual, G. Nguyen Vien, and A. Pochat. Phys. Rev. A, 54:4968, 1996.
- [9] M. J. Hussey and A. J. Murray. J. Phys. B, 38:2965, 2005.
- [10] S. J. Cavanagh and B. Lohmann. J. Phys. B, **32**:L261, 1999.
- [11] L. Avaldi, R. Camilloni, and G. Stefani. Phys. Rev. A, 41:134, 1990.
- [12] L. G. Christophorou and J. K. Olthoff. J. Phys. Chem. Ref. Data, 29:267, 2000.
- [13] X. Ren, T. Pflüger, M. Weyland, W. Y. Baek, H. Rabus, J. Ullrich, and A. Dorn. J. Chem. Phys., 142:174313, 2015.
- [14] S. Jia, J. Zhou, X. Wang, X. Xue, X. Hao, Q. Zeng, Y. Zhao, Z. Xu, A. Dorn, and X. Ren. Phys. Rev. A, 107:032819, 2023.
- [15] J. Gao, D. H. Madison, and J. L. Peacher. J. Chem. Phys., 123:204314, 2005.
- [16] M. Gong, X. Li, S. B. Zhang, S. Niu, X. Ren, E. Wang, A. Dorn, and X. Chen. Phys. Rev. A, 98:042710, 2018.
- [17] K. Bechane. PhD thesis, University Ferhat Abbas Sétif 1, 2024.
- [18] K. Bechane, S. Houamer, T. Khatir, A. Tamin, and C. Dal Cappello. *Phys. Rev. A*, 109:012812, 2024.

- [19] O. Zaidi, A. Mansouri, S. Houamer, A. Tamin, T. Khatir, and C. Dal Cappello. Eur. Phys. J. D, 78:140, 2024.
- [20] A. Tamin, S. Houamer, T. Khatir, L. U. Ancarani, and C. Dal Cappello. J. Chem. Phys., 161:164305, 2024.

# Chapter 1

# Theoretical Background and Advancements in Ionization Theory

Ionization processes are central for understanding many fundamental phenomena in atomic and molecular physics, as they involve the loss of electrons from atoms, ions, or molecules due to interactions with projectiles. Specifically, ionization induced by electron [1,2], positron [3,4], and proton impact [5,6] provides valuable insights into collision dynamics and many-body interactions. The most basic form of these processes is a single ionization, where only one electron is ejected from the target, often through direct impact with the incoming particle; in contrast double ionization, involves the ejection of two electrons. In this thesis, our focus is on understanding and accurately modeling single ionization processes caused by electron impact, by investigating complete experiments known as (e,2e) processes.

The theoretical foundation for studying (e,2e) processes is scattering theory, which provides the necessary mathematical framework to calculate Triple Differential Cross Sections (TDCS), the quantity providing the most detailed information about the ionization dynamics. Since scattering theory has been extensively covered in various theses and quantum mechanics textbooks [7–9], here we will provide only some key elements. We start by exploring the kinematics and geometries relevant to electron impact ionization, and then briefly present the theoretical methods discussed in the subsequent sections, such as the Plane Wave Born Approximation (PWBA) [10] serving as an initial simple approach, and more advanced models like the Distorted Wave Born Approximation (DWBA) [11,12], and Molecular 3-Body Distorted Wave (M3DW) [13].

# 1.1 Scattering Theory

In general terms, scattering can be viewed as a process where two objects begin far apart, move toward each other, collide, and then separate again. Although our focus would not be on the moment of collision itself, but on the outcome it produces, theorists still try to model what occurs between particles at every stage of the process.

When a projectile collides with a target (an atom or molecule in our case), the interaction can be either elastic or inelastic, depending on the kinematics and the energy transfer between the particles involved. In an elastic collision, the particles internal states remain unchanged, only their trajectories are altered; this differs from an inelastic collision which involves a transfer of energy to the target, leading to a different final state [14].

In a scattering process, the number of particles scattered into a given direction is directly related to a key quantity in collision physics: **the differential cross section** (figure 1.1). Denoted  $\frac{d\sigma(\theta,\phi)}{d\Omega}$ , it is defined as the number of particles  $N(\theta,\phi)$  scattered into an element of solid angle  $d\Omega = \sin\theta d\theta d\phi$  in the direction  $(\theta,\phi)$  per unit time and incident flux  $J_{inc}$ :

$$\frac{d\sigma(\theta,\phi)}{d\Omega} = \frac{1}{J_{inc}} \frac{dN(\theta,\phi)}{d\Omega}.$$
(1.1)

By integrating over all possible directions we define the total cross section

$$\sigma = \int \frac{d\sigma}{d\Omega} = \int_0^{\pi} \sin\theta d\theta \int_0^{2\pi} \frac{d\sigma(\theta, \phi)}{d\Omega} d\phi. \tag{1.2}$$

Let us now see how such quantities arise from the fundamental principles of quantum mechanics. The differential cross section is derived from the **scattering amplitude**, which in turn is calculated using the wave function of the system during the scattering process. In quantum scattering theory, the behavior of a projectile interacting with a target is governed by the Schrödinger equation

$$H\Psi = E\Psi \tag{1.3}$$

where the Hamiltonian operator H = K + V includes both the kinetic energy operator  $K = \frac{-\hbar^2}{2m} \nabla^2$  and the potential energy V resulting from their interactions. In the simplest case of scattering between two interacting particles through a potential  $V(\mathbf{r}_1, \mathbf{r}_2)$ , the Hamiltonian is given by

$$H = -\frac{\hbar^2}{2m_1} \nabla_1^2 - \frac{\hbar^2}{2m_2} \nabla_2^2 + V(\mathbf{r_1}, \mathbf{r_2}). \tag{1.4}$$

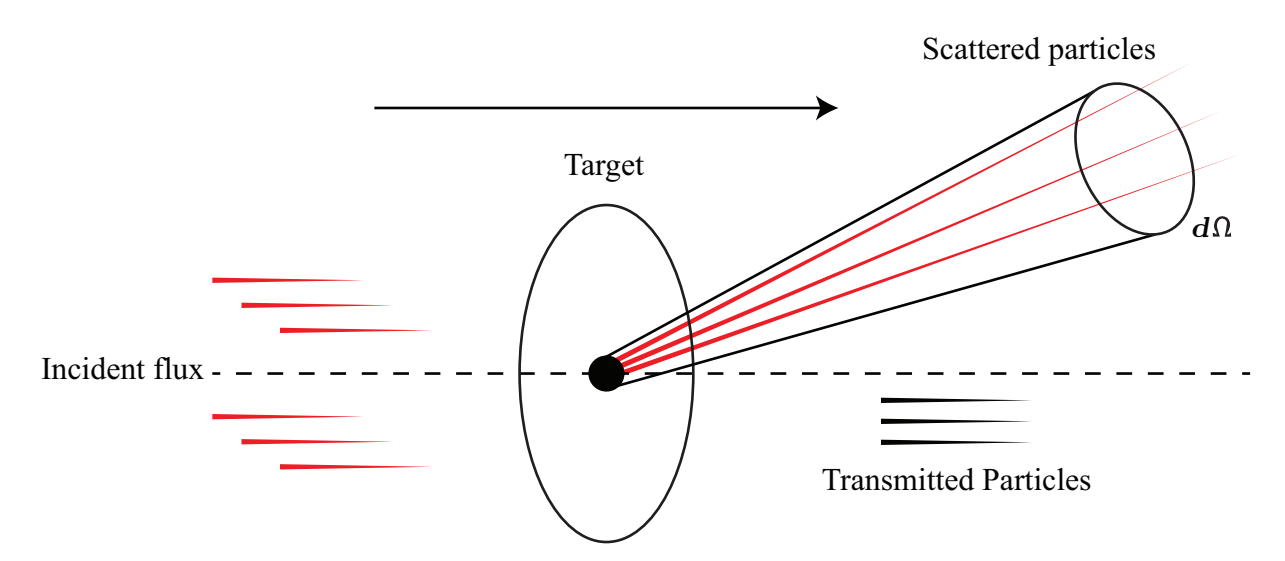


Figure 1.1: Scattering process

This two body problem can be simplified the center of-mass movement (free motion) and a relative motion for a particle with a reduced mass  $\mu$ . The stationary Schrödinger equation is then solved for the relative motion [15]; the solution is can be written as [10]

$$\Psi(\mathbf{r}) = \Psi_{inc}(\mathbf{r}) + \Psi_{sc}(\mathbf{r}) \tag{1.5}$$

where  $\Psi_{inc}(\mathbf{r})$  and  $\Psi_{sc}(\mathbf{r})$  represents the incoming and scattered wave functions respectively. Assuming no prior interaction, the incoming wave function is a plane wave of amplitude C

$$\Psi_{inc}(\mathbf{r}) = Ce^{\mathbf{k}_i \cdot \mathbf{r}} \tag{1.6}$$

for a wave vector  $\mathbf{k_i}$  of the incoming particle. The scattering wave, exhibiting spherical symmetry, is generally written in the form

$$\Psi_{sc}(\mathbf{r}) = f(\theta, \phi) \frac{e^{ik_s r}}{r} \tag{1.7}$$

where  $\mathbf{k}_s$  denotes the wave vector of the scattered particle and  $f(\theta, \phi)$  is the **scattering** amplitude. Now, returning to equation 1.1, we can express the differential cross-section in terms of the scattering amplitude. The number of scattered particles  $dN(\theta, \phi)$  in a solid angle element  $d\Omega$  in the direction  $(\theta, \phi)$ , is given by

$$dN = J_{sc}dS = J_{sc}r^2d\Omega (1.8)$$

so that, equation 1.1 becomes

$$\frac{d\sigma}{d\Omega} = \frac{J_{sc}}{J_{inc}}r^2\tag{1.9}$$

With the wave functions 1.6 and 1.7 we can easily calculate flux densities

$$\mathbf{J}_{inc} = \frac{i\hbar}{2\mu} (\Psi_{inc}(\mathbf{r}) \nabla \Psi_{inc}^*(\mathbf{r}) - \Psi_{inc}^*(\mathbf{r}) \nabla \Psi_{inc}(\mathbf{r}))$$

$$\mathbf{J}_{sc} = \frac{i\hbar}{2\mu} (\Psi_{sc}(\mathbf{r}) \nabla \Psi_{sc}^*(\mathbf{r}) - \Psi_{sc}^*(\mathbf{r}) \nabla \Psi_{sc}(\mathbf{r}))$$
(1.10)

taking the magnitudes of the expressions 1.10, we obtain

$$J_{inc} = \frac{\hbar k_i}{\mu}$$

$$J_{sc} = \frac{\hbar k_s}{\mu r^2} |f(\theta, \phi)|^2$$
(1.11)

where  $\mu$  is the reduced mass, and deduce the differential cross section

$$\frac{d\sigma}{d\Omega} = \frac{k_s}{k_i} |f(\theta, \phi)|^2. \tag{1.12}$$

The scattering amplitude can be expressed as (see [10, 15, 16] for calculation details)

$$f(\theta, \phi) = \frac{-\mu}{2\pi\hbar^2} \int e^{-i\mathbf{k}_s \cdot \mathbf{r}'} V(\mathbf{r}') \Psi_i(\mathbf{r}') d\mathbf{r}' = \frac{-\mu}{2\pi\hbar^2} \langle \Psi_f | V | \Psi_i \rangle$$
 (1.13)

where  $\Psi_i$  and  $\Psi_f$  are the initial and final wave functions respectively.

The calculation of  $f(\theta, \phi)$  is rarely straightforward. The perturbation method, where approximations are made to simplify the problem while providing meaningful results to some extent. One such approximation is the Born approximation, which offers a way to calculate cross sections.

# 1.1.1 Born Approximation

The Born approximation assumes that the interaction potential between the particles involved is relatively weak, it simplifies the problem by treating the influence of the interaction potential as a small adjustment rather than a dominant force. It also lays the groundwork for understanding higher-order effects, as it can be extended through a series of corrections formulated by Born [17]. The solution (1.5) at order "n", written as

$$\Psi_n(\mathbf{r}) = \Psi_{n-1}(\mathbf{r}) - \frac{\mu}{2\pi\hbar^2} \int \frac{e^{i\mathbf{k}(\mathbf{r} - \mathbf{r}_n)}}{|\mathbf{r} - \mathbf{r}_n|} V(r_n) \Psi_{n-1}(\mathbf{r}_n) d\mathbf{r}_n,$$
(1.14)

Equation 1.14 is obtained from the solution at order n-1, called Born series. The first term of this series, known as **the First Born Approximation (FBA)**, which allows for one interaction between the particle and the target

$$\Psi_1(\mathbf{r}) = \Psi_0(\mathbf{r}) - \frac{\mu}{2\pi\hbar^2} \int \frac{e^{i\mathbf{k}(\mathbf{r} - \mathbf{r}_1)}}{|\mathbf{r} - \mathbf{r}_1|} V(r_1) \Psi_0(\mathbf{r}_1) d\mathbf{r}_1$$
(1.15)

where  $\Psi_0(\mathbf{r})$  is the incoming plan wave. The corresponding scattering amplitude in FBA can be expressed as

$$f(\theta,\phi) = -\frac{\mu}{2\pi\hbar^2} \int \frac{e^{i\mathbf{k}(\mathbf{r}-\mathbf{r}_1)}}{|\mathbf{r}-\mathbf{r}_1|} V(r_1) e^{ik_0 r_1} d\mathbf{r}_1.$$
(1.16)

Generally, this approximation is valid only when the incident electron energy is sufficiently higher than that of the target electrons. Alternative methods or workarounds for calculating the scattering amplitude are necessary at lower incident energies.

#### 1.1.2 Partial wave analysis

From this section onwards we will use atomic units, that is to say we set  $\hbar = e = m_e = a_0 = 1$ , for the physical quantities

$$\hbar = \frac{h}{2\pi}; h = 6.6210^{-34} J.s$$

$$e = 1.610^{-19} C$$

$$m_e = 9.109^{-28} g$$

$$a_0 = 0.5310^{-10} m$$
(1.17)

Partial wave analysis [7] is a powerful tool in physics, particularly in scattering theory. It takes advantage of spherically symmetric central potentials U(r) in atomic targets, by separating a wave function into a radial portion and spherical harmonics. For a scattering particle of momentum  $\mathbf{K}$ , the wave function  $\Psi(\mathbf{k}, \mathbf{r})$  satisfies the Schrödinger equation

$$\left[\frac{1}{r^2}\frac{d}{dr}(r^2\frac{d}{dr}) - \frac{L^2}{r^2} - U(r) + 2E\right]\Psi(\mathbf{k}, \mathbf{r}) = 0$$
(1.18)

The partial wave decomposition is given by Eq.(1.19), that is to say an infinite summation

over angular momentum ( $\ell$ ) components of spherical harmonics  $Y_{\ell,m}$  [15]

$$\Psi(\mathbf{k}, \mathbf{r}) = \frac{4\pi}{(2\pi)^{\frac{3}{2}}} \sum_{\ell, m} i^{\ell} e^{i\Delta_{\ell}} \frac{F_{\ell}(k, r)}{kr} Y_{\ell, m}^{*}(\hat{k}) Y_{\ell, m}(\hat{r})$$
(1.19)

where  $\Delta_{\ell}$  represents the phase shift (which is the angular change in solution relative to a plane wave),  $F_l(k,r)$  is the reduced radial wave function,  $Y_{\ell,m}$  are the complex spherical harmonics with and denotes the set of angles.

# 1.2 Ionization theory

When an incident particle collides with a target (atomic or molecular), the interaction can result in the scattering of the incident particle and the ejection of one or more electrons from the target, provided the incident energy is sufficient to overcome the binding energy of one or more electrons in the target's orbitals. When we focus on the single electron ionization, after the collision two electrons are in the continuum, a scattered and an ejected one (Figure 1.2). The target is ionized upon the impact with an incident particle

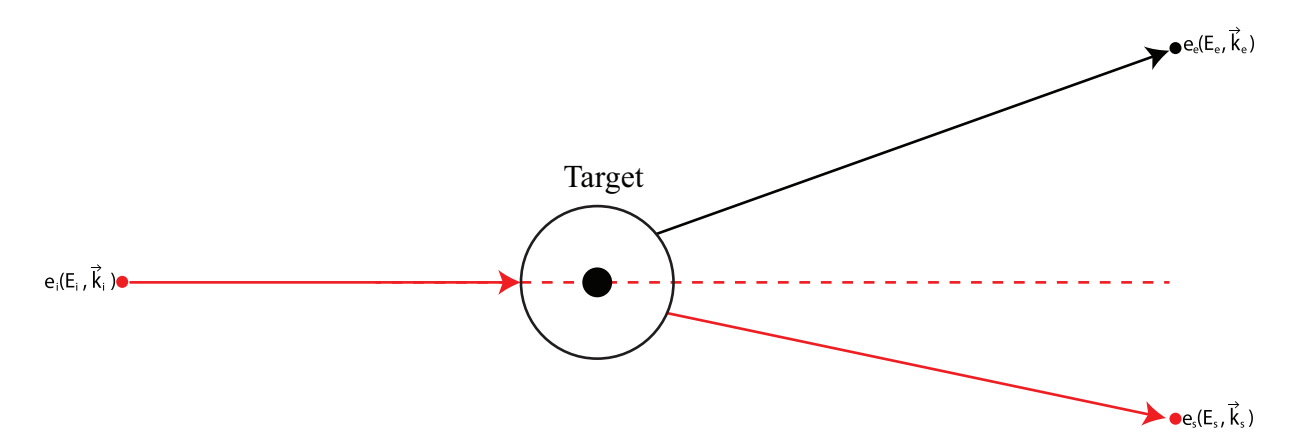


Figure 1.2: Single ionization process

of energy  $E_i$  and momentum  $\mathbf{k_i}$ . The incident particle is scattered and an electron is ejected from the target, with energies  $E_s$ ,  $E_e$  and momentum  $\mathbf{k_s}$ ,  $\mathbf{k_e}$  respectively.

# 1.2.1 Description of (e,2e) reaction

The ionization process known as (e,2e) reaction, can be schematized as

$$e_i^-(E_i, k_i) + A \longrightarrow A^+ + e_s^-(E_s, k_s) + e_e^-(E_e, k_e).$$

It is named (e, 2e) reaction when a kinematically complete (experimental or theoretical) is achieved. The conservation laws for energy and momentum must be satisfied,  $E_i = E_s + E_e + \text{Binding energy}$ , and  $\mathbf{k_i} = \mathbf{k_s} + \mathbf{k_e} + \mathbf{q}$ , where  $\mathbf{q}$  is the momentum of the ion. The momentum transfer (transferred by the scattered electron) defined as  $\mathbf{K} = \mathbf{k_i} - \mathbf{k_s}$ , which determines the type of information we're getting from the scattering process [16]:

- Lower **K** values provide insight into the overall interaction mechanism between the incident electron and the target atom or molecule.
- Higher values of **K** provide more information on the target's structure.

In the next section we outline the different geometries of the scattering setup.

#### 1.3 Geometries and kinematics

Some of the major experimental groups in the field use different techniques and descriptions for the geometries and it is convenient to provide a brief overview.

#### 1.3.1 Experimental techniques

Historically, the first (e,2e) coincidence experiments were conducted and published in 1969 by Ehrhardt et al. [18] and Amaldi et al. [19]. These groundbreaking studies laid the foundation for the field, which later saw significant advancements with the development of powerful techniques

- Electron Momentum Spectroscopy (EMS): EMS is considered a type of microscope that measures the energy and momentum of electrons in atoms and molecules, rather than their position. It is based on a high-energy electron-impact ionization reaction in a symmetric non-coplanar kinematics. This technique allows for the determination of which orbital was ionized and provides valuable information on electron correlations [20].
- Cold Target Recoil Ion Momentum Spectroscopy (COLTRIMS): COLTRIMS is a momentum microscope for scattering experiments, an imaging technique used to study the dynamics of electron-impact ionization in atoms and molecules. It measures the small three-dimensional momentum vectors of target particles produced during these reactions, offering high-resolution data and a  $4\pi$  solid angle. This technique leverages supersonic gas jets to create a cold and localized target, enabling the reconstruction of the complete kinematics of the reaction [21]. In Chapter 4, we

compare our results for the water molecule with experimental data obtained using this technique.

- Recoil-Ion and Electron Momentum Spectroscopy (Reaction Microscopes):

  This technique allows for the measurement of the vector momenta of several ions and electrons resulting from atomic or molecular fragmentation, using Reaction Microscopes. Historically, Reaction Microscopes have evolved from COLTRIMS, and their combination enables the projection of recoil ions and electrons in coincidence. This technique enables the study of the dynamics of multi-particle systems under the influence of external electromagnetic fields, offering kinematically complete studies [22].
- The Manchester (e,2e) Coincidence Experiment: The experiment was developed and used for the first time in 1984 by Hawley-Jones [23], it uses a setup of a (e,2e) spectrometer and a vacuum system to investigate the angular correlations between the scattered electron (after the collision) and the ejected inner-shell electron. The electron gun in the spectrometer can be moved and rotated out of the detection plan, allowing the measurement of electron impact ionization coincidence events in both coplanar and non coplanar geometries as well, at low and high energy kinematics [24].

#### 1.3.2 Geometries

The experimental techniques used in (e,2e) processes use various geometries to measure and calculate the triple differential cross sections (TDCS). Here, we describe the common geometries adopted by two major research groups in this field, namely the Heidelberg laboratory group [25] and the Manchester group [24].

#### 1.3.2.1 The Heidelberg group:

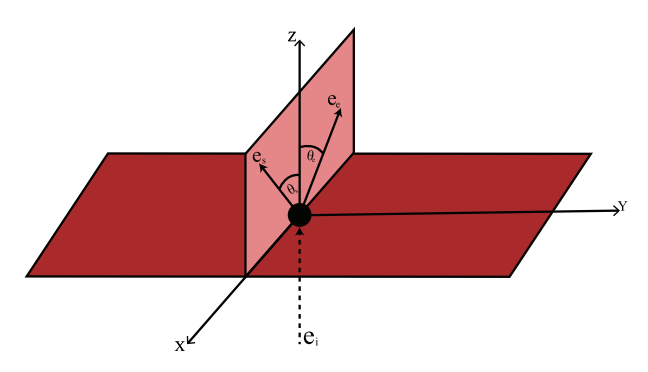
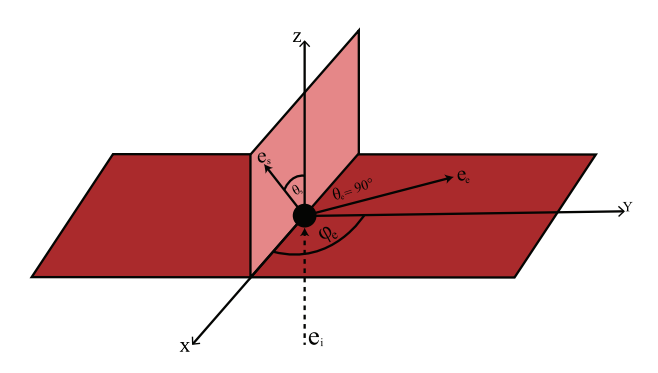
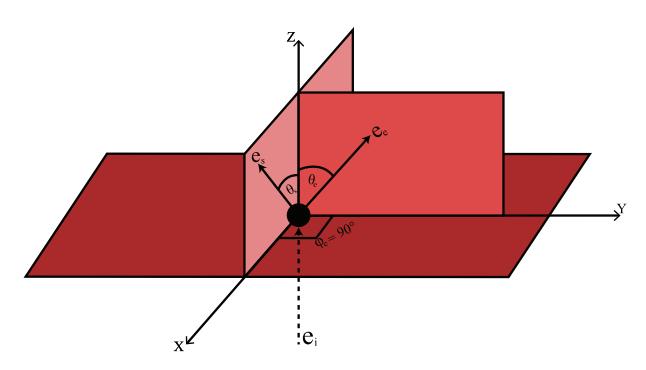


Figure 1.3: The XZ plane is the scattering plane, which is also referred to as coplanar geometry. The incident, scattered and ejected electrons are  $e_i$ ,  $e_s$  and  $e_e$  respectively, the scattering and ejection angles are  $\theta_s$  and  $\theta_e$  respectively.



**Figure 1.4:** The XY plane is the full-perpendicular plane, same notations as figure 1.3 for electrons and angles, and  $\phi_e$  is ejected electron azimuthal angle.



**Figure 1.5:** The YZ plane is the half-perpendicular plane, same notations as figures 1.3 and 1.4.

The Heidelberg laboratory's detectors are fixed on the detection plane and can be moved from one plane to another as needed, while the incident electron beam is always parallel to the Z-direction. The geometries in Figures 1.3, 1.4 and 1.5 are referred to as asymmetric

geometries, where the scattered and ejected electrons do not share equal energy and are detected at different angles. In contrast, in a symmetric geometry both the scattered and ejected electrons have equal energy and are detected at symmetric angles relative to the incident electron beam.

#### 1.3.2.2 The Manchester group:

As shown in Figure 1.6, the geometries are defined differently by the Manchester group, which has the capability to rotate the electron gun through an angle  $\Psi$ . The geometry is referred to as coplanar when  $\Psi = 0^{\circ}$ , and perpendicular when  $\Psi = 90^{\circ}$  (which corresponds exactly to the full-perpendicular plane of the Heidelberg group in figure 1.4).

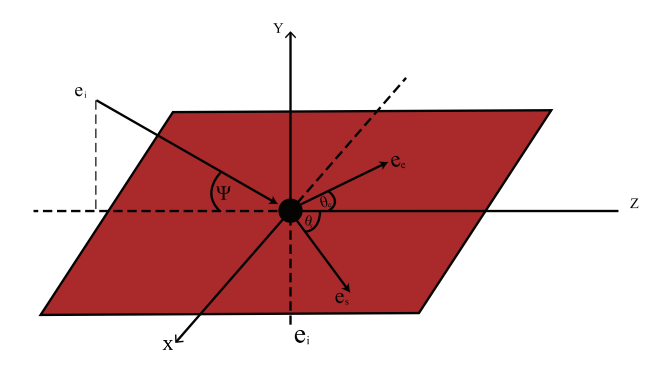


Figure 1.6: Scattering or coplanar plane when  $\Psi = 0^{\circ}$ , perpendicular plane when  $\Psi = 90^{\circ}$ .

Another key difference between the two teams is that, for the Manchester group, the symmetric geometry means that the scattered and ejected electrons are detected at the same angle  $\theta_s = \theta_e = \theta$  and with equal energies  $E_e = E_s = E$ .

#### 1.4 Potentials and interactions

Before, during, and after a collision, numerous interactions occur between the incident electron and the atomic or molecular target.

#### 1.4.1 Coulomb interaction

The first interaction to consider is the long-range Coulomb force between the incident electron and the target, it behaves according to Coulomb's inverse-square law.

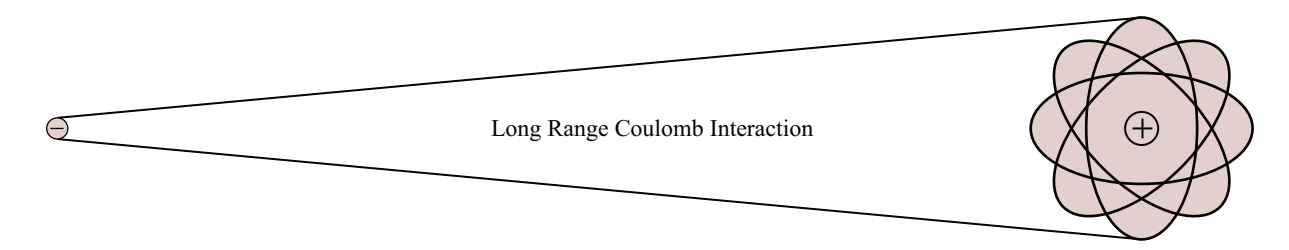


Figure 1.7: The long range Coulomb interaction

#### 1.4.1.1 Coulomb Potential:

In the case where only the Coulomb interaction is considered, the electron Schrödinger equation is given by

$$\left[\nabla^2 + \frac{2Z}{r} + 2E\right]\Psi_{CW}(\mathbf{k}, \mathbf{r}) = 0 \tag{1.20}$$

where  $U_c(r) = -Z/r$  represents the Coulomb potential for a positive charge Z. The solution to equation 1.20 is known as the spherical Coulomb wave, which can be expressed as:

$$\Psi_{CW}(\mathbf{k}, \mathbf{r}) = \frac{4\pi}{(2\pi)^{3/2}} \sum_{l,m} i^{\ell} e^{i\sigma_{\ell}} \frac{F_{\ell}(k, r)}{kr} Y_{\ell,m}^{*}(\hat{k}) Y_{\ell,m}(\hat{r})$$
(1.21)

where  $\sigma_{\ell}$  is the Coulomb phase shift,  $Y_{\ell,m}$  are spherical harmonics, and  $F_{\ell}(k,r)$  is the solution for the differential equation:

$$\left[\frac{d^2}{dr^2} - \frac{\ell(\ell+1)}{r^2} + \frac{2Z}{r} + 2E_\ell\right]F_\ell(k,r) = 0 \tag{1.22}$$

The wave function  $\psi_{CW}$ , describing an electron under the influence of a Coulomb potential, can also be written for an outgoing electron using parabolic coordinates [26]

$$\Psi_{CW}^{-}(\mathbf{k}, \mathbf{r}) = (2\pi)^{-3/2} e^{\eta \pi/2} \Gamma(1+i\eta) e^{i\mathbf{k}\cdot\mathbf{r}} {}_{1}F_{1}(-i\eta, 1, -i(\mathbf{k}\cdot\mathbf{r} + kr))$$
(1.23)

Similarly, for an ingoing electron, the wave function is:

$$\Psi_{CW}^{+}(\mathbf{k}, \mathbf{r}) = (2\pi)^{-3/2} e^{\eta \pi/2} \Gamma(1 - i\eta) e^{i\mathbf{k} \cdot \mathbf{r}} {}_{1} F_{1}(i\eta, 1, i(kr - \mathbf{k} \cdot \mathbf{r}))$$
(1.24)

- Γ: The Gamma function.
- ${}_{1}F_{1}(a,b,z) = \sum_{n=0}^{\infty} \frac{(a)_{n}}{(b)_{n}} \frac{z^{n}}{n!}$ : The confluent hypergeometric function, with  $(a)_{0} = 1$  and  $(a)_{n} = a(a+1) \dots (a+n-1)$ .
- $\eta = Z/k$ : The Sommerfeld parameter, representing the strength of the Coulomb interaction.

#### 1.4.2 Distortion Potential

The distortion potential, in simple terms, is the Coulomb potential with an additional short-range potential

$$V(r) = -\frac{Z}{r} + V_{\rm sr}(r) \tag{1.25}$$

where:

- $-\frac{Z}{r}$  is the Coulomb potential
- $V_{\rm sr}(r)$  is the **short-range potential**, which accounts for residual interactions such as electron repulsion, polarization, or other effects.

This results in a distorted Coulomb wave function. The distortion is more pronounced and significant at small distances from the target, as illustrated in Figure 1.8

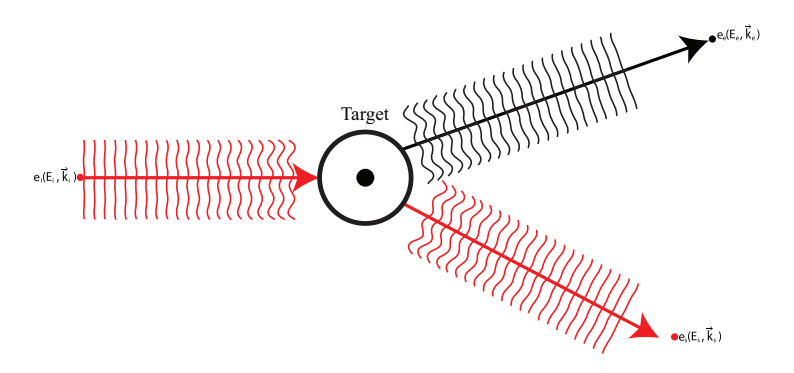


**Figure 1.8:** The figure illustrates how the electron wave function is distorted due to the inclusion of the short-range potential, particularly at small distances from the target.

The solution for the differential equation 1.20 with the new potential is written as

$$\Psi_{DW}(\mathbf{k}, \mathbf{r}) = \frac{4\pi}{(2\pi)^{3/2}} \sum_{l,m} i^{\ell} e^{i(\delta_{\ell} + \sigma_{\ell})} \frac{\chi_{\ell}(k, r)}{kr} Y_{\ell,m}^{*}(\hat{k}) Y_{\ell,m}(\hat{r})$$
(1.26)

where:

- $\chi_{\ell}(k,r)$  is the radial part of the wave function,
- $\delta_{\ell}$  is the additional phase shift introduced by the short-range potential.

The added short-range potential  $V_{\rm sr}(r)$  is responsible for an additional phase shift  $\delta_{\ell}$  in the partial wave expansion of the wave function. This phase shift can be calculated using various numerical methods, as discussed in [27, 28].

#### 1.4.3 Correlation and Polarization:

#### 1.4.3.1 Electrons Correlations

The term "correlation" refers to the interdependence between electrons in a system, where the state of one electron (e.g., position, energy, or spin) directly affects the states of others. These correlations are divided into two types:

- Structural Correlation Refers to interactions between bound and continuum electrons in the target.
- **Dynamic Correlation** The modifications made to the wave functions via Coulomb forces.

#### 1.4.3.2 Correlation-Polarization Potential

A potential that might have a significant effect in the ionization process is the polarization potential. The **correlation-polarization potential** combines an asymptotic dipole polarization with a short-range correlation. For large distances r, the dipole polarization potential can be approximated as [29, 30]:

$$v_p(r) \equiv -\frac{1}{2} \left[ \frac{\alpha_0}{r^4} \right], \tag{1.27}$$

where  $\alpha_0$  is the polarizability of the target. However, this potential cannot be used for small r because it diverges. The short-range correlation potential is defined as [30]:

$$v_{\text{corr}}(r) = \begin{cases} 0.0311 \ln r_s - 0.0584 + 0.00133 \, r_s \ln r_s - 0.0084 \, \ln r_s, & r_s < 1\\ \gamma \frac{\left(1 + \frac{7}{6}\beta_1 \sqrt{r_s} + \frac{4}{3}\beta_2 r_s\right)}{1 + \beta_1 \sqrt{r_s} + \beta_2 r_s}, & r_s \ge 1 \end{cases}$$
(1.28)

where  $\gamma = -0.1423$ ,  $\beta_1 = 1.0529$ ,  $\beta_2 = 0.3334$ , and  $r_s = \left[\frac{3}{4\pi}\rho(r)\right]^{\frac{1}{3}}$ , with  $\rho(r)$  being the radial charge density.

#### 1.4.4 Post Collisional Interactions:

The post-collisional interactions (PCI) illustrated in Figure 1.9 arise from the electrostatic repulsion between the outgoing electrons following a collision event.

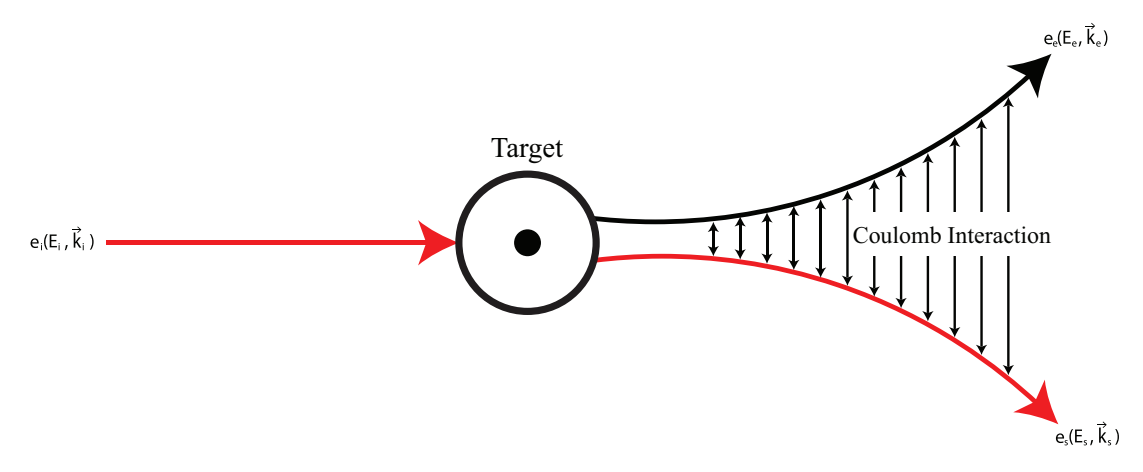


Figure 1.9: Post Collisional Interactions

This PCI may be written as

$$C(\alpha_{01}, \mathbf{k_{se}}, \mathbf{r_{01}}) = e^{\frac{-\pi\alpha_{01}}{2}} \Gamma(1 - i\alpha_{01}) {}_{1}F_{1}(-i\alpha_{01}, 1, -i(k_{se}r_{01} + \mathbf{k}_{se} \cdot \mathbf{r}_{01}))$$
(1.29)

with  $\mathbf{k}_{se} = \frac{1}{2}(\mathbf{k}_s - \mathbf{k}_e)$ , and  $\alpha_{01} = \frac{1}{k_{se}}$ . Due to the complexity of incorporating this term into the final-state in matrix element, some theoretical models opt to use an approximate treatment of PCI rather than accounting for the full Coulomb interaction. Ward and Macek [24] suggested using a multiplying factor for the cross section that is given by

$$C_{e-e} = N_{ee}|_{1}F_{1}(-i\alpha_{01}, 1, -2i(k_{se}r_{01}^{ave}))|^{2},$$
(1.30)

where

$$N_{ee} = \left| e^{\frac{-\pi\alpha_{01}}{2}} \Gamma(1 + i\alpha_{01}) \right|^2 \tag{1.31}$$

is called Gamow factor.

### 1.5 Differential Cross Sections

# 1.5.1 Single Differential Cross Section:

The Single Differential Cross Section (SDCS) measures the probability of a scattering or ionization event with respect to a single variable, such as energy or angle, and is typically notated as  $\frac{d\sigma}{dE}$  or  $\frac{d\sigma}{d\Omega}$ . The SDCS in terms of solid angle  $\Omega_s$  is given by:

$$\sigma^{(1)} = \frac{d\sigma}{d\Omega_s} = \frac{(2\pi)^4}{k_i} \int k_s^2 dk_s dk_1 \, \delta(E_i - E_f) \, |T_{if}|^2$$
 (1.32)

where the transition matrix element squared  $|T_{if}|^2$ , represents the probability amplitude for the scattering process.

The single differential cross section quantifies the likelihood of detecting a particle in a specific direction after the collision [31].

#### 1.5.2 Doubly Differential Cross Section:

The **Doubly Differential Cross Section (DDCS)** describes the probability of a scattering or ionization event as a function of both energy and angle, providing detailed insights into particle interactions. It is usually expressed as  $\frac{d^2\sigma}{dE\,d\Omega}$ 

$$\sigma^{(2)} = \frac{d^2 \sigma}{d\Omega_s dE_e} = \frac{(2\pi)^4}{k_i} k_s k_e \int d\Omega_e |T_{if}|^2$$
 (1.33)

#### 1.5.3 Triply Differential Cross Section:

The **Triply Differential Cross Section (TDCS)** describes the probability of a scattering or ionization event as a function of three variables. In terms of the solid angle of the scattered and ejected electrons,  $\Omega_s$  and  $\Omega_e$  respectively, and the energy of the ejected electron  $E_e$ , it is expressed as:

$$\sigma^{(3)} = \frac{d^3 \sigma}{d\Omega_s \, d\Omega_e \, dE_e} = \frac{(2\pi)^4}{k_i} \, k_s \, k_e \, |T_{if}|^2 \tag{1.34}$$

It provides the most detailed information about the collision process, revealing how the probability distribution depends on the energy and direction of both the scattered and ejected particles.

#### 1.6 Theoretical Models

#### 1.6.1 The Plane Wave Born Approximation:

The Plane Wave Born Approximation (PWBA) is a theoretical framework based on the first born approximation FBA, where the incident and outgoing particles are approximated as plane waves. The final state wave function is given by:

$$\Psi_f(\mathbf{r}_0, \mathbf{r}_1) = \psi_s(\mathbf{r}_0) \,\psi_e(\mathbf{r}_1), \tag{1.35}$$

the position vector of the scattered and ejected electrons are  $\mathbf{r_0}$  and  $\mathbf{r_1}$  respectively. The final wave function is expressed as a product of two plane waves, one describing each

outgoing electron, and  $\psi_s(\mathbf{r}_0) = \frac{1}{(2\pi)^{3/2}} e^{i\mathbf{k}_s \cdot \mathbf{r}_0}$  represents the plane wave of the scattered electron, and  $\psi_e(\mathbf{r}_1) = \frac{1}{(2\pi)^{3/2}} e^{i\mathbf{k}_e \cdot \mathbf{r}_1}$  represents the plane wave of the ejected electron. In this model, the transition matrix element is written as:

$$T_{if} = \langle \psi_s \, \psi_e \, | V(r_0, r_1) | \, \psi_i \, \psi_{target} \rangle \tag{1.36}$$

where  $V(r_0, r_1) = \frac{1}{|\mathbf{r}_0 - \mathbf{r}_1|} - \frac{1}{r_0}$  is the Coulomb potential between the incident electron and the active electron that will be ejected after the collision,  $\phi_i$  is the incident electron plane wave, and  $\psi_{target}$  is the initial bound state wave function of the active electron in the target.

#### 1.6.2 The Distorted Wave Born Approximation

The Distorted Wave Born Approximation (DWBA) is a more advanced theoretical framework used in scattering and ionization processes, where the incident and outgoing particle waves are represented by distorted wave functions 1.26 [11, 12]. Unlike PWBA, DWBA accounts for the interaction between the projectile and the target, providing a more accurate description of the collision dynamics. This is particularly important when the impact energy is not high enough, as the continuum electrons experience the effect of a distortion potential. The initial state wave function  $\Phi_i$  of the system can be written as:

$$\Phi_i = \chi_i \psi_{target} \tag{1.37}$$

where  $\psi_{target}$  is the target wave function, and  $\chi_i$  is the distorted wave function of the incident electron, which can be written from Equation (1.26) as

$$\phi_i(\mathbf{k_i}, \mathbf{r_0}) = \frac{4\pi}{(2\pi)^{3/2}} \sum_{\ell,m} i^{\ell} e^{i(\delta_{\ell} + \sigma_{\ell})} \frac{\chi_l(k_i, r_0)}{k_i r_0} Y_{\ell,m}^*(\hat{k_i}) Y_{\ell,m}(\hat{r_0})$$
(1.38)

The final state of the system is approximated by the product of the ionized target and the wave functions of the two outgoing electrons:

$$\Phi_f \approx \chi_s \, \chi_e \, \psi_{ion} \tag{1.39}$$

where:

- $\chi_s$  is the distorted wave function of the **scattered electron**,
- $\chi_e$  is the distorted wave function of the **ejected electron**,
- $\psi_{ion}$  is the wave function of the ionized target.

The distorted wave functions  $\chi_s$  (scattered electron) and  $\chi_e$  (ejected electron) are given by:

$$\chi_s(\mathbf{k}_s, \mathbf{r}_0) = \frac{4\pi}{(2\pi)^{3/2}} \sum_{\ell,m} i^{\ell} e^{i(\delta_{\ell} + \sigma_{\ell})} \frac{\chi_{\ell}(k_s, r_0)}{k_s r_0} Y_{\ell,m}^*(\hat{k}_s) Y_{\ell,m}(\hat{r}_0), \tag{1.40}$$

$$\chi_e(\mathbf{k}_e, \mathbf{r}_1) = \frac{4\pi}{(2\pi)^{3/2}} \sum_{\ell, m} i^{\ell} e^{i(\delta_{\ell} + \sigma_{\ell})} \frac{\chi_{\ell}(k_e, r_1)}{k_e r_1} Y_{\ell, m}^*(\hat{k}_e) Y_{\ell, m}(\hat{r}_1). \tag{1.41}$$

The transition matrix element in the distorted-wave Born approximation(DWBA) is written as

$$T^{DWBA} = \langle \Phi_f | H - H_0 | \Phi_i \rangle$$

$$= \langle \chi_{proj} \chi_{ejec} \psi_{ion} | V_i - U_i | \chi_i \psi_{target} \rangle$$
(1.42)

where:

- *H* is the total Hamiltonian of the system, describing the full interaction between the projectile, target, and ejected particles.
- $H_0$  is the free Hamiltonian of the system, representing the kinetic energy of the particles in the absence of interactions.
- $V_i$  is the initial interaction potential between the projectile and the target.
- $U_i$  is the spherically symmetric distorting potential of the initial state.

The DWBA approach has proven to be an effective method for calculating the triply differential cross section in electron impact ionization processes. However, the model has limitations due to its poor treatment of PCI, which motivated the development of the three-body distorted wave (3DW) model.

# 1.6.3 Brauner, Briggs, and Klar (BBK) Model:

In 1989 Brauner et al. [32], studied low energy electron-hydrogen ionization. They achieved a good agreement with experiment for light atoms H and He, by using a wave function  $\Psi_f$  (now known as BBK or 3C wave function), which is a product of three Coulomb waves representing the mutual Coulomb interaction between the scattered electron, the ejected electron, and the residual ion, as well as the post-collision interaction

$$\Psi_f \approx \phi_s \, \phi_e \, C_{e-e} \tag{1.43}$$

where

- $\phi_s$ : Represents the Coulomb wave function for the scattered electron.
- $\phi_e$ : Represents the Coulomb wave function for the *ejected electron*.
- $C_{e-e}$ : Represents the Coulomb interaction between the scattered electron and the ejected electron, capturing their mutual post-collision interaction.

The transition matrix element is written as:

$$T^{BBK} = \langle \Psi_f | V | \Psi_i \rangle = \langle \phi_s \, \phi_e \, C_{e-e} | V | \phi_i \, \psi_{target} \rangle$$
 (1.44)

The downside of this BBK model is the neglect of the distortion effect, which should be significant at low energies. A couple of extensions were made to this model to overcome this issue, as we will discuss in the following chapter.

#### 1.6.4 Three-Body Distorted Wave:

In an attempt to address the limitations of the DWBA model and incorporate the PCI like in the BBK model, the **Three-Body Distorted Wave (3DW)** can be regarded as a combination of both models. Therefore the equation 1.43 is modified to give

$$\Phi_f \approx \chi_s \, \chi_e \, C_{e-e} \, \psi_{ion} \tag{1.45}$$

The final state wavefunction 1.45 developed by Prideaux and Madison [33] is called the 3-body distorted wave (3DW) function. Similarly to the DWBA model, the transition matrix element for 3DW is given by

$$T^{3DW} = \langle \chi_s \, \chi_e \, C_{e-e} \, \psi_{ion} \, | V_i - U_i \, | \psi_{\text{target}} \, \chi_i \rangle$$
 (1.46)

The Three-Body Distorted Wave is considered one of the most accurate and sophisticated models for describing electron-atom ionization processes, and it is often used as a benchmark for other theoretical models.

# 1.6.5 Molecular 3-Body Distorted Wave:

The 3DW approximation was later generalized by Gao et al. [13], to be used for molecular targets. Similarly the transition matrix element for the molecular 3-body distorted wave is written as [30]

$$T^{M3DW} = \left\langle \chi_s^{-}(\mathbf{k_s}, \mathbf{r_0}) \, \chi_e^{-}(\mathbf{k_e}, \mathbf{r_1}) \, C_{e-e}(\mathbf{k_{01}}, \mathbf{r_{01}}) \, \psi_{\text{ion}}(\xi, \hat{\mathcal{R}}) \, \middle| H - H_i \, \middle| \psi_{\text{target}}(\xi, \mathbf{r_1}, \hat{\mathcal{R}}) \, \chi_i^{+}(\mathbf{k_i}, \mathbf{r_0}) \right\rangle$$

$$(1.47)$$

where

- $\chi_s^-(\mathbf{k_s}, \mathbf{r_0})$ : The distorted wave function for the scattered electron with momentum  $\mathbf{k_s}$  and position  $\mathbf{r_0}$ .
- $\chi_e^-(\mathbf{k_e}, \mathbf{r_1})$ : The distorted wave function for the ejected electron with momentum  $\mathbf{k_e}$  and position  $\mathbf{r_1}$ .
- $C_{e-e}(\mathbf{k_{01}}, \mathbf{r_{01}})$ : The Coulomb interaction term between the scattered and ejected electrons.
- $\psi_{\text{ion}}(\xi, \hat{\mathcal{R}})$ : The wave function of the residual ion, depending on the coordinates of all the passive target electrons  $\xi$  and the orientation of the molecule  $\hat{\mathcal{R}}$ .
- $H H_i$ : The interaction Hamiltonian, representing the difference between the total Hamiltonian H and the initial-state Hamiltonian  $H_i$ .
- $\psi_{\text{Target}}(\xi, \mathbf{r_1}, \hat{\mathcal{R}})$ : The initial molecular orbital wave function, depending on the coordinates of all the passive target electrons  $\xi$ , the ejected electron's position  $\mathbf{r_1}$ , and the orientation of the molecule  $\hat{\mathcal{R}}$ .
- $\chi_i^+(\mathbf{k_i}, \mathbf{r_0})$ : The distorted wave function for the incident electron with momentum  $\mathbf{k_i}$  and position  $\mathbf{r_0}$ .

In this approximation, the term  $H - H_i$  does not depend on the passive electron coordinates  $\xi$ ; it depends only on the coordinates of the projectile and the active electron,  $\mathbf{r}_0$  and  $\mathbf{r}_1$ , respectively. Integrating over all coordinates of the passive electrons yields the following:

$$\Phi_{Dy}(\mathbf{r}_1, \hat{\mathcal{R}}) = \langle \psi_{\text{ion}}(\xi, \hat{\mathcal{R}}) | \psi_{\text{Target}}(\xi, \mathbf{r}_1, \hat{\mathcal{R}}) \rangle$$
(1.48)

where  $\Phi_{Dy}(\mathbf{r}_1,\hat{\mathcal{R}})$  is the initial bound-state Dyson molecular orbital for the active electron  $\mathbf{r}_1$  for a molecular orientation  $\hat{\mathcal{R}}$ ; it is also called the Dyson orbital. Defining the perturbation to be W [30], equation 1.47 then becomes

$$T^{M3DW}(\hat{\mathcal{R}}) = \left\langle \chi_s^-(\mathbf{k_s}, \mathbf{r_0}) \, \chi_e^-(\mathbf{k_e}, \mathbf{r_1}) \, C_{e-e}(\mathbf{k_{01}}, \mathbf{r_{01}}) \, \middle| W \, \middle| \Phi_{Dy}(\mathbf{r_1}, \hat{\mathcal{R}}) \, \chi_i^+(\mathbf{k_i}, \mathbf{r_0}) \right\rangle \quad (1.49)$$

The triple differential cross section for a particular orientation  $\hat{\mathcal{R}}$  can be written as

$$TDCS^{M3DW}(\hat{\mathcal{R}}) = \frac{1}{(2\pi)^5} \frac{k_s k_e}{k_i} |T^{M3DW}(\hat{\mathcal{R}})|^2$$
 (1.50)

The TDCS for randomly oriented molecules requires some averaging. This can be done through the computationally efficient but wrong method called the **Orientation-Averaged** 

Molecular Orbital (OAMO) method or by performing a proper average of the TDCS over all molecular orientations, which requires significantly more computational time.

#### 1.6.5.1 Proper Orientation Average

The TDCS here is calculated at each orientation and then averaged over all possible orientations [30] as follows

$$TDCS_{PA}^{M3DW} = \frac{\int TDCS(\hat{\mathcal{R}}) d\Omega_{\hat{\mathcal{R}}}}{\int d\Omega_{\hat{\mathcal{R}}}}.$$
 (1.51)

This expression can be expanded further by substituting the detailed form of the TDCS as

$$TDCS_{PA}^{M3DW} = \frac{1}{(2\pi)^5} \frac{k_e k_s}{k_i}$$

$$\frac{\int \left| \int d^3 \mathbf{r}_0 d^3 \mathbf{r}_1 \chi_s^{-*}(\mathbf{k}_s, \mathbf{r}_0) \chi_e^{-*}(\mathbf{k}_e, \mathbf{r}_1) C_{e-e}(\mathbf{k}_{se}, \mathbf{r}_{01}) W(\mathbf{r}_0, \mathbf{r}_1) \Phi_{Dy}(\mathbf{r}_1, \mathbf{R}) \chi_i^{+}(\mathbf{k}_i, \mathbf{r}_0) \right|^2 d\Omega_{\hat{\mathcal{R}}}}{\int d\Omega_{\hat{\mathcal{R}}}}$$
(1.52)

The computational time using this method is extremely high (a point in the TDCS is obtained within a few days) especially for large molecular targets.

#### 1.6.5.2 Orientation-Averaged Molecular Orbital

In this approximation, since the only term that depends on the orientation is the Dyson orbital 1.48, the order of integration is interchanged to (which is not physically correct)

$$TDCS_{OAMO}^{M3DW} = \frac{1}{(2\pi)^5} \frac{k_e k_s}{k_i} \frac{1}{\left| \int d^3 \mathbf{r}_0 d^3 \mathbf{r}_1 \chi_s^{-*}(\mathbf{k}_s, \mathbf{r}_0) \chi_e^{-*}(\mathbf{k}_e, \mathbf{r}_1) C_{e-e}(\mathbf{k}_{se}, \mathbf{r}_{01}) W(\mathbf{r}_0, \mathbf{r}_1) \chi_i^{+}(\mathbf{k}_i, \mathbf{r}_0) \int \Phi_{Dy}(\mathbf{r}_1, \mathbf{R}) d\Omega_{\hat{\mathcal{R}}} \right|^2}{\int d\Omega_{\hat{\mathcal{R}}}}$$

$$(1.53)$$

where the OAMO Dyson wave function is defined as

$$\Phi_{Dy}^{OAMO}(\mathbf{r_1}) = \frac{\int \Phi_{Dy}(\mathbf{r_1}, \hat{\mathcal{R}}) d\Omega_{\mathbf{R}}}{\int d\Omega_{\hat{\mathcal{R}}}}$$
(1.54)

and the final transition matrix element for the OAMO approximation is

$$TDCS_{OAMO}^{M3DW} = \frac{1}{(2\pi)^5} \frac{k_e k_s}{k_i}$$

$$\left| \int d^3 \mathbf{r}_0 d^3 \mathbf{r}_1 \, \chi_s^{-*}(\mathbf{k}_s, \mathbf{r}_0) \, \chi_e^{-*}(\mathbf{k}_e, \mathbf{r}_1) \, C_{e-e}(\mathbf{k}_{se}, \mathbf{r}_{01}) \, V(\mathbf{r}_0, \mathbf{r}_1) \, \chi_i^{+}(\mathbf{k}_i, \mathbf{r}_0) \Phi_{Dy}^{OAMO}(\mathbf{r}_1) \right|^2 \quad (1.55)$$

Equation 1.55 represents a simplified calculation that is performed similarly to that for atoms or a single molecular orientation. This approach significantly reduces computational time but produces much worse and less accurate results compared to averaging over all possible orientations.

### 1.6.6 Multicenter Three-Distorted-Wave approach:

The Multicenter Three-Distorted-Wave (MCTDW) approach builds on the distorted-wave approximation, extending it to account for the multi-center nature of molecular potentials [34]. The final state of the system is written as

$$\Psi_f = \mathcal{F}_e^- \mathcal{F}_s^- \psi_{\text{ion}} \tag{1.56}$$

where  $\mathcal{F}_e^-$ , and  $\mathcal{F}_s^-$  are the ejected and scattered distorted wave functions for a multicentric potential. The transition matrix element for this model is therefore written as:

$$T^{MCTDW}(\Omega) = \left\langle \mathcal{F}_{s}^{-}(\mathbf{k_{s}}, \mathcal{R}_{\Omega}^{-1}\mathbf{r_{0}}) \mathcal{F}_{e}^{-}(\mathbf{k_{e}}, \mathcal{R}_{\Omega}^{-1}\mathbf{r_{1}}) \left| V \right| \Phi_{Dy}(\mathcal{R}_{\Omega}^{-1}\mathbf{r_{1}}) \mathcal{F}_{i}^{+}(\mathbf{k_{i}}, \mathcal{R}_{\Omega}^{-1}\mathbf{r_{0}}) \right\rangle$$
(1.57)

- $\Omega = (\alpha, \beta, \gamma)$  represents the Euler angles,
- $\mathcal{R}_{\Omega}^{-1}$  is the **rotation** of the target,
- $V = \frac{1}{|\mathbf{r}_0 \mathbf{r}_1|} \frac{1}{N} \sum_n \frac{Z_n}{|\mathbf{r}_0 \mathbf{R}_n|}$ , is the interaction potential
- $\Phi_{Dv}$  is the Dyson wave function.
- ullet  $\mathcal{F}_i^+$  is the incident electron's distorted wave function in a multi-center potential.

The treatment for this transition amplitude is similar to DWBA for an atomic target, the main difference being that the electrons distorted wave functions are obtained solving for a multi-center potential. However, it shares the same limitations as DWBA, such as the inadequate treatment of post-collisional interactions.

## 1.6.7 The Generalized Sturmian Function Approach (GSF):

The Generalized Sturmian Functions (GSF) approach for scattering and ionization processes [35, 36] uses a set of basis functions called **Generalized Sturmian functions**, which are solutions to a Sturm-Liouville problem with a specific potential [37]. The ionization process is studied within the GSFs approach using a first-order perturbative approximation through the driven equation [38]

$$(E - \hat{\mathcal{H}}_0)\Psi^1(\mathbf{r_0}, \mathbf{r_1}; \hat{\mathcal{R}}) = \hat{T}(\mathbf{r_0}, \mathbf{r_1}; \hat{\mathcal{R}}), \tag{1.58}$$

where

- E is the total energy of the system,
- $\hat{\mathcal{H}}_0$  is the unperturbed Hamiltonian of the target,
- $\Psi^1(\mathbf{r_0},\mathbf{r_1};\hat{\mathcal{R}})$  is the final state wave function,
- $\Psi^0(\mathbf{r_0}, \mathbf{r_1}; \hat{\mathcal{R}})$  is the inital state wave function,
- $\hat{T}$  is the transition operator, representing the interaction potential  $V(r_0, r_1)$ .

where the initial  $\Psi^0(\mathbf{r_0}, \mathbf{r_1}; \hat{\mathcal{R}})$ , and final  $\Psi^1(\mathbf{r_0}, \mathbf{r_1}; \hat{\mathcal{R}})$  state wave functions are written as

$$\Psi^{0}(\mathbf{r_{0}}, \mathbf{r_{1}}; \hat{\mathcal{R}}) = (2\pi)^{-3/2} e^{i\mathbf{k_{i}} \cdot \mathbf{r_{0}}} \Phi^{0}(\mathbf{r_{1}}; \hat{\mathcal{R}})$$
(1.59)

$$\Psi^{1}(\mathbf{r_{0}}, \mathbf{r_{1}}; \hat{\mathcal{R}}) = (2\pi)^{-3/2} e^{i\mathbf{k_{s}} \cdot \mathbf{r_{0}}} \Phi^{1}(\mathbf{r_{1}}; \hat{\mathcal{R}}). \tag{1.60}$$

The wave function  $\Phi^1(\mathbf{r}_1; \hat{\mathcal{R}})$  for the ejected electron is written as an expansion on GSF  $\mathcal{S}_i^{\ell,E}(r_1)$ 

$$\Phi^{1}(\mathbf{r}_{1}; \hat{\mathcal{R}}) = \frac{1}{r_{1}} \sum_{\ell m} \sum_{i} a_{j}^{(\ell, E)}(\hat{\mathcal{R}}) \mathcal{S}_{j}^{(\ell, E)}(r_{1}) Y_{\ell}^{m}(\hat{r}_{1})$$
(1.61)

where  $a_j^{(\ell,E)}(\hat{\mathcal{R}})$  are the expansion coefficients for a given molecular orientation  $\hat{\mathcal{R}}$ . The detailed mathematical aspects are found in [38]. The transition amplitude for this model is

$$f = \sum_{\ell m} \sum_{j} a_{j}^{(\ell,E)}(\hat{\mathcal{R}}) e^{-i\left(\delta_{\ell} - \ell^{\frac{\pi}{2}}\right)} Y_{\ell}^{m}(\hat{r}). \tag{1.62}$$

Unlike the previous theoretical models, in GSFs approach it is obtained directly from the expansion coefficients  $a_j^{(\ell,E)}(\hat{\mathcal{R}})$ .

# 1.7 Target wave functions

In the previous section, we described how different models treat the final state of the system, specifically the wave functions for the electrons and their interactions. In this section, we briefly summarize the atomic or molecular wave functions used in our calculations.

The complexity of calculations in quantum mechanics increases rapidly with the number of electrons in a system due to the need to account for electron-electron interactions and correlation effects. This complexity increases for large atoms and molecules, necessitating the use of approximations such as the **frozen-core approximation**, which states that only the valence electrons has a significant influence on the properties of a system, while the core electrons are largely unaffected by the external environment. This approach simplifies calculations and accelerates numerical simulations by focusing solely on the valence electrons. In a second approximation, called the **single active electron** (or **single-particle**) **model**, only the wave function of the electron under study is considered [39].

#### 1.7.1 For atoms

The choice of an initial-state wave function is crucial for accurately modeling ionization processes. For example for helium one may use wave functions obtained with the Hartree-Fock approximation [40], with a Configuration Interaction (CI) expansion [41], or within a variational approach that incorporates electron correlation effects. However the situation becomes more computationally expensive for heavier atoms.

In this work, we use Clementi-type Hartree-Fock wave functions [40, 42], where an atomic orbital j is expanded on  $N_j$  Slater-type wave functions, given by:

$$\phi_j(\mathbf{r}) = \sum_{k=1}^{N_j} a_{jk} R_{n_{jk}}^{\xi_{jk}}(r) Y_{l_{jk}, m_{jk}}(\theta, \varphi), \qquad (1.63)$$

where  $n_{ik}$ ,  $l_{jk}$ ,  $m_{jk}$ ,  $\xi_{jk}$ ,  $\beta_{jk}$  are parameters associated with these wave functions, and  $a_{jk}$  denotes the weight of each real atomic component, with

$$R_{n_{jk}}^{\xi_{jk}}(r) = N_{jk} \, r^{n_{jk}-1} e^{-\xi_{jk} \, r} \tag{1.64}$$

and the normalization constant  $N_{jk}$  is defined as:

$$N_{jk} = \frac{(2\xi_{jk})^{n_{jk} + \frac{1}{2}}}{\sqrt{(2n_{jk})!}}. (1.65)$$

#### 1.7.2 For molecules

Molecular Orbital Theory (MOT) is a fundamental concept in quantum chemistry used to describe the electronic structure of molecules. MOT treats electrons as delocalized over the entire molecule. In this approach, atomic orbitals from individual atoms combine to form molecular orbitals that extend across the molecule. These molecular orbitals are classified as bonding, antibonding, or non-bonding [15].

The expansion over a basis of atomic orbitals yields M molecular orbitals:

$$\psi_i = \sum_{j=1}^M C_{ij} \chi_j, \tag{1.66}$$

where:

- $\psi_i$  is the *i*-th molecular orbital, resulting from the linear combination of M atomic orbitals  $\chi_j$  from each atom in the molecule,
- $C_{ij}$  is a scalar that defines the contribution of each atomic orbital  $\chi_j$ .

In the specific case of molecules, specifically for the hydrogen molecule  $H_2$ , several attempts have been made to construct accurate target wave functions: bicentric methods, such as the Hartree-Fock (HF) approach [43] and Configuration Interaction (CI) [44], or monocentric (CI) [45]. We shall use the monocentric (HF) functions.

#### 1.7.2.1 Monocentric functions of Moccia

In the approach proposed by Moccia [46], each molecular wave function is expanded in terms of **centered** Slater-type functions, with a common origin at the heaviest atom, as follows:

$$\phi_i(\mathbf{r}) = \sum_{k=1}^{N_i} a_{ik} \Phi_{n_{ik},\ell_{ik},m_{ik}}^{\xi_{ik}}(\mathbf{r})$$
(1.67)

where  $N_i$  is the number of Slater-type functions used to expand the *i*-th molecular wave function,  $a_{ik}$  and  $\zeta_{ik}$  are coefficients characteristic of the target under consideration, and

$$\Phi_{n_{ik},\ell_{ik},m_{ik}}^{\xi_{ik}}(\mathbf{r}) = R_{n_{ik}}^{\xi_{ik}}(r) S_{\ell_{ik},m_{ik}}(\hat{r})$$
(1.68)

Here:

•  $R_{n_{ik}}^{\xi_{ik}}(r)$  are the radial components given by:

$$R_{n_{ik}}^{\xi_{ik}}(r) = \frac{(2\xi_{ik})^{n+1/2}}{\sqrt{(2n_{ik})!}} r^{n_{ik}-1} e^{-\xi_{ik}r}$$
(1.69)

•  $S_{\ell_{ik},m_{ik}}(\hat{r})$  are the real spherical harmonics, which can be expressed in terms of complex spherical harmonics  $Y_{l,m}$  as follows:

$$\begin{cases}
S_{\ell_k, m_k}(\hat{r}) = \left(\frac{m_{ik}}{2|m_{ik}|}\right)^{\frac{-1}{2}} \left\{ Y_{\ell_{ik} - |m_{ik}|}(\hat{r}) + (-1)^{m_{ik}} \left(\frac{m_{ik}}{|m_{ik}|}\right) Y_{\ell_{ik}|m_{ik}|}(\hat{r}) \right\}, & m_{ik} \neq 0 \\
S_{\ell_{ik}, 0}(\hat{r}) = Y_{\ell_{ik}, 0}(\hat{r}). & m_{ik} = 0 \\
\end{cases}$$
(1.70)

# 1.8 SUMMARY

In this chapter, we presented the basics of scattering and provided an overview of the frameworks and models relevant to electron impact ionization processes. We introduced key approximations such as the Born Approximation and Partial Wave Analysis, setting the stage for understanding electron interactions with atomic and molecular targets. We then explored essential aspects of the theory, including the description of interactions, geometries, and kinematics. Additionally, we examined key concepts of theoretical models, highlighting their applicability and limitations, and showcasing the progression from simpler to more complex frameworks capable of modeling the three-body problem in the electron impact ionization processes. The final section addressed the construction of wave functions for atomic and molecular targets.

# **Bibliography**

- [1] S. Nehaoua, S. Houamer, C. Dal Cappello, M. Chinoune, A. Galstyan, and A. C. Roy. Eur. Phys. J. D, 69(86), 2015.
- [2] M. Chinoune, S. Houamer, and C. Dal Cappello A. Galstyan. J. Phy. B, 49(205201), 2016.
- [3] R. I. Campeanu and C. Whelan. *Atoms*, **9**(33), 2021.
- [4] O. Zaidi, A. Mansouri, S. Houamer, A. Tamin, T. Khatir, and C. Dal Cappello. Eur. Phys. J. D, 78(140), 2024.
- [5] M. E. Rudd, T. V. Goffe, R. D. DuBois, and L. H. Toburen. Phys. Rev. A, 31(492), 1985.
- [6] O. Boudrioua, C. Champion, C. Dal Cappello, and Y. V. Popov. Phys. Rev. A, 75(022720), 2007.
- [7] N. Zettili. Quantum Mechanics: concepts and applications. John Wiley & Sons, UK, 2009.
- [8] C. J Joachain. , Quantum collision theory. North-Holland Physics Publishing: Amsterdam, 1983.
- [9] C. Cohen-Tannoudji, B. Diu, and F. Laloë. *Mécanique Quantique II*. Éditions Hermann, Paris, 1973.
- [10] M. Chinoune. PhD thesis, University Of Science And Technology Houari Boumediene, 2017.
- [11] D. H. Madison and O. Al-Hagan. J. Atomic and Molecular Phys., 2010:367180, 2010.
- [12] D. H. Madison, R. V. Calhoun, and W. N. Shelton. Phys. Rev. A, 16(2):552–562, 1977.
- [13] J. Gao, D. H. Madison, and J. L. Peacher. J. Chem. Phys., 123(20), 2005.
- [14] A. Lupu-Sax. PhD thesis, Harvard University, 1998.
- [15] T. Khatir. PhD thesis, University Ferhat Abbas Sétif 1, 2021.
- [16] K. Bechane. PhD thesis, University Ferhat Abbas Sétif 1, 2024.

- [17] M. Born. Z. Physik, **37**:863–867, 1926.
- [18] H. Ehrhardt, M. Schulz, T. Tekaat, and K. Willmann. Phys. Rev. Lett., 22(3):89–92, 1969.
- [19] U. Amaldi, A. Egidi, R. Marconero, and G. Pizzella. Rev. Sci. Instr., 40(8):1001– 1004, 1969.
- [20] I. E. McCarthy and E. Weigold. Rep. Prog. Phys., 54(6):789, 1991.
- [21] R. Dörner et al. Phys. Rep., **330**:95–192, 2000.
- [22] J. Ullrich, R. Moshammer, A. Dorn, R. Dörner, L. P. H. Schmidt, and H. Schmidt-Böcking. Rep. Prog. Phys., 66(9):1463, 2003.
- [23] T. J. Hawley-Jones, F. H. Read, S. Cvejanovic, P. Hammond, and G. C. King. *J. Phys. B: At. Mol. Opt. Phys.*, **25**(10):2398, 1992.
- [24] A. Sakaamini. PhD thesis, University of Manchester, 2019.
- [25] S.M.F Amami. PhD thesis, Missouri University of Science And Technology, 2017.
- [26] N. F. Mott and H. S. W. Massey. *The Theory of Atomic Collisions*. Oxford University Press, 1965.
- [27] F. Salvat and J. M. Fernández-Varea. Comput. Phys. Commun., 240:165–177, 2019.
- [28] H. Chaluvadi. PhD thesis, Missouri University of Science And Technology, 2015.
- [29] N. T. Padial and D. W. Norcross. Phys. Rev. A, 29(4), 1984.
- [30] E.A. Ali. PhD thesis, Missouri University of Science And Technology, 2017.
- [31] S. Houamer. PhD thesis, University Ferhat Abbas Sétif 1, 2004.
- [32] M. Brauner, J. S. Briggs, and H. Klar. J. Phys. B: At. Mol. Opt. Phys., **22**(14):2265–2287, 1989.
- [33] A. Prideaux and D. H. Madison. Phys. Rev. A, 67(052710), 2003.
- [34] M. Gong, X. Li, S. B. Zhang, S. Niu, X. Ren, E. Wang, A. Dorn, and X. Chen. Phys. Rev. A, 98(042710), 2018.
- [35] G. Gasaneo, L. U. Ancarani, D. M. Mitnik, J. M. Randazzo, A. L. Frapiccini, and F. D. Colavecchia. Adv. Quantum Chem., 67:153–216, 2013.

- [36] C. M. Granados-Castro and L. U. Ancarani. Eur. Phys. J. D, 71(65), 2017.
- [37] G. B. Arfken and H. J. Weber. *Mathematical Methods for Physicists*. Academic Press Inc., Orlando, FL, 1995.
- [38] C. M. Granados Castro. PhD thesis, Université de Lorraine, Metz, 2016.
- [39] O. Zaidi. PhD thesis, University Ferhat Abbas Sétif 1, 2024.
- [40] E. Clementi and C. Roetti. At. Data Nucl. Data Tables, 14:177, 1974.
- [41] J. Mitroy, I. E. McCarthy, and E. Weigold. J. Phys. B: At. Mol. Opt. Phys., 18:4149, 1985.
- [42] A. Szabo and N. S. Ostlund. *Modern Quantum Chemistry: Introduction to Advanced Electronic Structure Theory*. Dover Publications, Inc., 1996.
- [43] MC. Dal Cappello, C. Dal Cappello, C. Tavard, and M. Ch'erid A. Lahmam-Bennani A. Duguet. *J. Physique*, **50**:207, 1989.
- [44] N. Lahmidi and B. Joulakian. J. Phys. B: At. Mol. Opt. Phys., 38:51–60, 2005.
- [45] S. Hagstrom and H. Shull. J. Chem. Phys., **30**:1314, 1559.
- [46] R. Moccia. J. Chem. Phys., **40**:2164, 1964.

# Chapter 2

# The 3CWZ and M3CWZ models

# 2.1 Introduction

Building upon the foundational principles of ionization theory discussed in Chapter 1, this chapter provides a historical overview of our research team contributions, spanning from early basic models to more advanced frameworks, such as the **Three Coulomb Waves with a Variable Charge (3CWZ)** model, which was initially proposed by our research group first for electron impact ionization (Bechane et al. [1]) and subsequently extended to positron impact ionization (Zaidi et al. [2]), as well as its molecular extension, the Molecular Three Coulomb Waves with a Variable Charge (M3CWZ) model (Tamin et al. [3]).

We begin this chapter by describing two asymptotic charge models, specifically the **One-Coulomb Wave (1CW)** and **BBK**. These models were essential during the early stages of my thesis for understanding the main features of (e,2e) reactions. We subsequently explore the concept of variable charge, which uses approximate distortion effects to address the short-range interactions between the ionized electron and the target. By incorporating variable charges, the **BBK** variable charge approach serves as a precursor to more accurate models such as **BBK1CWZ** and **BBK2CWZ**. These approaches laid the foundation for the **3CWZ** and **M3CWZ** models.

Finally, we present the theoretical framework for the **3CWZ** model and extend it to molecular systems through **M3CWZ**. This molecular adaptation incorporates additional complexities inherent to molecular targets, such as anisotropic potentials and multi-center effects.

# 2.2 Asymptotic charge models

#### 2.2.1 1-Coulomb wave 1CW

In this model, only the interaction between the ejected electron and the residual ion (with charge Z) is taken into account. The Schrödinger equation for this system is written as:

$$\left(-\frac{1}{2}\nabla^2 - \frac{Z}{r}\right)\Psi_{CW}(\mathbf{r}) = E_e\psi(\mathbf{r})$$
(2.1)

where  $E_e = \frac{k_e}{2}$  is the energy of the ejected electron of momentum  $\mathbf{k_e}$ . The solution to this equation is a Coulomb wave which can be expressed in spherical  $\Psi_{CW}$  and parabolic coordinates  $\Phi_{CW}$  (see chapter one 1.4.1.1)

$$\begin{cases}
\Psi_{CW}^{-}(\mathbf{k_e}, \mathbf{r}) = \frac{4\pi}{(2\pi)^{3/2}} \sum_{l,m} i^{\ell} e^{i\sigma_{\ell}} \frac{F_{\ell}(k_e, r)}{k_e r} Y_{\ell,m}^{*}(\hat{k}) Y_{\ell,m}(\hat{r}) \\
\Phi_{CW}^{-}(\mathbf{k_e}, \mathbf{r}) = \frac{e^{\pi\alpha/2}}{(2\pi)^{3/2}} \Gamma(1 + i\alpha) e^{i\mathbf{k_e} \cdot \mathbf{r}} {}_{1} F_{1}(-i\alpha, 1, -i(k_e r + \mathbf{k_e} \cdot \mathbf{r})),
\end{cases} (2.2)$$

where  $\alpha = Z/k$ . For Z = 0, the wave function  $\Psi_{CW}^-$  reduces to a plane wave. The incident and scattered electrons are described by plane waves, and the ejected electron is a Coulomb wave (in our theoretical framework we carry out integrations analytically, for that we use the parabolic coordinates for the Coulomb wave), and the scattering amplitude is

$$T_{if} = \langle \Phi_{CW} \psi_s | V | \psi_i \psi_{nlm} \rangle \tag{2.3}$$

where  $\psi_{i/s} = \frac{1}{(2\pi)^{\frac{3}{2}}} e^{i\mathbf{k}_{i/s}\mathbf{r}_0}$ , are the plane waves for the scattered and incident electrons, and  $V = -\frac{1}{r_0} + \frac{1}{|\mathbf{r_0} - \mathbf{r_1}|}$  is the Coulomb potential. Integrating over  $\mathbf{r_0}$  yields to (see details in [4])

$$T_{if} = \frac{4\pi}{K^2} \langle \Phi_{CW} | e^{i\mathbf{K} \cdot \mathbf{r}} - 1 | \psi_{nlm} \rangle, \qquad (2.4)$$

where  $\psi_{nlm}$  is the initial target bound state wave function of the electron, and **K** is the transfer momentum.

The 1CW model provides a simplified framework which presents several limitations:

- i) It is not supposed to be valid for low or intermediate collision energies;
- ii) The PCI is neglected;
- iii) It is not supposed to be valid for complex targets, since short range interactions are neglected.

However, in high-energy regimes and for simple targets like hydrogen or helium, the 1CW approximation is effective.

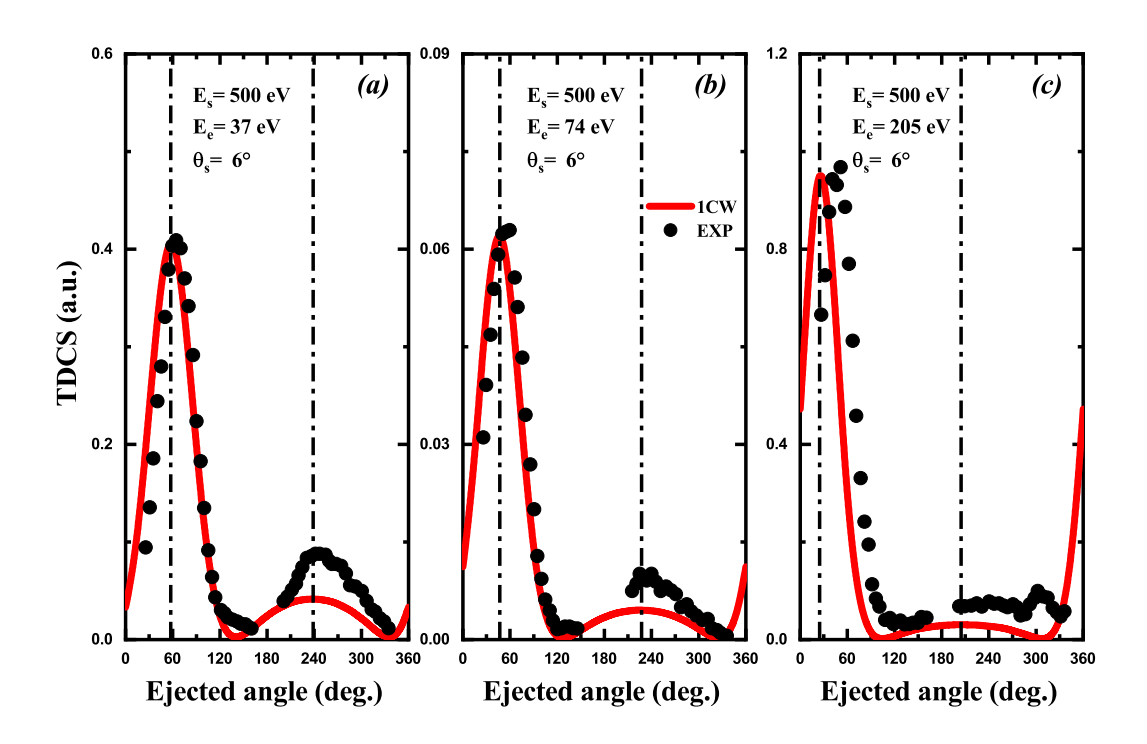


Figure 2.1: TDCS for the ionization of He as a function of the ejection angle at 500 eV scattering energy, The projectile is scattered at an angle  $\theta = 6^{\circ}$  in coincidence with the ejected electron with  $E_2 = 37$ , 74 and 205 eV in panels (a), (b), and (c) respectively. Theoretical result is the red solid line (1CW), and the normalized experimental data from [5] are black circles.

An example is shown in Figure 2.1, where the 1CW TDCS for He ionization is compared to the experimental data from [5] for the ejection energies 37, 74, and 205 eV with a scattering angle  $\theta_s = 6^{\circ}$ , where the experimental data is normalized to theory for best visual fit. The model successfully reproduces both the binary and standard recoil peaks, with a noticeable angular shift toward smaller scattering angles at 205 eV ejection energy.

#### 2.2.2 BBK model

As discussed in Chapter 1 (Section 1.6), the BBK model was among the first to incorporate PCI exactly. In this section, we explore cases where it performed exceptionally well and others where its limitations became evident. The final state is described by three Coulomb waves representing the interaction of the scattered and ejected electrons with the residual ion, as well as PCI between these two electrons

$$\Psi_f = \Phi_{CW}(\mathbf{k}_s, \mathbf{r}_0) \,\Phi_{CW}(\mathbf{k}_e, \mathbf{r}_1) \,C(\alpha_{01}, \mathbf{k}_{se}, \mathbf{r}_{01}), \tag{2.5}$$

with PCI represented as

$$C(\alpha_{01}, \mathbf{k_{se}}, \mathbf{r_{01}}) = e^{\frac{-\pi\alpha_{01}}{2}} \Gamma(1 - i\alpha_{01})_1 F_1(-i\alpha_{01}, 1, -i(k_{se}r_{01} + \mathbf{k}_{se} \cdot \mathbf{r_{01}}))$$
(2.6)

where  $\mathbf{k}_{se} = \frac{1}{2}(\mathbf{k}_s - \mathbf{k}_e)$ , and  $\alpha_{01} = \frac{1}{2k_{se}}$ .

The transition matrix element is

$$T_{if} = \left\langle \Psi_f \left| \frac{1}{r_{01}} - \frac{1}{r_0} \right| \Psi_i \right\rangle \tag{2.7}$$

with  $\Psi_i = e^{i\mathbf{k_i}\cdot\mathbf{r_0}}\psi_{nlm}$ , and explicitly written as:

$$T_{if} = \int \int \Phi_{CW}^*(\mathbf{k}_s, \mathbf{r}_0) \, \Phi_{CW}^*(\mathbf{k}_e, \mathbf{r}_1) \, C^*(\alpha_{01}, \mathbf{k}_{se}, \mathbf{r}_{01}) \left( \frac{1}{r_{01}} - \frac{1}{r_0} \right) e^{i\mathbf{k}_i \cdot \mathbf{r}_0} \, \psi_{nlm}(\mathbf{r}_1) \, d\mathbf{r}_0 \, d\mathbf{r}_1$$

$$(2.8)$$

using a Fourier transform scheme, equation (2.8) becomes (see details in Appendix A)

$$T_{if} = \frac{1}{(2\pi)^3} \lim_{\substack{\lambda \to 0 \\ \gamma \to 0}} \int \left[ \int \phi_c^*(\mathbf{k}_e, \mathbf{r}_1) \psi_{nlm}(\mathbf{r}_1) d\mathbf{r}_1 \int \phi_c^*(\mathbf{k}_s, \mathbf{r}_0) e^{i(\mathbf{k}_i + \mathbf{p}) \cdot \mathbf{r}_0} e^{-\gamma r_0} d\mathbf{r}_0 \right]$$

$$\times \int (2\pi)^{-3/2} \frac{C^*(\alpha_{01}, \mathbf{k}_{se}, \mathbf{r}'_{01})}{r'_{01}} e^{i(\mathbf{k}_{01} - \mathbf{p}) \cdot \mathbf{r}'_{01}} e^{-i\mathbf{k}_{se} \cdot \mathbf{r}'_{01}} e^{-\lambda r'_{01}} d\mathbf{r}'_{01}$$

$$- \int \phi_c^*(\mathbf{k}_e, \mathbf{r}_1) \psi_{nlm}(\mathbf{r}_1) d\mathbf{r}_1 \int \frac{\phi_c^*(\mathbf{k}_s, \mathbf{r}_0)}{r_0} e^{i(\mathbf{k}_i + \mathbf{p}) \cdot \mathbf{r}_0} e^{-\gamma r_0} d\mathbf{r}_0$$

$$\times \int (2\pi)^{-3/2} C^*(\alpha_{01}, \mathbf{k}_{se}, \mathbf{r}'_{01}) e^{i(\mathbf{k}_{se} - \mathbf{p}) \cdot \mathbf{r}'_{01}} e^{-i\mathbf{k}_{se} \cdot \mathbf{r}'_{01}} e^{-\lambda r'_{01}} d\mathbf{r}'_{01} d\mathbf{r}'_$$

#### 2.2.2.1 Application to Hydrogen and Helium:

Calculations of the TDCS have been performed for electron-impact ionization of hydrogen and helium under specific kinematic conditions. For hydrogen, the TDCS was calculated at an impact energy of 250 eV, with the projectile scattered at an angle of  $\theta_s = 8^{\circ}$  in coincidence with an ejected electron energy of  $E_e = 5$  eV. For helium, calculations were conducted at an impact energy of 500 eV, with a projectile scattering angle of  $\theta_s = 6^{\circ}$  and an ejected electron energy of 74 eV. Results obtained from the BBK model are presented in Figures 2.2 and 2.3 and compared with the experimental data from [5], and [6] respectively.

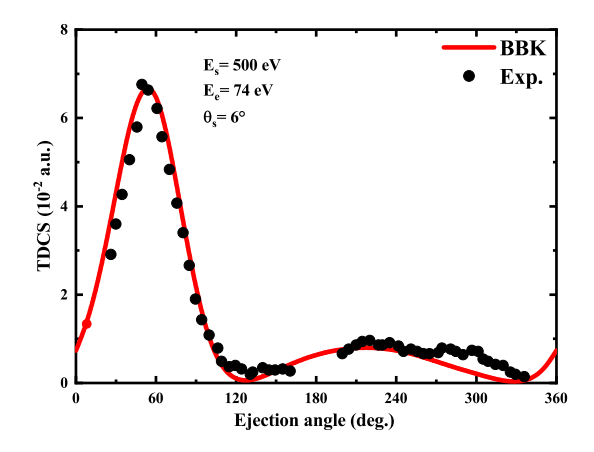


Figure 2.2: TDCS for the ionization of He  $1s^2$  as a function of the ejection angle at 500 eV scattering energy, The projectile is scattered at an angle  $\theta=6^{\circ}$  in coincidence with the ejected electron with  $E_e=74~eV$ . Theoretical result is the red solid line (BBK), and the normalized experimental data from [5] are black circles.

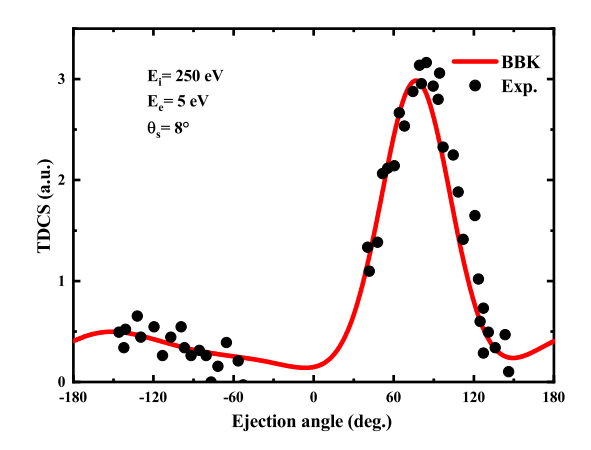


Figure 2.3: TDCS for the ionization of hydrogen as a function of the ejection angle at 250 eV impact energy, The projectile is scattered at an angle  $\theta = 8^{\circ}$  in coincidence with the ejected electron with  $E_e = 5 \ eV$ . Theoretical result is the red solid line (BBK), and the absolute experimental data from [6] are black circles.

Figures 2.2 and 2.3 demonstrate the capability of the BBK model to reproduce TDCS measurements on light targets. In the He case (Fig. 2.2), for these asymmetric coplanar geometries, the BBK calculation exhibits a clear double-peak structure in the directions of  $\mathbf{K}$  and  $-\mathbf{K}$ , where  $\mathbf{K} = \mathbf{k_i} - \mathbf{k_s}$  is the momentum transfer. The theoretical prediction shows very good agreement with the experimental data across the entire angular range. Similarly, for hydrogen at  $E_i = 250\,\text{eV}$  and  $E_e = 5\,\text{eV}$  (Fig. 2.3), the model not only reproduces the shape and position of the peaks, but also its magnitude. Overall, the excellent agreement confirms the BBK approach as a reliable tool for describing electronimpact ionization in such small atomic systems.

#### 2.2.2.2 Application to Neon

We now compare the BBK results with the experimental data from Ref. [5], performed at intermediate impact energy (approximately 600 eV) in an asymmetric coplanar geometry. TDCS calculations are presented in Fig. 2.4 for the ionization of Ne  $2p^6$  as a function of the ejection angle at a scattering energy of 500 eV, with a fixed scattering angle of  $\theta_s = 6^{\circ}$ , in coincidence with the ejected electron energies  $E_e = 37$ , 74, and 205 eV, corresponding to momentum transfers of K = 0.74, 0.87, and 1.44 a.u., respectively (panels (a), (b), and (c)).

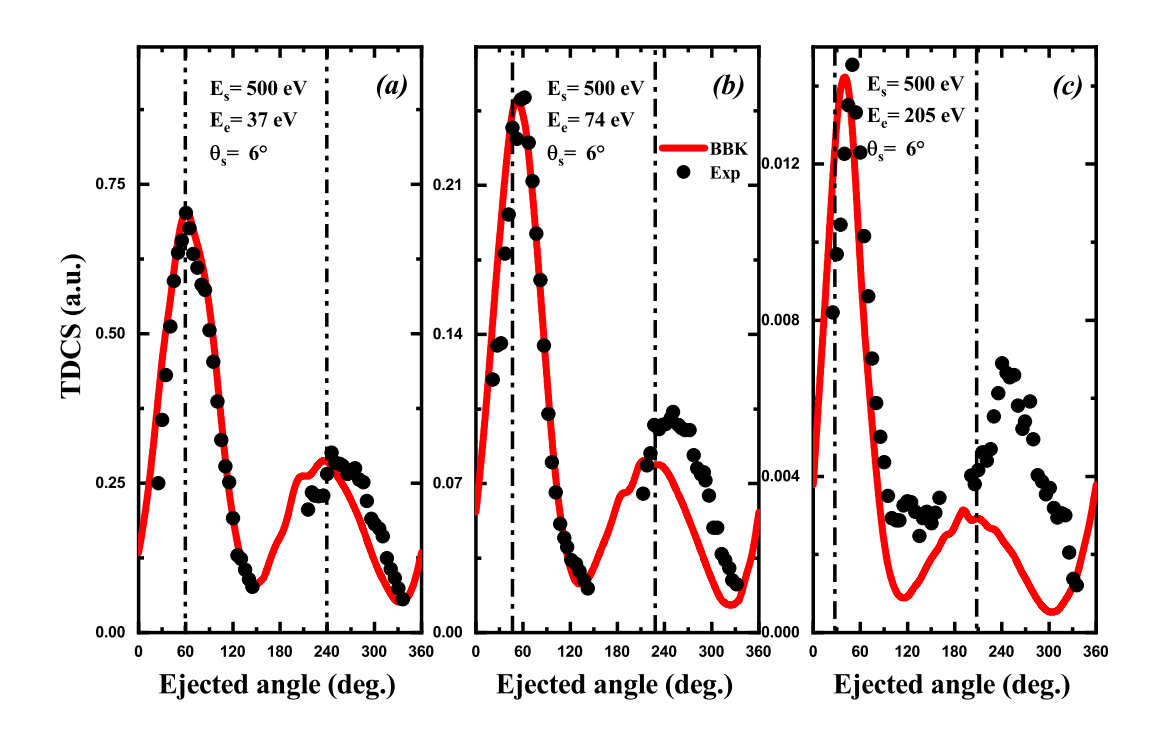


Figure 2.4: TDCS for the ionization of Ne  $2p^6$  as a function of the ejection angle at 500 eV scattering energy, The projectile is scattered at an angle  $\theta_s = 6^{\circ}$  in coincidence with the ejected electron with  $E_e = 37$ , 74 and 205 eV in panels (a), (b), and (c) respectively. Theoretical result is the red solid line (BBK), and the normalized experimental data from [5] are black circles.

The theoretical TDCS exhibit a double peak structure across the three impact energies, in the direction of transfer momentum  $\mathbf{K}$  and  $-\mathbf{K}$ , at  $E_e = 37eV$  (panel a), the BBK model provides a good overall agreement, reproducing both the binary and recoil peaks. As the ejected electron energy increases to  $E_e = 74eV$  (panel b), the model still follows the binary peak well but starts deviating in the recoil region. At  $E_e = 205eV$  (panel c), while the binary peak remains well-described, the recoil peak is underestimated.

#### 2.2.2.3 Application to Argon

To further test the BBK model, the TDCS for two different kinematic conditions for Argon  $3p^6$  are compared with the experimental data [7,8]. The first case corresponds to an incidence energy of 1 keV, an ejection energy of 13 eV, and a scattering angle of  $\theta_s = 1.2^{\circ}$ : as shown in Figure 2.5 (a), the agreement between theory and experimental data is moderately good in the binary and recoil regions, with no significant discrepancies observed. The second case involves a scattering energy of 500 eV, an ejection energy of 205 eV, and a scattering angle of  $\theta_s = 3^{\circ}$ : Figure 2.5 (b) shows that the outcomes differ dramatically, the BBK model failing to reproduce all the experimental data in the recoil

region.

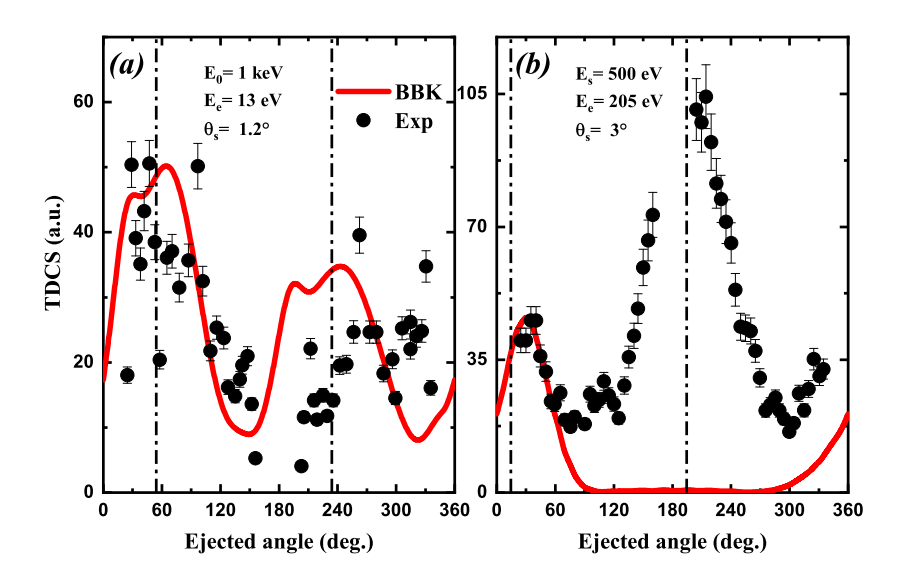


Figure 2.5: TDCS for the ionization of Ar  $3p^6$  as a function of the ejection angle: (a) at 1 keV impact energy, with a scattered angle  $\theta_s = 1.2^{\circ}$  in coincidence with the ejected electron of energy  $E_e = 13$  eV. The right panel (b) a scattering energy of 500 eV, a scattering angle  $\theta_s = 3^{\circ}$ , and an ejected electron energy of  $E_e = 13$  eV. Theoretical results are shown as red solid line (BBK), while the normalized experimental data from [7,8] are represented by black circles.

The kinematics in Figure 2.5 (a) involve a much smaller momentum transfer  $K \approx 0.22$  atomic units, reducing the influence of the residual ion. As a result, the BBK model performs reasonably well in describing the process for this case. In Figure 2.5 (b), the kinematics correspond to a large momentum transfer  $K \approx 1.27$  atomic units, resulting in a significant recoil momentum q (up to 5.2 atomic units) absorbed by the target. This leads to strong interactions between the outgoing electrons and the residual ion [9], making the recoil region particularly challenging to model theoretically. In this regime, the BBK model fails to accurately describe the kinematics.

The limitations of the BBK model, particularly in describing processes involving large momentum transfers and strong residual ion interactions, highlighted the need for more advanced theoretical frameworks. This led to the development of sophisticated models that incorporate distortion effects, such as BBK1CWZ and BBK2CWZ.

# 2.3 The concept of variable charge

As discussed in the previous section, the BBK model is not sufficient to explain (e,2e) experiments. Therefore, it is essential to account for additional interactions, such as dis-

tortion effects which play a crucial role especially at lower impact energies. Differently from conventional distorted wave approaches, in our work, distortion effects are represented by a Coulomb wave with a variable charge, and are therefore introduced in an approximate manner. Specifically, the continuum electrons are described using a Coulomb wave with a variable charge denoted Z(r), rather than a constant nuclear charge Z. This radial-dependent effective charge is determined from the Hartree potential, which consists of two components: a Coulomb potential representing the long-range interaction between the target and the electron (at large distances from the nucleus, this potential retains its Coulombic character), and a short-range potential that accounts for polarization effects and additional electronic interactions within the target atom or molecule. We consider the angularly averaged potential

$$U_i(r) = \frac{1}{4\pi} \int V(\mathbf{r}) d\Omega \tag{2.10}$$

of the Hartree potential

$$V(\mathbf{r}) = \frac{Z}{r} - \sum_{i} N_{i} \left\langle \varphi_{i} \left| \frac{1}{|\mathbf{r} - \mathbf{r}_{i}|} \right| \varphi_{i} \right\rangle$$
 (2.11)

where Z is the charge at the center of the target,  $N_i$  is the number of electrons in orbital i, and  $\varphi_i(\mathbf{r})$  is the wave function of orbital i. The explicit form of the short-range potential,  $U(\mathbf{r})$ , is detailed in [4], written as:

$$U(r) = \frac{1}{r} + \sum_{i} N_{i} \sum_{k,k'} a_{ik} a_{ik'} N_{n_{ik'}} N_{n_{ik}} \delta_{l_{ik},l_{ik'}} \delta_{m_{ik},m_{ik'}} \frac{n_{kk'}!}{r \xi_{kk'}^{n_{kk'}+1}} e^{-\xi_{kk'} r} \sum_{s=0}^{n_{kk'}-1} \frac{(n_{kk'}-s)}{s!} (\xi_{kk'} r)^{s}$$

$$(2.12)$$

We can express this potential as

$$U(r) = \frac{Z(r)}{r} \tag{2.13}$$

where

$$Z(r) = 1 + \sum_{i} N_{i} \sum_{k,k'} a_{ik} a_{ik'} N_{n_{ik'}} N_{n_{ik}} \delta_{l_{ik},l_{ik'}} \delta_{m_{ik},m_{ik'}} \frac{n_{kk'}!}{r \xi_{kk'}^{n_{kk'}+1}} e^{-\xi_{kk'} r} \sum_{s=0}^{n_{kk'}-1} \frac{(n_{kk'}-s)}{s!} (\xi_{kk'} r)^{s}$$

$$(2.14)$$

It is easy to verify that the charge function Z(r) satisfies:

$$Z(0) = 1 + \sum_{i} N_i = Z, \text{ and } Z(r \to \infty) = 1$$
 (2.15)

## 2.3.1 Variable charge as a distortion approximation

To justify the use of the Coulomb wave model with a variable charge, we conduct a comparative study between a distorted wave and a spherical Coulomb wave with a variable charge. Specifically, we compare the radial part of the distorted wave function in equation 1.26, computed numerically, with the radial part of the Coulomb wave in equation 1.21, which is known analytically and given by [9]:

$$u_{cw}(r) = C_{\ell}(\alpha) \exp(ikr) (kr)^{\ell+1} {}_{1}F_{1}(\ell+1+i\alpha, 2\ell+2, -2ikr), \tag{2.16}$$

with

$$C_{\ell}(\alpha) = 2^{\ell} \exp\left(\frac{-\pi\alpha}{2}\right) \frac{|\Gamma(\ell+1+i\alpha)|}{(2\ell+1)!} \quad ; \quad \alpha = -\frac{Z(r)}{k}. \tag{2.17}$$

Figure 2.6 presents the partial radial wave functions for the ionization of argon Ar  $3p^6$  as a function of the distance r, for angular momentum quantum numbers ranging from  $\ell = 0$  to  $\ell = 5$ , and energy E = 74 eV.

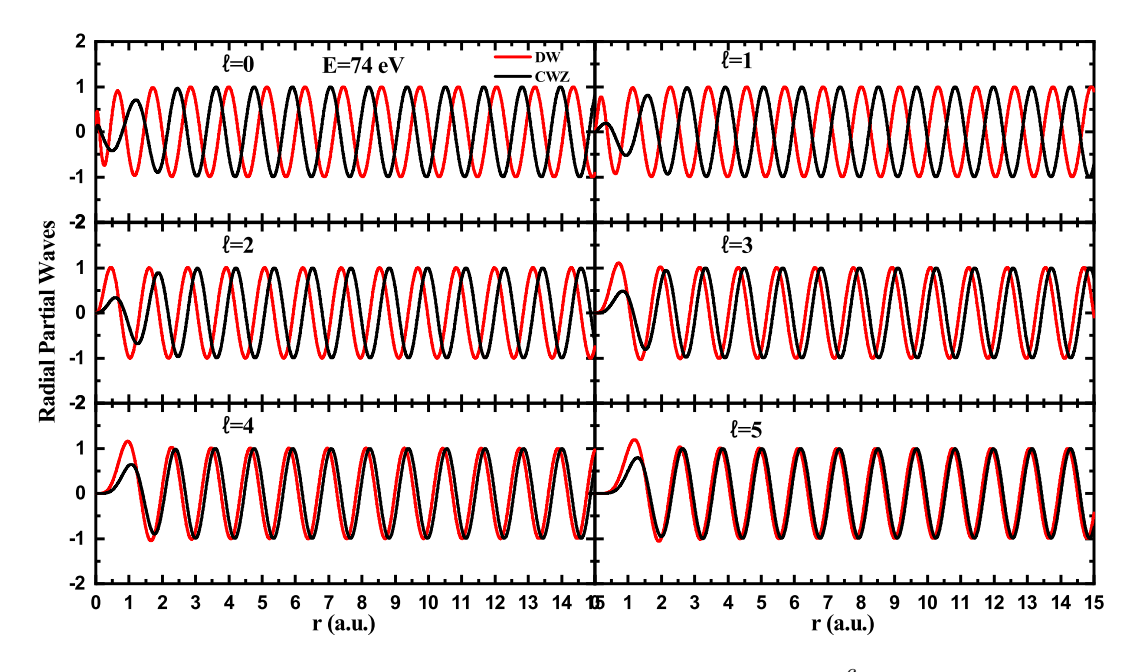


**Figure 2.6:** Partial radial wave functions for the ionization of Ar  $3p^6$  as a function of distance r, plotted for  $\ell=0$  to  $\ell=5$ . The results compare a distorted wave (DW, solid black line) with a spherical Coulomb wave of variable charge (CWZ, solid red line) at an ejection energy of E=74 eV.

Clearly, for higher  $\ell$  values, the Coulomb wave matches the distorted wave except at some short distances; where distortion effects are more significant. For the lower  $\ell$  values deviations appear on the whole radial domain, and a clear phase shift is observed. However, the overall agreement supports the idea that the variable charge model captures essential

distortion effects to some degrees. Thus, this approach can lead to reasonable accuracy, while offering significant advantages in terms of computational efficiency.

### 2.4 Previous theoretical models

The first model, known as BBKDW (or BBK1CWZ), is essentially a BBK model that incorporates a variable-charge Coulomb wave to describe the ejected electron. This model was introduced in 2016 by Chinoune et al. [10] and was tested under several kinematic conditions for the ionization of various atomic targets and the methane molecule. While some improvements have been observed with respect to the original BBK model, particularly in amplitude, the differences were often not substantial. Consequently, this motivated a further refinement where the model was extended as to describe also the scattered electron using a variable-charge Coulomb wave. This led to the development of the BBK2DW (or BBK2CWZ) model in 2023 by Attia et al. [11].

#### 2.4.1 BBK2CWZ model

Building upon the previous BBKDW model, the model was extended. In the BBK2DW framework, both the ejected and scattered electrons are represented by an approximate distorted wave specifically, a Coulomb wave with a variable charge Z(r). The resulting scattering amplitude is then expressed as follows:

$$T_{if} = -\frac{1}{2\pi} \left\langle \phi_{CW}^{Z}(\mathbf{k_s}, \mathbf{r_0}) \phi_{CW}^{Z}(\mathbf{k_e}, \mathbf{r_1}) C(\alpha_{01}, \mathbf{k_{01}}, \mathbf{r_{01}} \mid V(r_0, r_1) \mid (2\pi)^{-3/2} e^{i\mathbf{k_i} \cdot \mathbf{r_0}} \phi_i(\mathbf{r_1}) \right\rangle,$$
(2.18)

where

- $\phi^Z_{CW}$  represents the Coulomb wave functions for the scattered and ejected electrons,
- $V(r_0, r_1)$  is the interaction potential.
- $\phi_i$  is the initial state wave function of the target electron.

The variable charge Z(r) for the two outgoing electrons behave as follows. The ejected electron experiences a charge  $Z_e = N$  at the center of the target, and asymptotically reduces to  $Z_e = 1$ . At the center of the target, the scattered electron perceives a charge  $Z_s = N$ , while asymptotically, two possible scenarios can be considered:

• The scattered electron experiences an asymptotic charge of  $Z_s = 1$ , similar to the ejected electron. In this case, the model is referred to as BBK2CWZ1.

• Alternatively, if the scattered electron is faster than the ejected electron, it may feel the screening of the ejected electron, resulting in an asymptotic charge  $Z_s = 0$ . In this case, the model is referred to as BBK2CWZ0.

These models have been applied in several situations for atomic targets [11]. For the sake of comparison, we now consider the same scenario as depicted in Figure 2.5 (panel b), where the kinematics correspond to a large momentum transfer.

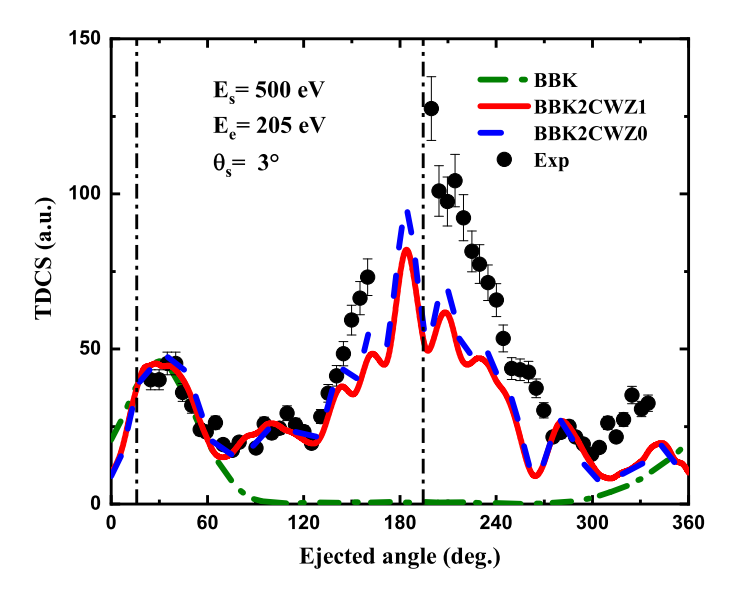


Figure 2.7: TDCS for the ionization of Ar  $3p^6$  as a function of the ejection angle, at a scattering energy of 500 eV, a scattering angle of  $\theta = 3^{\circ}$ , and an ejected electron energy of  $E_e = 13$  eV. Theoretical results are shown as the red solid line (BBK2CWZ1), dashed blue line (BBK2CWZ0), and dash-dot green line (BBK), while the normalized experimental data from [8] are represented by black circles.

As previously noted in Figure 2.5 the BBK model fails to reproduce the recoil peak. In Figure 2.7, we compare the refined BBK2CWZ1 and BBK2CWZ0 models to the experimental data and the original BBK result. Clearly, the BBK2CWZ approaches show a very good agreement with the experimental data, particularly in the recoil region, highlighting the advantage of including an approximate distorted wave treatment for both outgoing electrons. However, treating the incident electron as a plane wave limits the applicability of this model to intermediate and higher impact energies only. We further refined this model (Bechane et al. [1]) by representing the incident electron as well by a Coulomb wave with a variable charge. This extension enables the variable-charge approach to be applied in low-energy kinematics, where distortion effects become particularly significant.

# 2.5 Three coulomb waves with a variable charge model 3CWZ

Building on the limitations observed in previous models, and the necessity to test the variable charge approach at low energy kinematics, the 3CWZ model was developed to provide a more comprehensive three-body description of electron-impact ionization. In this model, the incident, ejected, and scattered electrons are all represented by Coulomb waves with a variable charge, thereby enabling a more accurate treatment of exchange and distortion effects, especially at low impact energies. Under strong kinematical asymmetry, the fast scattered electron and the slower ejected electron are easily distinguished, so exchange effects can be neglected. At low impact energies, in contrast this distinction diminishes and exchange interactions must be taken into account. Therefore, the TDCS for this model is written as follows:

$$\sigma^{(3)} = \frac{d^3 \sigma}{d\Omega_e d\Omega_s dE_e} = (2\pi)^4 \frac{k_e k_s}{k_i} (|T_{dir}|^2 + |T_{exc}|^2 + |T_{dir} - T_{exc}|^2)$$
 (2.19)

The direct term  $T_{dir}$  and the exchange  $T_{exc}$  term are respectively given by

$$T_{dir} = \langle \phi_{CW}^{z(-)}(\mathbf{k}_s, \mathbf{r}_0) \phi_{CW}^{z(-)}(\mathbf{k}_e, \mathbf{r}_1) | C(\alpha_{01}, \mathbf{k}_{se}, \mathbf{r}_{01}) | \frac{1}{r_{01}} - \frac{1}{r_0} | \phi_{CW}^{z(+)}(\mathbf{k}_i, \mathbf{r}_0) \Phi_{nlm}(\mathbf{r}_1) \rangle \quad (2.20)$$

$$T_{exc} = \langle \phi_{CW}^{z(-)}(\mathbf{k}_s, \mathbf{r}_1) \phi_{CW}^{z(-)}(\mathbf{k}_e, \mathbf{r}_0) | C(\alpha_{01}, \mathbf{k_{es}}, \mathbf{r_{10}}) | \frac{1}{r_{01}} - \frac{1}{r_0} | \phi_{CW}^{z(+)}(\mathbf{k}_i, \mathbf{r}_0) \Phi_{nlm}(\mathbf{r}_1) \rangle \quad (2.21)$$

with

$$T_{dir} = T_{dir}^1 - T_{dir}^0 (2.22)$$

and

$$\begin{cases}
T_{dir}^{1} = \int \phi_{CW}^{z(-)*}(\mathbf{k}_{e}, \mathbf{r}_{1}) \phi_{CW}^{z(-)*}(\mathbf{k}_{s}, \mathbf{r}_{0}) C(\alpha_{01}, \mathbf{k}_{se}, \mathbf{r}_{01}) \times \frac{1}{r_{01}} \times \phi_{CW}^{z(+)}(\mathbf{k}_{i}, \mathbf{r}_{0}) \Phi_{nlm}(\mathbf{r}_{1}) d\mathbf{r}_{0} d\mathbf{r}_{1} \\
T_{dir}^{0} = \int \phi_{CW}^{z(-)*}(\mathbf{k}_{e}, \mathbf{r}_{1}) \phi_{CW}^{z(-)*}(\mathbf{k}_{s}, \mathbf{r}_{0}) C(\alpha_{01}, \mathbf{k}_{se}, \mathbf{r}_{01}) \times \frac{1}{r_{0}} \times \phi_{CW}^{z(+)}(\mathbf{k}_{i}, \mathbf{r}_{0}) \Phi_{nlm}(\mathbf{r}_{1}) d\mathbf{r}_{0} d\mathbf{r}_{1}
\end{cases}$$
(2.23)

where  $\Phi_{nlm}$  is the initial bound state wave function of the target, while  $\phi_{CWZ}^{z(+)}$  and  $\phi_{CWZ}^{z(-)}$  respectively represent the outgoing and incoming Coulomb waves [12], which are written as

$$\begin{cases}
\phi_{CW}^{z(+)}(\mathbf{k}, \mathbf{r}) = \frac{e^{i\mathbf{k}\cdot\mathbf{r}}}{(2\pi)^{3/2}} \Gamma(1 - i\alpha(r))_1 F_1(i\alpha(r), 1, i(kr - \mathbf{k}\cdot\mathbf{r})) e^{-\frac{\pi\alpha(r)}{2}} \\
\phi_{CW}^{z(-)}(\mathbf{k}, \mathbf{r}) = \frac{e^{i\mathbf{k}\cdot\mathbf{r}}}{(2\pi)^{3/2}} \Gamma(1 + i\alpha(r))_1 F_1(-i\alpha(r), 1, -i(kr + \mathbf{k}\cdot\mathbf{r})) e^{-\frac{\pi\alpha(r)}{2}}
\end{cases}$$
(2.24)

with  $\alpha(r) = \frac{Z(r)}{k}$ . The amplitudes 2.23 involve a six-dimensional integral. Numerically it requires significant computational time. We have used a technique, proposed by Kornberg and Miraglia [13], that employs Fourier transforms to substantially simplify the calculations [4].

# 2.6 Molecular three coulomb waves with a variable charge model M3CWZ

Currently, the most powerful approach for describing the electron-impact ionization of molecular targets is the M3DW model. While the model provides a generally good description of differential ionization cross sections for various molecules, it remains computationally expensive.

In this thesis, we extended the 3CWZ model to molecular targets while preserving its numerical advantages. The resulting model is named M3CWZ.

The ionization of the target can also occur via a capture process [14], in which the incident electron is captured into a bound state while two initially bound electrons are ejected. This process is generally not considered in (e, 2e) theoretical studies at intermediate to high impact energies. Neglecting capture effects, the fourfold differential cross-section (4DCS) for a specific molecular orientation is given by [15]:

$$\sigma^{(4)} = \frac{d^4 \sigma}{d\Omega_{Euler} d\Omega_s d\Omega_e dE_e} = (2\pi)^4 \frac{k_e k_s}{k_i} (|T_{dir}|^2 + |T_{exc}|^2 + |T_{dir} - T_{exc}|^2)$$
(2.25)

with  $d\Omega_{Euler} = \sin \beta \, d\beta \, d\alpha \, d\gamma$ , where  $(\alpha, \beta, \gamma)$  are the Euler angles.

In our approach, we adopt the frozen core and single active electron approximations for the initial molecular bound wave function  $\Phi_i(\mathbf{r}_1)$ ; the direct and exchange terms are given by equations 4.7 and 4.8, respectively. For the initial molecular bound wave function of the target, we use Moccia's single center molecular orbitals expanded in a set of Slater-type orbitals [16].

To compare with experimental data obtained from randomly oriented molecules, the 4DCS must be averaged over all Euler angles.

$$\sigma_{\text{molecule}}^{(3)} = \frac{1}{8\pi^2} \int \sigma^{(4)} d\Omega_{\text{Euler}}.$$
 (2.26)

In our theoretical framework, this integration is carried out analytically [17] using the following property for the rotation matrix

$$\frac{1}{8\pi^2} \int d\Omega_{Euler} D_{\mu,m}^l(\alpha,\beta,\gamma) D_{\mu',m'}^{l'*}(\alpha,\beta,\gamma) = \frac{1}{\hat{l}} \delta_{l,l'} \delta_{m,m'} \delta_{\mu,\mu'}$$
(2.27)

where  $\hat{l} = 2l + 1$ .

The variable charge is obtained from

$$U_i(r_1) = \frac{1}{4\pi} \int V_i(\mathbf{r_1}, \mathbf{R}_i) d\Omega = -\frac{Z(r_1)}{r_1},$$
 (2.28)

where  $V_i(\mathbf{r}, \mathbf{R}_i)$  is taken here to be the standard Hartree potential defined for molecules by

$$V_i(\mathbf{r}_1, \mathbf{R}_i) = -\sum_{N=1}^{M} \frac{Z_N}{|\mathbf{r}_1 - \mathbf{R}_N|} + \sum_{j=1}^{N_0} N_{ij} \int \frac{|\varphi_j(\mathbf{r})|^2}{|\mathbf{r} - \mathbf{r}_1|} d\mathbf{r}$$
(2.29)

where  $N_0$  is the number of occupied orbitals,  $N_{ij}$  is the number of electrons in the orbital, M and  $Z_N$  are the number of nuclei and their charges respectively, and  $R_N$  being their positions with respect to the molecular center of mass.

### 2.7 Conclusion

This chapter provided an overview of the theoretical background of the variable charge approach. The chapter begins by revisiting foundational models such as the One-Coulomb Wave (1CW) and the BBK model, which were instrumental in understanding (e,2e) reactions. These models, while effective in certain scenarios, particularly at high energies, revealed limitations when dealing with low-energy collisions and complex atomic targets, especially in describing the recoil region. To address these limitations, the concept of a variable charge was introduced, which approximates distortion effects. This led to the development of more sophisticated models such as BBK1CWZ and BBK2CWZ. The BBK2CWZ model showed significant improvements in reproducing experimental data, particularly in the recoil region, highlighting the importance of distortion effects in ionization processes, but treating the incident electron as a plane wave limited the applicability of this model to intermediate and higher impact energies only, which required a further refinement. We then extended the variable-charge concept also to the incident electron, creating the Three Coulomb Waves with a Variable Charge (3CWZ) model, which is particularly relevant at low impact energies, where exchange and distortion effects are crucial. Finally, we generalized this approach to molecular targets, resulting in

the Molecular Three Coulomb Waves with a Variable Charge (M3CWZ) model.

# **Bibliography**

- [1] K. Bechane, S. Houamer, T. Khatir, A. Tamin, and C. Dal Cappello. *Phys. Rev. A*, **109**:012812, 2024.
- [2] O. Zaidi, A. Mansouri, S. Houamer, A. Tamin, T. Khatir, and C. Dal Cappello. Eur. Phys. J. D, 78:140, 2024.
- [3] A. Tamin, S. Houamer, T. Khatir, L. U. Ancarani, and C. Dal Cappello. J. Chem. Phys., 161:164305, 2024.
- [4] M. Chinoune. PhD thesis, University Of Science And Technology Houari Boumediene, 2017.
- [5] A. S. Kheifets, A. Naja, E. M. Staicu Casagrande, and A. Lahmam-Bennani. *J. Phys. B: At. Mol. Opt. Phys.*, **41**:145201, 2008).
- [6] M. Brauner, J. S. Briggs, and H. Klar. J. Phys. B: At. Mol. Opt. Phys., 22(14):2265–2287, 1989.
- [7] D. S. Milne-Brownlie, S. Cavanagh, B. Lohmann, C. Champion, P. A. Hervieux, and J. Hanssen. *Phys. Rev. A*, **69**:032701, 2004.
- [8] R. El Mir, E. M. Staicu Casagrande, A. Naja, C. Dal Cappello, S. Houamer, and F. El Omar. J. Phys. B: At. Mol. Opt. Phys., 48:175202, 2015.
- [9] M. Attia. PhD thesis, University Ferhat Abbas Sétif 1, 2024.
- [10] M. Chinoune, S. Houamer, and C. Dal Cappello A. Galstyan. J. Phy. B, 49(205201), 2016.
- [11] M. Attia, S. Houamer, T. Khatir, K. Bechane, S. Houamer, and C. Dal Cappello. J. Phys. B: At. Mol. Opt. Phys., **56**:075201, 2023.
- [12] L. D. Landau and E. M. Lifshitz. Quantum Mechanics: Non-Relativistic Theory. Pergamon Press, Oxford., 1981.
- [13] M. A. Kornberg and J. E. Miraglia. Phys. Rev. A, 48:3714, 1993.
- [14] M. R. H. Rudge. Rev. Mod. Phys., 40:564, 1968.
- [15] D. H. Madison and O. Al-Hagan. J. Atomic and Molecular Phys., 2010:367180, 2010.
- [16] R. Moccia. J. Chem. Phys., **40**:2164, 1964.

[17] C. Champion, C. Dal Cappello , S. Houamer, and A. Mansouri. *Phys. Rev. A*,  $\bf 73:012717,\ 2006.$ 

# Chapter 3

# Application on Atoms: Argon and Neon

# 3.1 Introduction

In this chapter <sup>1</sup>, we apply the Three Coulomb Waves with a Variable Charge (3CWZ) model to atomic targets specifically neon and argon. The 3CWZ model incorporates variable charge effects to represent the incident, scattered, and ejected electrons, aiming to improve predictions of triply differential cross sections (TDCS) across a range of kinematic conditions. Neon has an electronic structure simpler than argon, and serves as an initial test to validate the model's performance at high, intermediate, and low impact energies. Notably, neon has been extensively studied in the context of electron impact ionization, with comprehensive experimental and theoretical investigations reported in the literature [2–5]. We then extend our analysis to argon in intermediate and low energy regimes, leveraging extensive experimental data for comparison [6, 7]. Like neon, argon has been widely investigated in the context of electron impact ionization (see, e.g., [2, 6–8]), providing a robust benchmark for our theoretical predictions. Our results are compared with experimental results and other theoretical approaches, such as the DWBA, DWB2-RM, and 3DW, to evaluate its efficacy.

# 3.2 Neon

The 3CWZ model was initially tested on neon, for which extensive experimental data is available [2,3]. Although the tests were performed under a limited range of kinematic conditions, they serve as an important bridge for extending the model to more complex atomic targets.

<sup>&</sup>lt;sup>1</sup>Parts of this chapter are reproduced from our publication [1]

## 3.2.1 Target wave function and variable charge

#### 3.2.1.1 Target wave function

Let us consider the neon atom (Z = 10), whose electronic configuration is  $1s^2 2s^2 2p^6$ . The active electron in neon is described using Clementi's Hartree–Fock wave functions with a Slater-type basis (see Equation 1.63). The parameters associated with these wave functions, denoted as  $n_{ik}$ ,  $l_{ik}$ ,  $m_{ik}$ ,  $\xi_{ik}$ ,  $\beta_{ik}$ , along with the corresponding ionization energies, are summarized in Table 3.1.

n	l	m	ξ	(1s)	(2s)	(2p)
1	0	0	9.5735	0.93093	-0.23171	
1	0	0	15.4496	0.04610	-0.00442	
2	0	0	1.9550	-0.00085	0.18201	
2	0	0	2.8462	0.00321	0.66106	
2	0	0	4.7746	-0.00180	0.32372	
2	0	0	7.7131	0.03537	-0.14244	
2	1	m	1.4700			0.22430
2	1	m	2.3717			0.51826
2	1	m	4.4545			0.33902
2	1	m	9.4550			0.01765
Ior	Ionization energies (a.u.)			32.77248	1.93043	0.85044

**Table 3.1:** Parameters of Clementi's wave functions and ionization energies of the atomic orbitals of the neon atom.

#### 3.2.1.2 Variable charge

The static potential in Equation 2.13 for the ionization of Ne 2p is calculated and written as:

$$U(r_1) = \frac{1}{4\pi} \int \left[ -\frac{10}{r_1} + 2 \int \frac{|\phi_{1s}|^2}{|\mathbf{r} - \mathbf{r}_1|} d\mathbf{r} + 2 \int \frac{|\phi_{2s}|^2}{|\mathbf{r} - \mathbf{r}_1|} d\mathbf{r} + 5 \int \frac{|\phi_{2p}|^2}{|\mathbf{r} - \mathbf{r}_1|} d\mathbf{r} \right] d\Omega_e$$

$$= -\frac{Z(r_1)}{r_1}.$$
(3.1)

and the variable charge Z(r) can be expressed as

$$\begin{cases}
Z_{e/s}(r) = 10 - 2Z_{1s}(r) - 2Z_{2s}(r) - 5Z_{2p}(r) \\
Z_{i}(r) = 10 - 2Z_{1s}(r) - 2Z_{2s}(r) - 6Z_{2p}(r)
\end{cases}$$
(3.2)

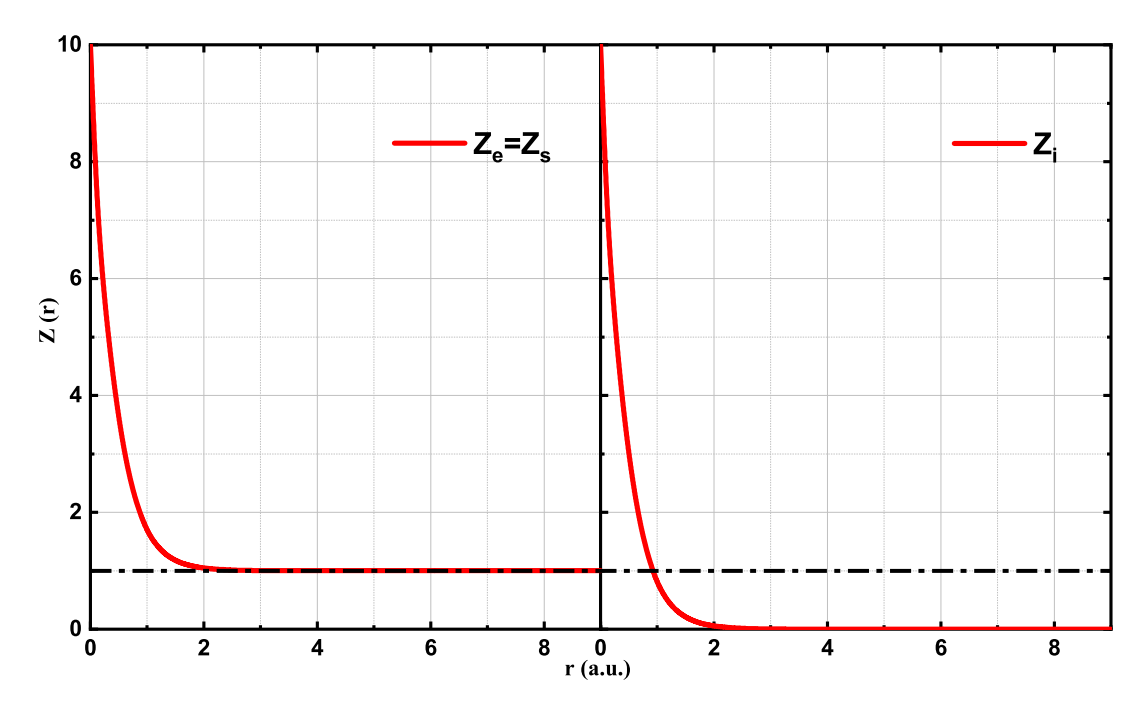


Figure 3.1: Variable charge experienced by the incident electron, the scattered electron, and the ejected electron during the ionization process of Ne 2p.

In the two panels of Fig. 3.1, we show the variable charge Z(r) for the continuum electrons.  $Z_s(r)$  and  $Z_e(r)$  decrease from Z = 10 to Z = 1, while  $Z_i(r)$  decreases from Z = 10 to Z = 0. The asymptotic values of Z(r) are reached at about r = 3 a.u.

#### 3.2.2 Results and Discussion

Figure 3.2 presents absolute TDCS data for the ionization of the neon 2s orbital at an incident energy of  $E_0 = 150$  eV, at a fixed scattering angle  $\theta_s = 10^{\circ}$  for panel (a), and  $\theta_s = 15^{\circ}$  for panel (b), and an ejection energy  $E_e = 10$  eV.

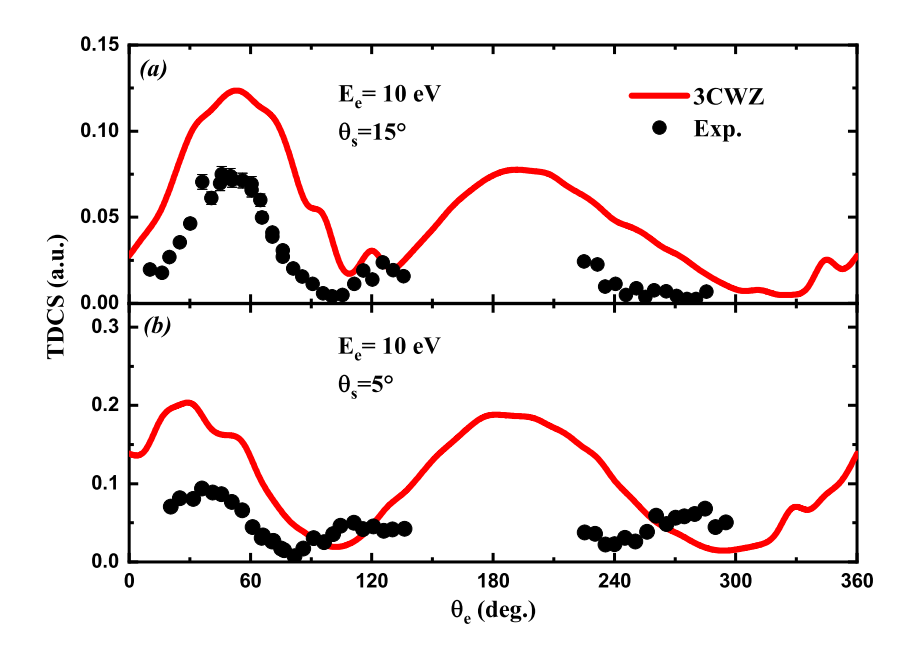


Figure 3.2: Absolute TDCS for the ionization of neon 2s at an incident energy of 150eV, as a function of the ejection angle at scattering angles  $\theta_s = 15^{\circ}$  for panel (a), and  $\theta_s = 5^{\circ}$  for panel (b), and ejected electron energy fixed at  $E_e = 10$  eV. Theoretical results are represented by a red solid line (3CWZ), the absolute experimental data are shown as black circles from [2].

Figure 3.2 shows that the 3CWZ model somewhat reproduces the shape and position of the binary peak. However, since these data are provided on an absolute scale, the TDCS can be compared not only in shape but also in magnitude. It is clear that the 3CWZ model strongly overestimates the data in the binary region in both panel (a) and panel (b). In the recoil region, the model predicts a very large recoil peak; however, the lack of experimental data in the range of  $\theta_e = 140^{\circ}$  to  $\theta_e = 240^{\circ}$  prevents a definitive conclusion on the extent of this overestimation. This discrepancy should be attributed to the frozen-core approximation used in this study, which is not justified for inner orbitals. (see Chapter 1, Section 1.7).

Figure 3.3 presents absolute TDCS data for the ionization of the neon 2p orbital under two distinct kinematic conditions: in panel (a), the incident energy is  $E_i \approx 599.6$  eV with a fixed scattering angle of  $\theta_s = 6^{\circ}$  and an ejection energy  $E_e = 74$  eV; in panel (b),  $E_i = 150$  eV with  $\theta_s = 5^{\circ}$  and  $E_e = 10$  eV.

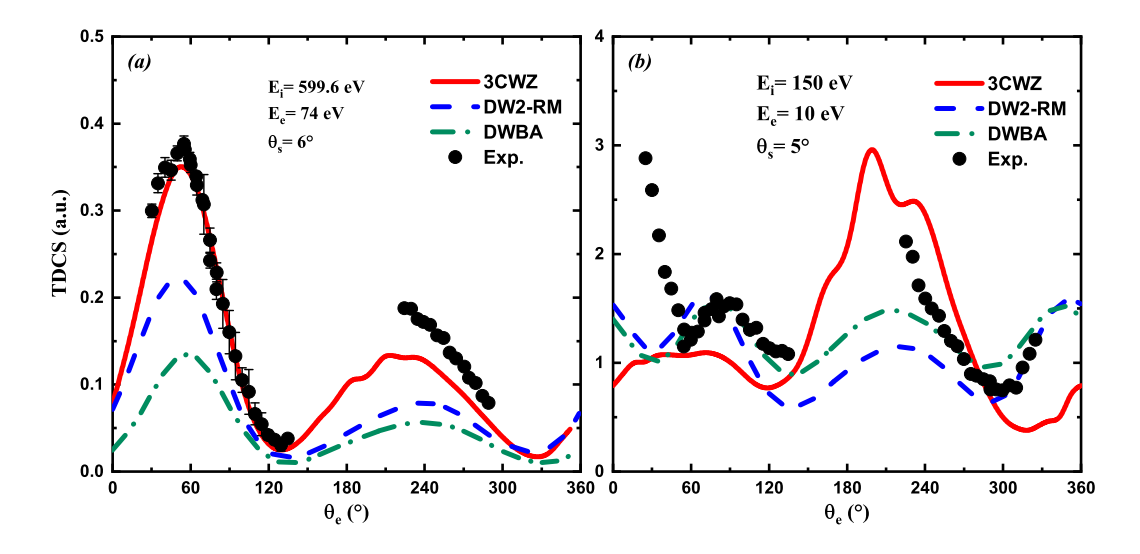


Figure 3.3: Absolute TDCS for the ionization of neon 2p as a function of the ejection angle at a fixed scattering angle  $\theta_s = 6^{\circ}$  for panel (a), and  $\theta_s = 5^{\circ}$  for panel (b). The incident and ejected electrons have respective energies: (a)  $E_i = 599.6eV$  and  $E_e = 74eV$ , (b)  $E_i = 150eV$  and  $E_e = 10eV$ . Theoretical results are represented by a red solid line (3CWZ), a blue dashed line (DW2-RM) [2], a green dash-dot line (DWBA) [2]. The absolute experimental data are shown as black circles from [2].

In panel (a), corresponding to an intermediate ejection energy regime, the 3CWZ model reproduces quite well the overall shape of the TDCS in the binary and recoil peak seen in the experimental data, the amplitude of the TDCS is reproduced perfectly in the binary region, while in the recoil region the data are somewhat underestimated. In contrast, although the DWB2-RM and DWBA models capture the overall shape, they underestimate substantially the binary and recoil regions, resulting in poor overall agreement. In panel (b), which represents a lower ejection energy, the 3CWZ model continues to capture the overall shape of the TDCS; however, discrepancies in peak magnitudes become more evident, especially in the binary region. While the DWBA and DWB2-RM models yield a reasonable fit in terms of shape, the magnitude predictions are underestimated by both models. These results underscore the advantage of the 3CWZ model, which enables a more precise treatment of post-collision interactions and better reproduces the subtle features of both the binary and recoil regions.

A second test of the model was conducted under a lower impact energies, which can be a challenge to most theoretical models. With the emergence of new techniques that offers high quality measurements, such as the COLTRIMS reaction microscope (C-REMI) (see chapter 1 section 1.3.1), the 3D TDCS was presented as cuts along the three orthogonal planes (xz, xy, and yz) [3]; however, here we have selected only a few of the available kinematic settings from the scattering plane (xz). Figure 3.4 illustrates TDCS calculations at a low impact energy of 65 eV [3]. Panels (a), (b), and (c) display the TDCS for the

ionization of the neon 2p orbital at a fixed scattering angle of  $20^{\circ}$ , with ejected-electron energies of 2 eV, 4.5 eV, and 8.5 eV, respectively.

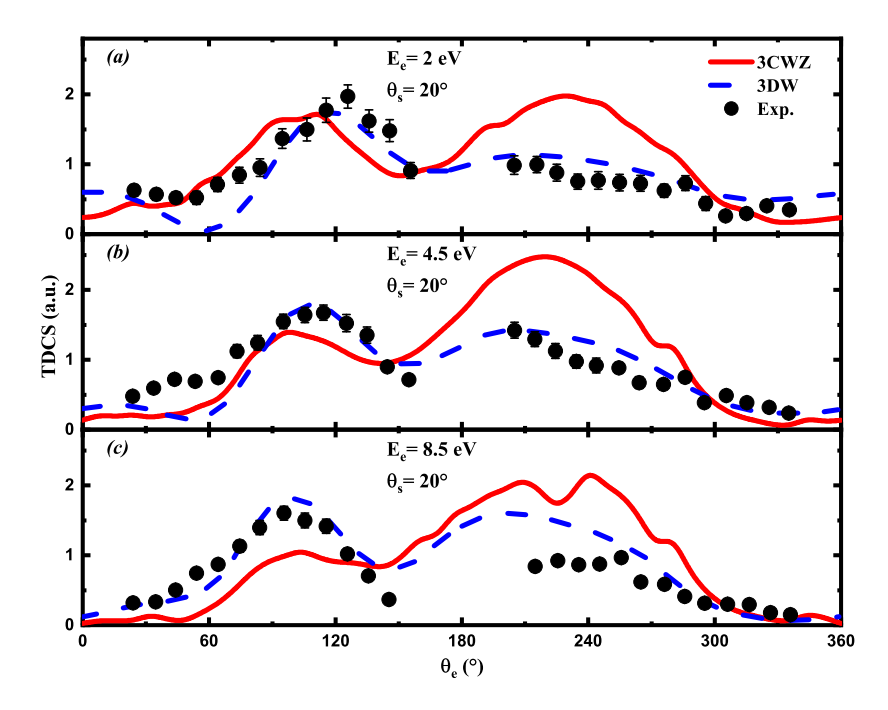


Figure 3.4: TDCS for the ionization of neon 2p as a function of the ejection angle at a fixed scattering angle  $\theta_s = 20^{\circ}$ , and incident energy 65 eV, and ejection energies (a)  $E_e = 2$  eV, (b) 4.5 eV, (c) 8 eV. Theoretical results are represented by a red solid line (3CWZ), a blue dashed line (3DW) [3]. The relative experimental data are shown as black circles from [3].

Panel (a),  $E_e = 2$  eV: Both 3CWZ and 3DW models, which treat exactly the (PCI), capture the main shape in the binary and recoil regions. Minor discrepancies in peak positioning suggest differences in how each model accounts for post collisional interactions, or the limitations of the variable charge approximation at low impact energies. Panel (b),  $E_e = 4.5$  eV: the overall shape is again reproduced by both models, although 3DW appears to track the binary region slightly better, and is more consistent in the recoil region. Panel (c),  $E_e = 8.5$  eV: the binary peak is well represented by 3CWZ, whereas 3DW shows a better agreement with experimental data, while both models overestimate the recoil peak. Overall, each model reproduces the principal structures of the TDCS, though subtle distinctions in binary and recoil peak positions remain. This underlines the complexity of modeling electron-impact ionization at low impact energies.

# 3.3 Argon

In this section, the 3CWZ model is applied to calculate triply differential cross sections for the ionization of argon 3p by electron impact. The approach is examined at intermediate

and low energies, taking advantage of the fact that argon is a well-studied atom with extensive experimental data available. Results from [1] are presented, highlighting the model's capability to handle various projectiles and collision energies under asymmetric coplanar kinematics.

## 3.3.1 Target wave function and variable charge

#### 3.3.1.1 Target wave function

Let us consider the argon atom (Z=18), whose electronic configuration is  $1s^22s^23s^22p^63p^6$ . The active electron in this atom is described using Clementi's Hartree-Fock wave functions with a Slater-type basis (Equation 1.63). The parameters associated with Clementi's wave functions noted as  $n_{ik}$ ,  $l_{ik}$ ,  $m_{ik}$ ,  $\xi ik$ ,  $\beta_{ik}$ , along with the ionization energies, are listed in table 3.2

n	l	m	ξ	(1s)	(2s)	(3s)	(2p)	(3p)
3	0	0	18.000	0.97453	-0.27660	0.08642		
3	0	0	21.2848	0.01878	-0.00224	0.00232		
3	0	0	15.5021	0.02233	0.04716	-0.02369		
3	0	0	11.2367	-0.00310	0.36490	-0.10542		
3	0	0	7.5066	0.00215	0.63126	-0.28841		
3	0	0	4.7029	-0.00094	0.04500	-0.05813		
3	0	0	3.2138	0.00038	-0.00186	0.68983		
3	0	0	1.9931	-0.00001	0.00088	0.47773		
2	1	m	9.0000				0.64951	-0.18072
4	1	m	15.0000				0.01298	-0.01234
4	1	m	11.9644				0.02669	0.02183
4	1	m	8.7924				0.28421	-0.12559
4	1	m	6.3011				0.12881	0.10518
4	1	m	3.4327				0.00219	0.58041
4	1	m	1.9409				0.00008	0.46149
4	1	m	1.0309				-0.00002	0.02249
Ioi	Ionization energies (a.u.)		118.61039	12.32219	1.27735	0.957150	0.59102	

**Table 3.2:** Parameters of Clementi's wave functions and ionization energies of the atomic orbitals of the argon atom

#### 3.3.1.2 Variable charge

The static potential in Equation 2.13 for the ionization of Ar 3p is calculated and written as:

$$U(r_1) = \frac{1}{4\pi} \int \left[ -\frac{18}{r_1} + 2 \int \frac{|\phi_{1s}|^2}{|\mathbf{r} - \mathbf{r}_1|} d\mathbf{r} + 2 \int \frac{|\phi_{2s}|^2}{|\mathbf{r} - \mathbf{r}_1|} d\mathbf{r} \right]$$
$$+ 6 \int \frac{|\phi_{2p}|^2}{|\mathbf{r} - \mathbf{r}_1|} d\mathbf{r} + 2 \int \frac{|\phi_{3s}|^2}{|\mathbf{r} - \mathbf{r}_1|} d\mathbf{r} + 5 \int \frac{|\phi_{3p}|^2}{|\mathbf{r} - \mathbf{r}_1|} d\mathbf{r} \right] d\Omega_e$$
$$= -\frac{Z(r_1)}{r_1}.$$
(3.3)

and the variable charge Z(r) can be expressed as

$$\begin{cases}
Z_e/s(r) = 18 - 2Z_{1s}(r) - 2Z_{2s}(r) - 6Z_{2p}(r) - 2Z_{3s}(r) - 5Z_{3p}(r) \\
Z_i(r) = 18 - 2Z_{1s}(r) - 2Z_{2s}(r) - 6Z_{2p}(r) - 2Z_{3s}(r) - 6Z_{3p}(r)
\end{cases}$$
(3.4)

In our model, the ejected and scattered electrons experience a charge of Z=N at the center of the target, which gradually reduces to Z=1 asymptotically. Meanwhile, the incident electron perceives a charge of Z=N at the center but Z=0 at large distances. These varying charges are denoted as  $Z_i(r)$ ,  $Z_s(r)$ , and  $Z_e(r)$ , corresponding to the incident, scattered, and ejected electrons, respectively.

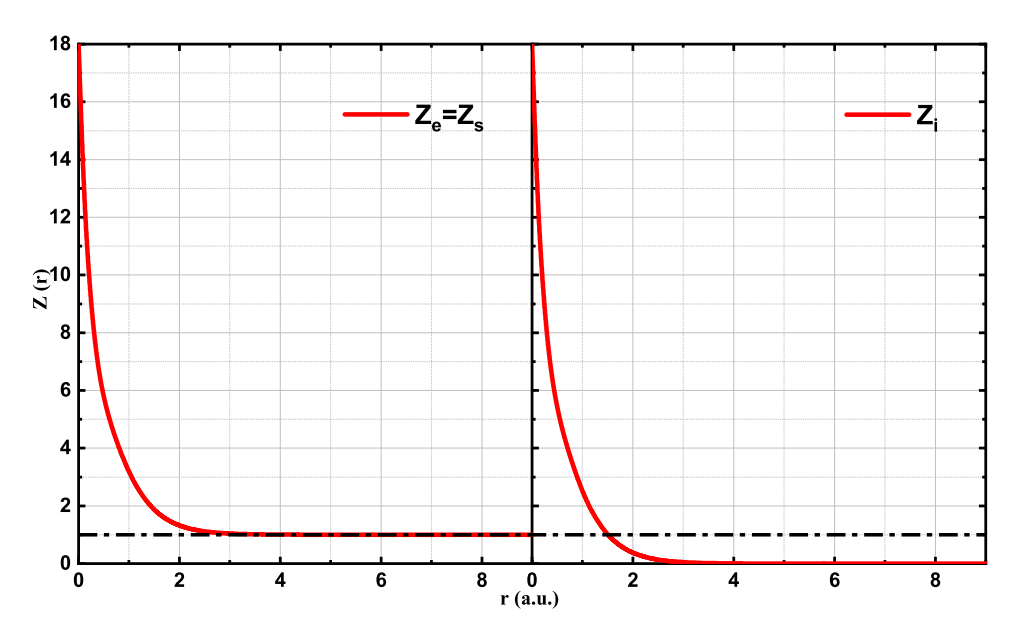


**Figure 3.5:** Variable charge experienced by the incident electron, the scattered electron, and the ejected electron during the ionization process of Ar 3p.

In Fig. 3.5, we present the variable charge Z(r) for the continuum electrons. It is shown that  $Z_s(r)$  and  $Z_e(r)$  decrease from Z=18 to Z=1, while  $Z_i(r)$  decreases from Z=18

to Z=0.

#### 3.3.2 Results and discussion

#### 3.3.2.1 Intermediate energy

First, we start with the intermediate-energy kinematics. We have calculated the TDCS using the 3CWZ model. The obtained results are now presented and discussed by considering various kinematic conditions in an asymmetric coplanar geometry (see Figure 1.3). Figure 3.6 shows the calculated TDCS results with an incident energy of approximately 721 eV and an ejection energy of 205 eV, compared to experimental data for scattering angles of 3°, 6°, and 9° [6], as well as with the DWB2-RM and DWBA-G [9] theoretical models. The kinematics in Figure 3.6 are characterized by a large momentum transfer (K = 1.27, 1.4, and 1.6 au) and a significant recoil momentum absorbed by the atom (up to q = 5.48 au). This indicates that the recoil ion plays a crucial role in the reaction. Therefore, in this case PCI is expected to strongly influence the TDCS, as the ejected and scattered electrons have relatively close energies. A detailed analysis of Figure 3.6 reveals that, overall, the DWB2-RM model provides a reasonable description of several aspects of the TDCS. However, in all cases, it predicts a binary peak that is significantly larger than that of the recoil region, which is in clear contradiction with the experimental data.

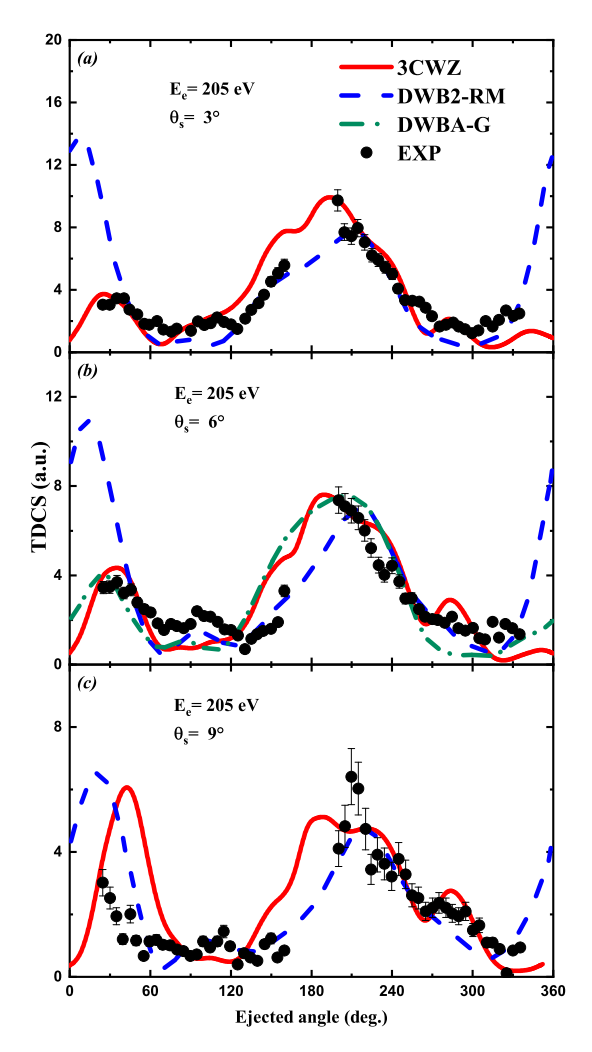


Figure 3.6: TDCS for the ionization of argon 3p as a function of the ejection angle, at fixed scattering and ejected energies 500 eV and 205 eV, respectively. The scattering angles are fixed at (a)  $\theta_s = 3^{\circ}$ , (b)  $\theta_s = 6^{\circ}$ , and (c)  $\theta_s = 9^{\circ}$ . Theoretical results are red solid line (3CWZ), green dash-dot line (DWBA-G), and green dashed line (DWB2-RM). The experimental data shown as black circles from [6], have been normalized for the best visual fit with theory.

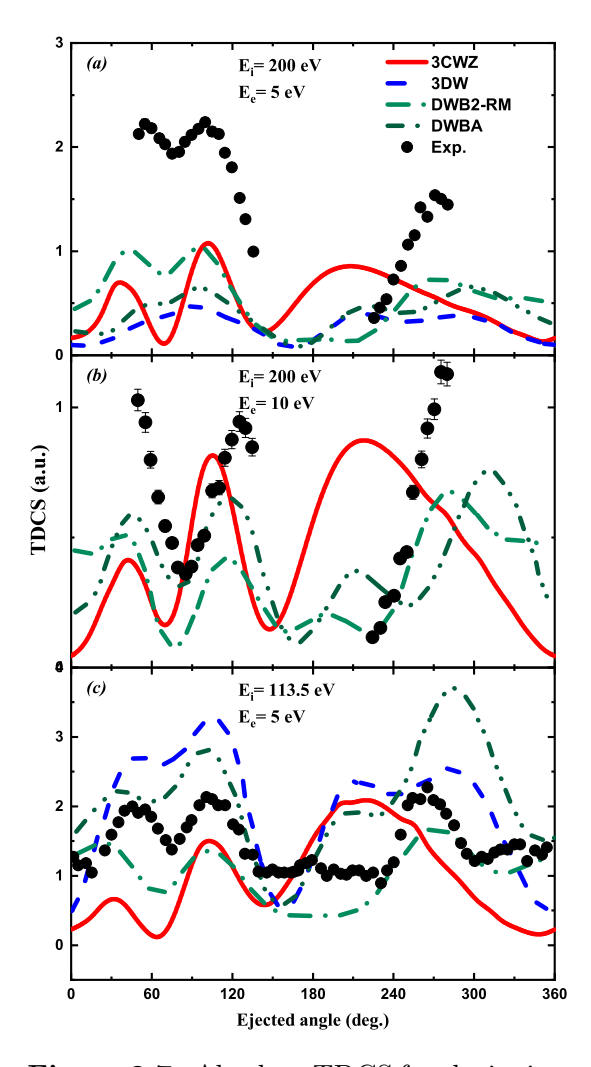


Figure 3.7: Absolute TDCS for the ionization of argon 3p as a function of the ejection angle at a fixed scattering angle  $\theta_s = 15^{\circ}$ . The incident and ejected electrons have respective energies: (a)  $E_i = 200eV$  and  $E_e = 5eV$ , (b)  $E_i = 200eV$  and  $E_e = 10eV$ , (c)  $E_i = 113.5$  and  $E_e = 5eV$ . Theoretical results are represented by a red solid line (3CWZ), a blue dashed line (3DW), a green dash-dot line (DWB2-RM), and a green dash-dot-dot line (DWBA). The experimental data are shown as black circles.

Furthermore, it can be observed that the 3CWZ model reproduces the TDCS well across most of the angular distribution, particularly in describing the peaks in both the binary and recoil regions, which are much better captured compared to the DWB2-RM model. On the other hand, the DWBA-G model (for which results are available only for certain cases) appears to provide predictions that are relatively close to both the experimental

data and the 3CWZ model, particularly in panel (b). To better interpret these findings, it is important to recall that the DWB2-RM model is a powerful approach generally capable of accurately describing the (e,2e) reaction. However, it does not account for (PCI), which plays a significant role in this specific case. In contrast, the DWBA-G model is a fully distorted wave approach in which PCI is incorporated through the Gamow factor. While the Gamow factor's strong violation of normalization makes DWBA-G unsuitable for absolute measurements comparisons, the model remains effective for comparing relative data, such as those considered in this study.

Now, we examine the ionization process under kinematic conditions of lower momentum transfer. Figure 3.7 compares the 3CWZ model with absolute data at impact energies of 200 eV and 113.5 eV, using experimental data from [2], alongside the 3DW, DWBA, and DWB2-RM models, clearly none of the models fully reproduces the absolute magnitude of the TDCS. In general, the 3CWZ model qualitatively captures the double-peak structure in the binary region, although the second binary peak is consistently larger than the first across all examined kinematic conditions. At an impact energy of 200 eV (panels a and b), all models tend to underestimate the measured data; however, the 3CWZ model reproduces the double binary peak relatively well, with its predictions in the binary region closely matching those of the DWB2-RM model. In contrast, the DWBA and 3DW models yield nearly identical shapes and magnitudes for the TDCS. Surprisingly, the sophisticated 3DW model fails to reproduce the double binary peak in panel (a). While the DWBA model exhibits similar behavior to 3DW at  $E_e = 10$  eV (panel a), it manages to capture the double binary peak at  $E_e = 5$  eV (panel b). At a projectile energy of 113.5 eV, similar trends are observed, although the absolute data are closer to the predictions of all models. Additionally, the 3CWZ and DWB2-RM models tend to underestimate the data, whereas the 3DW and DWBA models predict significantly higher intensities (panel c). In summary, although the 3CWZ model does not precisely reproduce the absolute magnitude of the TDCS, it qualitatively captures its shape particularly in the binary region and its performance is comparable to that of other advanced theories. In order to gain deeper insight into the dynamics of the (e, 2e) reaction, we study the ionization process at an impact energy of 195 eV. At this energy, experiments have been performed using a reaction microscope specifically designed for electron-impact measurements [7]. Consequently, new kinematic conditions beyond the coplanar geometry are examined to provide comprehensive information on the ionization dynamics. A three-dimensional TDCS image is presented as a function of the emission solid angle  $(\theta_e, \phi_e)$  for a fixed scattering angle  $\theta_s$ . For a more detailed comparison, TDCS cuts in three orthogonal planes are also provided: the xz plane (scattering plane), the yz plane (half-perpendicular plane), and the xy plane (full-perpendicular plane).

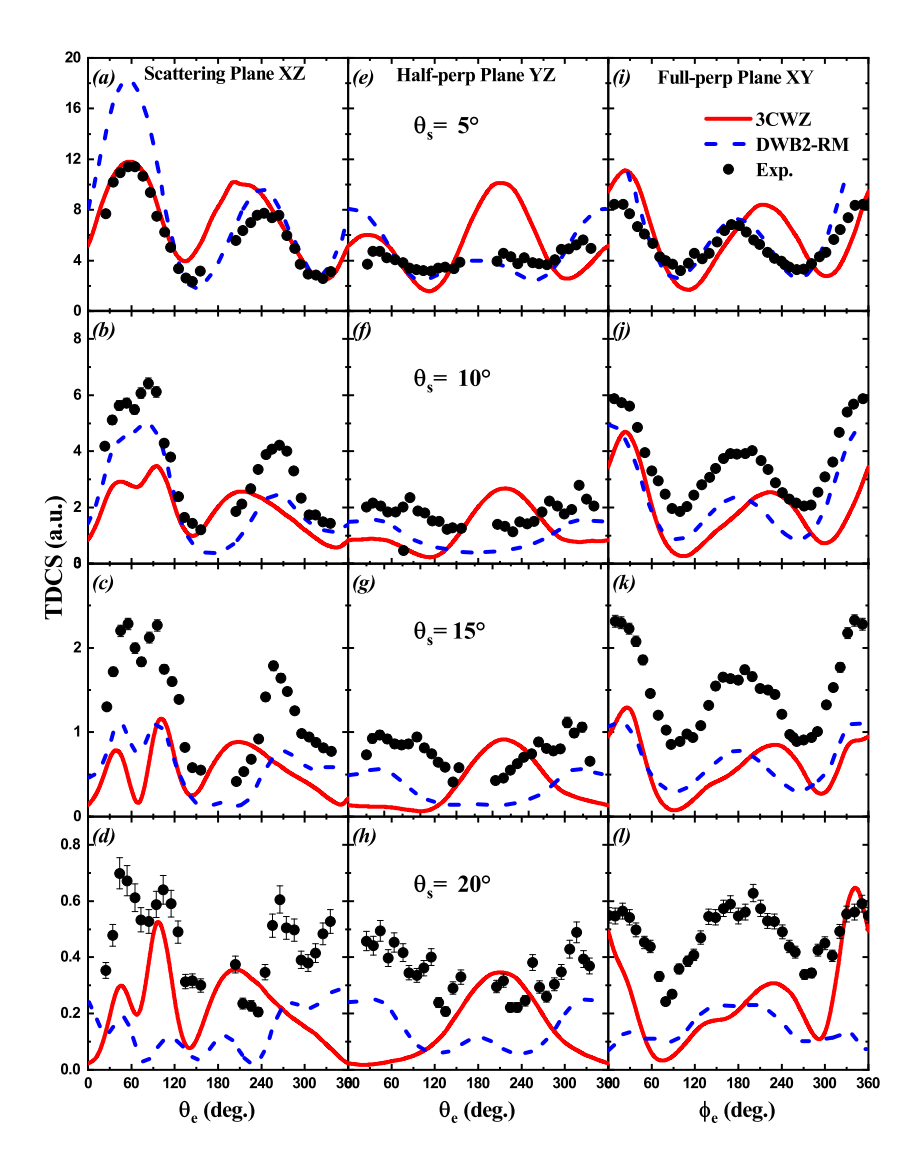


Figure 3.8: Absolute TDCS, shown as cuts of the 3D image, for the ionization of argon 3p at an incident energy of  $E_i = 195$  eV, plotted as a function of the ejection angles  $(\theta_e, \phi_e)$ . The projectile is scattered at angles of  $5^{\circ}$ ,  $10^{\circ}$ ,  $15^{\circ}$ , and  $20^{\circ}$ , in coincidence with an ejected electron of  $E_e = 10$  eV. The left, center, and right columns correspond to the scattering (xz) plane, half-perpendicular (yz) plane, and full-perpendicular (xy) plane, respectively. Theoretical results are shown as a black solid line (3CWZ) and a red dashed line (DWB2-RM), while experimental data (black circles) are taken from [7].

Figure 3.8 presents absolute TDCS cuts in three perpendicular planes at an ejection energy of  $E_e = 10$  eV, with  $\phi_e = 0$  along the x axis, and for scattering angles of 5°, 10°, 15°, and 20°. The 3CWZ results are compared with both experimental data and DWB2-RM predictions. In the xz plane (left column), the 3CWZ model agrees well with experiment at lower scattering angles, accurately reproducing the binary peak, and as the scattering angle increases (and thus the momentum transfer), the model's performance diminishes, although it still captures the double-peak structure characteristic of the p shell in argon

more effectively than DWB2-RM. The recoil peak, however, is slightly shifted to lower angles. In the yz plane (center column), DWB2-RM more closely matches the overall shape, while the 3CWZ model overestimates the recoil peak and struggles to reproduce the binary region except at 5°, where a peak nearly matching the experimental data emerges. Although DWB2-RM better reproduces the binary and recoil peaks in shape, it shows notable discrepancies in magnitude. Moreover, the 3CWZ results are shifted and not symmetric about 180° in all cases. Finally, in the xy plane (right column), the agreement with experimental data is mixed for both models. While DWB2-RM matches the data reasonably well at lower scattering angles (5° and 10°), it underestimates the measurements by up to a factor of two at higher scattering angles. In contrast, the 3CWZ model shows better agreement at  $\theta_s = 20^\circ$ , indicating that none of the models provides a uniformly superior description across all kinematic conditions. As observed in the yz plane, the 3CWZ results are shifted and not symmetric about 180° in all cases.

### 3.4 Conclusion

The application of the 3CWZ model to the ionization of neon and argon atoms demonstrates its potential for investigating electron impact ionization processes. For neon, the model successfully reproduces key features of the TDCS and outperforms conventional models such as DWBA and DWB2-RM, although it exhibits limitations in accurately predicting peak details in the recoil region at low energies (e.g., 65 eV), indicating the need for further refinement in this regime. For argon, the 3CWZ model effectively captures the qualitative shape of the TDCS at intermediate energies. However, discrepancies in absolute magnitudes and shifts in peak positions especially in the full and half-perpendicular planes at 195 eV indicate that the model does not yet fully capture all kinematic complexities. Overall, the 3CWZ model represents a promising advancement by balancing computational efficiency with reasonably good results. Nevertheless, further development is required to achieve quantitative precision across all energy regimes and geometries. These findings provide a solid foundation for extending the model to molecular targets, which will be explored in depth in the next chapter through an intensive study of water molecule ionization at low impact energies.

## **Bibliography**

- [1] K. Bechane, S. Houamer, T. Khatir, A. Tamin, and C. Dal Cappello. *Phys. Rev. A*, **109**:012812, 2024.
- [2] R. L. Hargreaves, M. A. Stevenson, and B. Lohmann. J. Phys. B: At. Mol. Opt. Phys, 43:205202, 2010.
- [3] X. Ren, S. Amami, O. Zatsarinny, T. Pflüger, M. Weyland, W. Yong Baek, H. Rabus, K. Bartschat, D. H. Madison, and A. Dorn. Phys. Rev. A, 91:032707, 2015.
- [4] T. Pflüger, O. Amami, O. Zatsarinny, K. Bartschat, A. Senftleben, X. Ren, J. Ullrich, and A. Dorn. *Phys Rev Lett.*, **110**:153202, 2013.
- [5] A. Dutta, B. Nath, and C. Sinha1. Phys. Rev. A, 64:042714, 2013.
- [6] F. Catoire, E. M. Staicu Casagrande, M. Nekkab, C. Dal Cappello, K. Bartschat, and A. Lahmam Bennani. J. Phys. B: At. Mol. Opt. Phys., 39:2827, 2006.
- [7] X. Ren, A. Senftleben, T. Pflüger, A. Dorn, K. Bartschat, and J. Ullrich. Phys. Rev. A, 83:052714, 2011.
- [8] R. D. DuBois and O. G. de Lucio. Atoms, 9:78, 2021.
- [9] A. S. Kheifets, A. Naja, E. M. Staicu Casagrande, and A. Lahmam-Bennani. J. Phys. B: At. Mol. Opt. Phys., 41:145201, 2008).

## Chapter 4

# Electron-impact ionization of water molecule

## 4.1 Introduction

Compared to atoms, (e,2e) studies on molecules <sup>1</sup> are relatively scarce due to experimental challenges, such as the close spacing of electronic states and contributions from rotational and vibrational excitations, as well as the inherent difficulty in theoretically describing multicenter continuum states. TDCS measurements have been reported for small molecules [1–4] and, more recently, for increasingly complex systems [5–11]. Water is especially important because it makes up about 70% of the tissue in many living organisms, including the human body [12].

In the previous chapter, we investigated (e,2e) processes on neon and argon atoms using the 3CWZ model, which offers a significant computational advantage over some other methods by providing TDCS predictions for arbitrary kinematics at low time cost. In this chapter, we extend the 3CWZ model to molecular targets while maintaining this numerical efficiency. The resulting model, named M3CWZ, is thoroughly tested by calculating TDCS for the  $1b_1$  and  $3a_1$  orbitals of the water molecule. We analyze both the well-known experiments of Lohman et al. [13], and recent experiments performed at low impact energies. In the latter, the data cover nearly the entire  $4\pi$  solid angle and are reported on a relative scale at 81~eV impact energy [14] and on an absolute scale at 65~eV impact energy [15]. These two low energy data sets correspond to the dipole regime, characterized by small momentum transfer; and represent on one hand a stringent challenge for theory, and on the other hand are of crucial practical interest for example in radiation

<sup>&</sup>lt;sup>1</sup>Part of this chapter (in particular section 4.5) is reproduced from: A. Tamin, S. Houamer, T. Khatir, L. U. Ancarani, and C. Dal Cappello, "Electron-impact ionization of water molecules at low impact energies." *J. Chem. Phys.* **161**, 164305 (2024), with the permission of AIP Publishing.

damage in biological systems.

Finally, in the last section, we present an under development modified version of the M3CWZ model, which uses a hybrid approach combining Coulomb waves with a variable charge and distorted waves.

## 4.2 Importance of water molecules

Water molecule  $H_2O$  is the most abundant molecular compound on earth, and also makes up roughly 70% of the human biological tissue, so that it plays a central role in many research fields such as biology, atmospheric chemistry, and planetary science.

The interaction of electrons with water molecules is of fundamental importance for understanding radiation-induced damage in biological tissues. When high-energy radiation penetrates living systems, it generates a large number of secondary electrons, which can inflict cellular damage either directly, through ionization of critical biomolecules, or indirectly by inducing the formation of reactive chemical species by initiating rapid reactions that often lead to the formation of stable molecules like  $H_2$  and  $O_2$ , or ionic fragments such as  $H^+$  and  $O^-$  [16]. These products frequently result from the destruction of water molecules surrounding DNA, which causes radiation-induced damage to DNA and other cellular components. The assessment of the rate of radio-induced effects on living matter requires the acquisition of both theoretical and experimental data on the single and multiple ionization cross sections of the water molecule.

Beyond biological systems, water plays a significant role in nuclear reactors [17] and radioactive waste management. There, it is commonly used as a coolant and moderator, but its ionization under high-energy radiation generates radicals that can contribute to material corrosion and hydrogen gas production, posing notable safety concerns. In atmospheric and interstellar chemistry, electron impact ionization of water vapor contributes to ionospheric reactions and astrochemical pathways [18], affecting both planetary atmospheres and the chemistry of icy celestial bodies.

## 4.3 Theoretical description of the water molecule

The water molecule is formed through the following reaction:

$$H_2 + \frac{1}{2}O_2 \to H_2O$$
 (4.1)

The ground state electronic configuration of a molecule, is generally determined using molecular orbital (MO) theory within the MO-LCAO framework. This method constructs

molecular orbitals (MO) as linear combinations of atomic orbitals (LCAO) derived from constituent atoms of the molecule. For water the method suggests that the most accurate wave function description is achieved by forming hybrid orbitals by combining the hydrogen atom's 2s orbital with the three 2p orbitals originating from the oxygen atom, leading to four equivalent hybrid orbitals known as  $2sp^3$ . Such hybridization helps in explaining the bent geometry and electronic distribution observed in water molecule. Furthermore, leveraging the symmetry characteristics of the  $H_2O$  molecule described comprehensively by group theory principles the ten electrons in its ground state are organized into five distinct molecular orbitals:

$$(1a_1)^2(2a_1)^2(1b_2)^2(3a_1)^2(1b_1)^2 (4.2)$$

#### Molecular Orbitals for Water

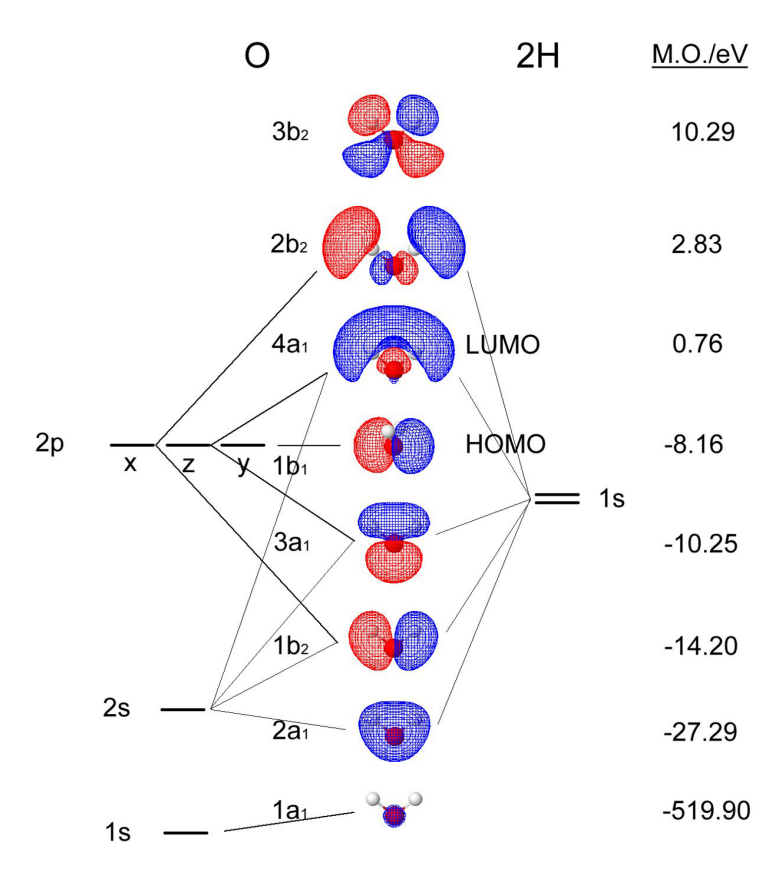


**Figure 4.1:** Molecular orbital diagram of water  $H_2O$  (Adapted from ChiralJon , licensed under CC BY 2.0) .

The ionization energies required for removing electrons from each molecular orbital of water are as follows: 558.5, 32.2, 18.5, 14.7, and 12.6 eV [19]. The  $1b_1$  orbital represents the

highest occupied molecular orbital (HOMO), whereas the next higher-energy orbital,  $4a_1$ , represents the lowest unoccupied molecular orbital (LUMO). Higher-energy orbitals, such as  $4a_1$ ,  $2b_2$ , and  $3b_2$  (Fig. 4.1), remain unoccupied in the ground state. These unoccupied orbitals become particularly relevant in studies of excited states, spectroscopic properties, and chemical reactivity. The electronic configuration given by Eq. 4.2 and presented in Fig. 4.1 aligns closely with experimental observations and theoretical predictions of molecular electronic structure [20]. The MO-LCAO construction frequently involves substantial computational complexity, particularly when dealing with larger or structurally complicated molecules. A prominent challenge in such calculations arises from evaluating multicenter integrals. Even for relatively small molecules, accurately determining these integrals can pose considerable numerical difficulties due to their complex spatial dependencies and mathematical formulations. To effectively address this computational issue, two main strategies have been widely adopted:

- Transforming the integrals into more computationally manageable forms by introducing suitable coordinate changes or mathematical substitutions, thereby simplifying the evaluation of multicenter interactions.
- Reducing the complexity of the multicenter molecular system by reformulating the problem into an equivalent atomic scenario, often by employing a simplified, monocentric (single-center) basis set. This approach significantly streamlines integral calculations and provides more straightforward numerical tools.

Within the context of the Born–Oppenheimer approximation, where nuclear and electronic motions are treated separately, the multicenter Hamiltonian for a general polyatomic molecule can be explicitly represented as follows:

$$H = -\sum_{i} \frac{\nabla_{i}^{2}}{2} - \sum_{\alpha,i} \frac{Z_{\alpha}}{|\mathbf{r}_{i} - \mathbf{r}_{\alpha}|} + \sum_{i < j} \frac{1}{|\mathbf{r}_{i} - \mathbf{r}_{j}|} + \sum_{\alpha < \beta} \frac{Z_{\alpha} Z_{\beta}}{|\mathbf{r}_{\alpha} - \mathbf{r}_{\beta}|}$$
(4.3)

the indices (i, j) represent electrons, while  $(\alpha, \beta)$  denote atomic nuclei. For some molecules, one may consider a monocentric approach whereby all contributions are expressed in terms of a single set of spherical coordinates around a single center. While the choice of the center of coordinates is not strictly unique, it generally corresponds to the position of the heaviest nucleus in the molecule. This simplified, monocentric approach has proven particularly effective for molecules of the type  $AH_n$ , such as methane  $(CH_4)$ , ammonia  $(NH_3)$ , and water  $(H_2O)$  [21]. For these molecules, calculated properties like total molecular energy and bond lengths have shown excellent agreement with experimental observations. Table 4.1 provides a comparison for the water molecule.

Property	Values reported by Moccia	Experimental values
$\mu$ (a.u.)	0.8205	0.728
O–H (a.u.)	1.814	1.810
H–H (a.u.)	2.907	2.873
H–O–H bond angle (degrees)	106.53	105.5

**Table 4.1:** Comparison of calculated molecular properties of  $H_2O$  from Moccia [21] with corresponding experimental values. (more deatils in [22]).

In this study, we use the Moccia [21] monocentric functions (see subsection 1.7.2.1), and the values of the coefficients  $a_{ij}$  and  $\xi_{ij}$  corresponding to the various quantum numbers  $n_{ij}$ ,  $l_{ij}$ , and  $m_{ij}$ , are reported in table 4.2

$n_{ij}$	$l_{ij}$	$m_{ij}$	ξ	$1a_1$	$2a_1$	$3a_1$	$1b_2$	$1b_1$
1	0	0	12.600	0.05167	0.01889	-0.00848		
1	0	0	7.450	0.94656	-0.25592	0.08241		
2	0	0	2.200	-0.01708	0.77745	-0.30752		
2	0	0	3.240	0.02497	0.09939	-0.04132		
2	0	0	1.280	0.00489	0.16359	0.14954		
2	1	0	1.510	0.00107	0.18636	0.79979		
2	1	0	2.440	-0.00244	-0.00835	0.00483		
2	1	0	3.920	0.00275	0.02484	0.24413		
3	2	0	1.600	0.00000	0.00695	0.05935		
3	2	0	2.400	0.00000	0.00215	0.00396		
3	2	2	1.600	-0.00004	-0.06403	-0.09293		
3	2	2	2.400	0.00003	-0.00988	0.01706		
4	3	0	1.950	-0.00004	-0.02628	-0.01929		
4	3	2	2.950	-0.00008	-0.05640	-0.06593		
2	1	-1	1.510				0.88270	
2	1	-1	2.440				-0.07083	
2	1	-1	3.920				0.23189	
3	2	-1	1.600				0.25445	
3	2	-1	2.400				-0.01985	
4	3	-1	1.950				0.04526	
4	3	-1	2.950				-0.06381	
2	1	1	1.510					0.72081
2	1	1	2.440					0.11532
2	1	1	3.920					0.24859
3	2	1	1.600					0.05473
3	2	1	2.400					0.00403
4	3	1	1.950					0.00935
4	3	3	1.950					-0.02691

**Table 4.2:** Values of coefficients  $a_{ij}$  and exponents  $\xi_{ij}$  for the molecular orbitals of water as provided by Moccia [23].

## 4.4 Theoretical model

The ionization of a water molecule by electron impact, assuming it is in its ground state, is illustrated as:

$$e_i + H_2O \to H_2O^+ + e_e + e_s$$
 (4.4)

where  $e_i$ ,  $e_s$ , and  $e_e$  represent the incident, scattered, and ejected electrons, respectively. Their associated momenta are denoted by  $\mathbf{k}_i$ ,  $\mathbf{k}_s$ , and  $\mathbf{k}_e$ , and they are required to fulfill momentum  $\mathbf{k_i} = \mathbf{k_s} + \mathbf{k_e} + \mathbf{q}$ , and energy conservation laws  $E_i = E_s + E_e + Binding$  energy. For highly asymmetric kinematics, the outgoing electrons can be clearly distinguished: one as a fast scattered electron and the other as a slow ejected electron. In this case, exchange effects between the scattered and ejected electrons can often be neglected. However, at low impact energies, this approach is no longer valid, and exchange effects between the scattered and ejected electrons must be taken into account. The ionization of the target may also proceed via a capture process [24], whereby the incident electron is captured into a bound state while two initially bound electrons are emitted. The fourfold differential cross section (4DCS) in the M3CWZ is given by Eq. 2.25 (see chapter 2 section 2.6 for details). In the case of ionization from the orbital  $3a_1$  the static potential is written as:

$$U(r_{1}) = \frac{1}{4\pi} \int \left[ -\frac{2}{R} - \frac{8}{r_{1}} + 2 \int \frac{|\phi_{1a_{1}}|^{2}}{|\mathbf{r} - \mathbf{r}_{1}|} d\mathbf{r} + 2 \int \frac{|\phi_{2a_{2}}|^{2}}{|\mathbf{r} - \mathbf{r}_{1}|} d\mathbf{r} \right] + 2 \int \frac{|\phi_{1b_{2}}|^{2}}{|\mathbf{r} - \mathbf{r}_{1}|} d\mathbf{r} + \int \frac{|\phi_{3a_{1}}|^{2}}{|\mathbf{r} - \mathbf{r}_{1}|} d\mathbf{r} d\mathbf{r} \right] d\Omega_{e} = -\frac{Z(r_{1})}{r_{1}}, \qquad (4.5)$$

$$U(r_{1}) = \frac{1}{4\pi} \int \left[ -\frac{2}{r_{1}} - \frac{8}{R} + 2 \int \frac{|\phi_{1a_{1}}|^{2}}{|\mathbf{r} - \mathbf{r}_{1}|} d\mathbf{r} + 2 \int \frac{|\phi_{2a_{2}}|^{2}}{|\mathbf{r} - \mathbf{r}_{1}|} d\mathbf{r} + 2 \int \frac{|\phi_{1b_{2}}|^{2}}{|\mathbf{r} - \mathbf{r}_{1}|} d\mathbf{r} \right] d\mathbf{r} + 2 \int \frac{|\phi_{1b_{1}}|^{2}}{|\mathbf{r} - \mathbf{r}_{1}|} d\mathbf{r} + \int \frac{|\phi_{3a_{1}}|^{2}}{|\mathbf{r} - \mathbf{r}_{1}|} d\mathbf{r} d\mathbf{r} d\mathbf{r} d\mathbf{r} = -\frac{Z(r_{1})}{r_{1}}, \qquad (4.6)$$

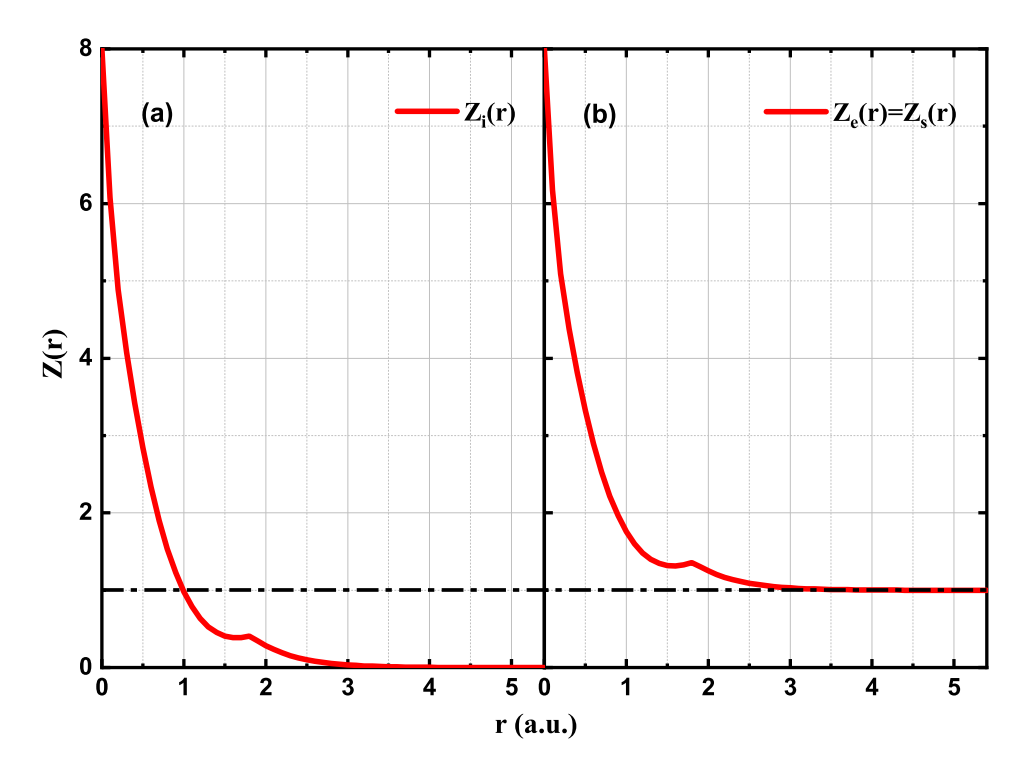


**Figure 4.2:** Variable charge Z(r) felt by the incident electron (a) and the outgoing electrons (b) during the ionization process for the  $3a_1$  molecular orbital of  $H_2O$ .

Figure 4.2 illustrates the variable charges employed in the present model for the ionization of the  $3a_1$  orbital of  $H_2O$  (the figure is similar for the  $1b_1$  orbital). The charge decreases from Z=8 at r=0 to an asymptotic value of Z=1 for the outgoing electrons ( $Z_e$  and  $Z_s$ ) and to Z=0 for the incident electron  $Z_i(r)$ . Near r=R=1.814 au, where R is the bond length of the molecule, the positive charge of the hydrogen nucleus generates a small kink, a feature obviously not observed in the case of atomic targets. The validity of using a variable charge approach in a three Coulomb waves model has been discussed in [25–27]. The transition amplitudes, as defined in equation 4.7, are evaluated using the Fourier transform formalism, which considerably streamlines the intermediate stages of the calculation (see Appendix A for details).

## 4.5 Results and discussions

The first step in this study is to test the proposed model for individual orbitals (i.e.,  $1b_1$ ,  $1b_2$ ,  $3a_1$ , and  $2a_1$ ). For this specific purpose, but without conducting an extensive comparative study, we consider the experiments performed at an impact energy of 250 eV, where the projectile is scattered at an angle  $\theta_s = 15^{\circ}$  in coincidence with an ejected electron of energy  $E_e = 10 \ eV$  for the  $2a_1$ ,  $1b_2$ , and  $1b_1$  orbitals, and  $E_e = 8 \ eV$  for

the  $3a_1$  orbital [13]. In these measurements, the momentum transfer is approximately 1.1 a.u.; all orbitals were resolved, and TDCSs were measured—on a relative scale—for the  $1b_1$ ,  $1b_2$ ,  $3a_1$ , and  $2a_1$  orbitals separately. The calculated TDCSs are presented in Figure 4.3 and compared to the experimental data, which are normalized, in each panel, at the binary peak. While no conclusion can be drawn regarding the absolute values, the overall shape agreement is good for the outer orbitals. However, for the inner  $2a_1$  orbital, the recoil peak is not well reproduced. This discrepancy in the case of inner orbitals for  $H_2O$  is attributed to the frozen-core approximation used in this study (see chapter one section 1.7), in which the outer valence electrons are treated as part of a frozen core and thus remain inactive [28].

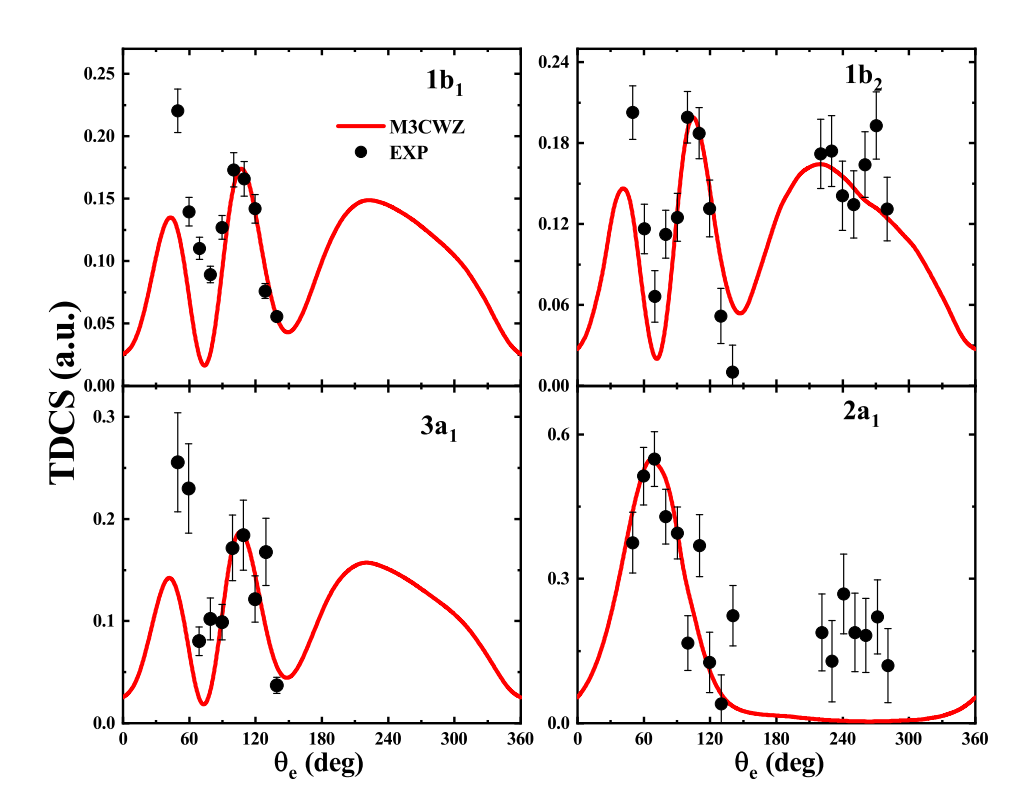
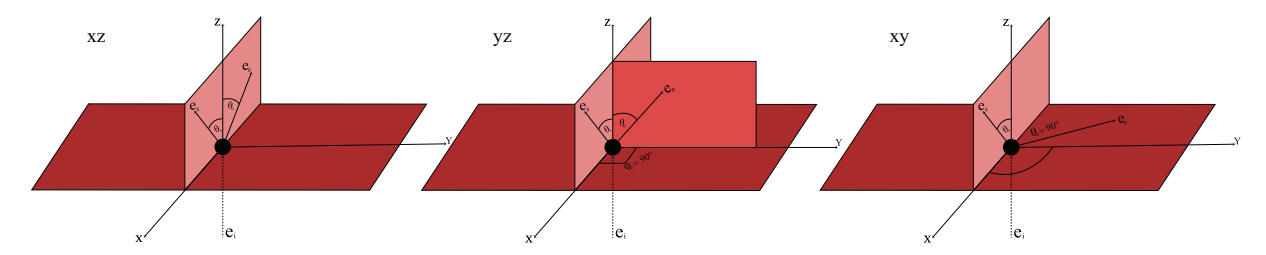


Figure 4.3: TDCS for electron-impact ionization of molecular orbitals of  $H_2O$  at 250 eV impact energy. The projectile is scattered at an angle  $\theta_s = 15^{\circ}$  in coincidence with the ejected electron with energy  $E_e = 10 \ eV$  (except for  $3a_1$  orbital where  $E_e = 8 \ eV$ ). Theoretical results of M3CWZ model (red solid line) [29] are compared with the relative scale measurements [13] normalized to the M3CWZ calculation in the binary region.

From Figure 4.3, we observe that the angular distributions for the  $1b_1$  and  $3a_1$  orbitals, considered separately, are very similar both experimentally and within the M3CWZ model. This similarity is attributed to their close ionization energies and the use of an orientation average, which minimizes the influence of the orbital shape. For the  $1b_2$  orbital, the M3CWZ model produces an overall shape in good agreement with the measured data,

including a recoil peak as pronounced as the binary peak.

Next, we examine the experiments performed at an impact energy of 81 eV [14]: 3D images of the TDCS have been measured as a function of the emission solid angle  $\Omega_e = (\theta_e, \phi_e)$  for scattering angles  $\theta_s = 6^{\circ}$  or  $\theta_s = 10^{\circ}$ , and ejected energies of  $E_e = 5 \ eV$  and 10 eV. To make the comparison with the data more comprehensive, three cuts of the 3D TDCS are presented in three orthogonal planes, namely the scattering xz plane, the half-perpendicular yz plane, and the full-perpendicular xy plane, as shown in Figure 4.4.



**Figure 4.4:** The orthogonal planes: the scattering (xz) plane, the half perpendicular (yz) plane and the full perpendicular (xy) plane.

Our results are displayed in Figure 4.5 and compared with the measured data [14] and the results calculated with the MTCDW and M3DW models [30]. We recall here that M3DW treats PCI exactly, whereas in the MCTDW approach PCI is modeled by a simple multiplicative Gamow factor (see Chapter One, Section 1.6). Here, the experimental data are on a relative scale and inter-normalized across all ejection energies as well as scattering angles. In other words, a single common factor is used to fix the relative magnitude of the measured data and the theoretical results. The global scaling factor is obtained by achieving a good visual fit of the data and the M3CWZ results in the full perpendicular xy plane at  $\theta_e = 10^{\circ}$  and  $E_e = 10 \ eV$  (the choice was already made in [30]). This scaling factor is found to be 0.285 and is subsequently applied to the three orthogonal planes in all other kinematics; all experiments are thereby consistently cross-normalized to each other.

In the full perpendicular xy plane (Fig. 4.5, left-hand column), the observed angular distributions are overall well reproduced by the M3CWZ model, with the best agreement observed in panel Fig. 4.5(d) for  $\theta_e = 10^{\circ}$  and  $E_e = 10 \ eV$ . Although no firm statement can be made regarding the magnitude agreement, once inter-normalized, the measured data and our theoretical results exhibit an overall agreement that can be considered acceptable. When comparing our TDCS with those obtained with the MCTDW and M3DW models, the situation is rather mixed: in most cases, our results show better agreement with the measured data, except for the kinematics of panel Fig. 4.5(b), where the MCTDW shape appears better. In the case of panel Fig. 4.5(d), the M3CWZ model

reproduces the data in a manner almost similar to MCTDW, while the M3DW model significantly underestimates the TDCS in the emission angle regions from  $0^{\circ}$  to  $10^{\circ}$  and from  $250^{\circ}$  to  $360^{\circ}$ . Concerning the absolute scale, the three theoretical calculations are of the same order of magnitude (the largest difference being a factor of about 1.5); our results are closer to those of the M3DW model at an ejection energy of  $E_e = 10 \ eV$  (panels Fig. 4.5(c) and Fig. 4.5(d)).

In the scattering xz plane (Fig. 4.5, central column), all the kinematical arrangements the experimental data exhibit features of binary and recoil lobes, a characteristic of dipole regimes. In these regimes the momentum transfer  $\mathbf{K} = \mathbf{k_i} - \mathbf{k_s}$  is rather small (in our case  $K \approx 0.37 - 0.54 \, au$ ); as a consequence, the residual ion strongly participates in the collision dynamics and elastically backscatters the ejected electron in the direction opposite to that of the momentum transfer. Furthermore, it has already been pointed out in [14] that nonfirst-order effects in the electron-target interaction are present since the observed binary peaks are shifted with respect to the direction of the momentum transfer K; one such effect is included in our modeling via the PCI to all orders of perturbation theory. One initial observation from the figure is that the M3CWZ model exhibits a strong recoil peak in all kinematics, in quite good agreement with the experiments. The binary region is also fairly well reproduced, except for panel Fig. 4.5(f), corresponding to  $\theta_e = 10^{\circ}$  and  $E_e = 5 \text{ eV}$ , for which the ratio of the binary to recoil heights is underestimated. When comparisons are made with the M3DW and MCTDW models, it is evident that the latter features larger recoil peaks. Keeping in mind the way the measured data are inter-normalized, we may state that they overestimate the recoil relative to the binary region. A further notable difference among the models appears in the binary region: the M3DW model consistently presents a double binary peak across all kinematics, the M3CWZ model does so only in the kinematics of panel Fig. 4.5(f), and the MCTDW model does not display a double binary peak in any of the configurations.

In the half perpendicular yz plane (Fig. 4.5, right-hand column), we first notice that the data are symmetric about  $\theta_e = 180^{\circ}$ , with two symmetric maxima located near  $\theta_e = 90^{\circ}$  and  $\theta_e = 270^{\circ}$ . The M3CWZ calculations reproduce the overall TDCS shapes quite well; we also observe reasonable agreement in relative magnitudes at a scattering angle of  $\theta_s = 6^{\circ}$  [Figs. 4.5(i) and 4.5(k)], whereas for  $\theta_s = 10^{\circ}$  [Figs. 4.5(j) and 4.5(l)] the data are somewhat underestimated in the regions of low and high emission angles. In addition, the comparison with M3DW and MCTDW calculations indicates that the three theoretical models predict practically the same TDCS shapes and magnitudes, except for the case  $\theta_s = 6^{\circ}$  and  $E_e = 5$  eV [Fig. 4.5(i)], where the M3DW model substantially overestimates the TDCS in the central part (from 120° to 220°).

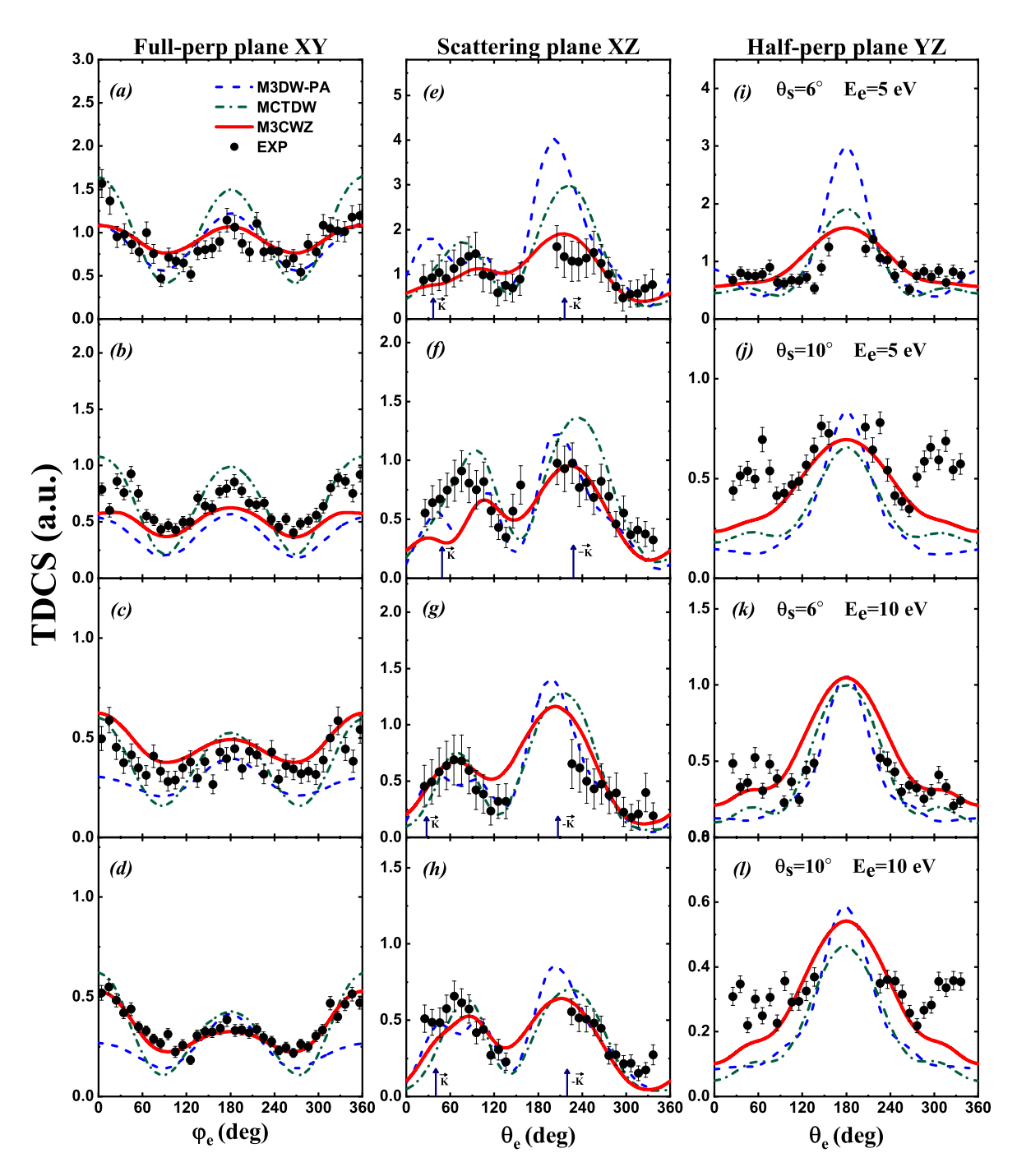


Figure 4.5: Summed TDCS (presented as cuts of the 3D image) for the ionization of  $1b_1$  and  $3a_1$  orbitals of  $H_2O$  as a function of the ejection angle at 81 eV impact energy. The projectile is scattered at angles  $\theta_s = 6^{\circ}$ , or  $\theta_s = 10^{\circ}$  in coincidence with the ejected electron with  $E_e = 5 \ eV$  or  $10 \ eV$ . Left-hand column in the full perpendicular (xy) plane. Central column: in the scattering (xz) plane. Right-hand column: in the half perpendicular (yz) plane. Theoretical results are red solid line (M3CWZ) [29], blue dashed line (M3DW as rescaled in [30]) and green dashed-dotted line (MCTDW) [30]. The cross normalized experimental data are black circles taken from [14]. In the central column (scattering plane), the direction of the momentum transfer  $\mathbf{K}$  and its opposite direction  $-\mathbf{K}$  are both indicated by an arrow.

To summarize the results presented in Fig. 4.5, it can be stated that the M3CWZ model is generally able to reproduce the measured TDCS shapes at  $81\ eV$  impact energy in most kinematical configurations. Moreover, it yields relative peak heights and overall magnitudes in the 12 considered configurations that satisfactorily match the inter-normalized experimental data. In the comparison of shape and magnitude with the M3DW and MCTDW results, some common characteristics emerge. However, no definite and general trend can be identified, as certain features are better described by one model or another, depending on the specific cut and kinematic configuration.

We now consider the second set of measurements, at 65 eV impact energy [15]. Since these data are provided on an absolute scale, the TDCS can be compared not only in shape but also in magnitude, providing an even stronger test of the present M3CWZ model (or any other model). As in the first set of measurements (at 81 eV impact energy), the present kinematics are characterized by a fairly low momentum transfer (from 0.5 to 0.87 au) and, thus, by the dipole regime. Figures 4.6-4.8 show the TDCSs in the scattering xzplane, the half perpendicular yz plane, and the full perpendicular xy plane, respectively. Figure 4.6 displays the TDCS as a function of the polar ejection angle  $\theta_s$  in the scattering xz plane for several sets of scattering angles ( $\theta_e = 10^{\circ}, 15^{\circ}, \text{ and } 20^{\circ}$ ) and ejection energies  $(E_s = 5, 10, \text{ and } 15 \text{ eV})$ . Our M3CWZ results are compared with experimental data as well as with the TDCS calculated using the M3DW and MCTDW-WM models [15]. We note that while the PCI is included and treated exactly in both the M3CWZ and M3DW approaches, in MCTDW-WM it is included approximately through the Ward-Macek factor [15]. Since this factor is known to violate the normalization, it is not recommended for comparisons with absolute measurements. However, the MCTDW-WM model has been used for comparison purpose in these particular kinematics by applying a scaling factor of 1.8 to achieve the best visual agreement with the data; in other words, the MCTDW-WM is used solely to test its ability to reproduce the TDCS shape qualitatively. It can be clearly observed in Fig. 4.6 that both experimental and theoretical TDCSs exhibit a pronounced recoil peak in all cases. The three models yield rather similar shapes and magnitudes, except that the M3DW calculations clearly overestimate the results of the M3CWZ and MCTDW-WM models in the emission angle range of approximately 180° to 220° in the kinematics of Figs. 4.6a–4.6e.

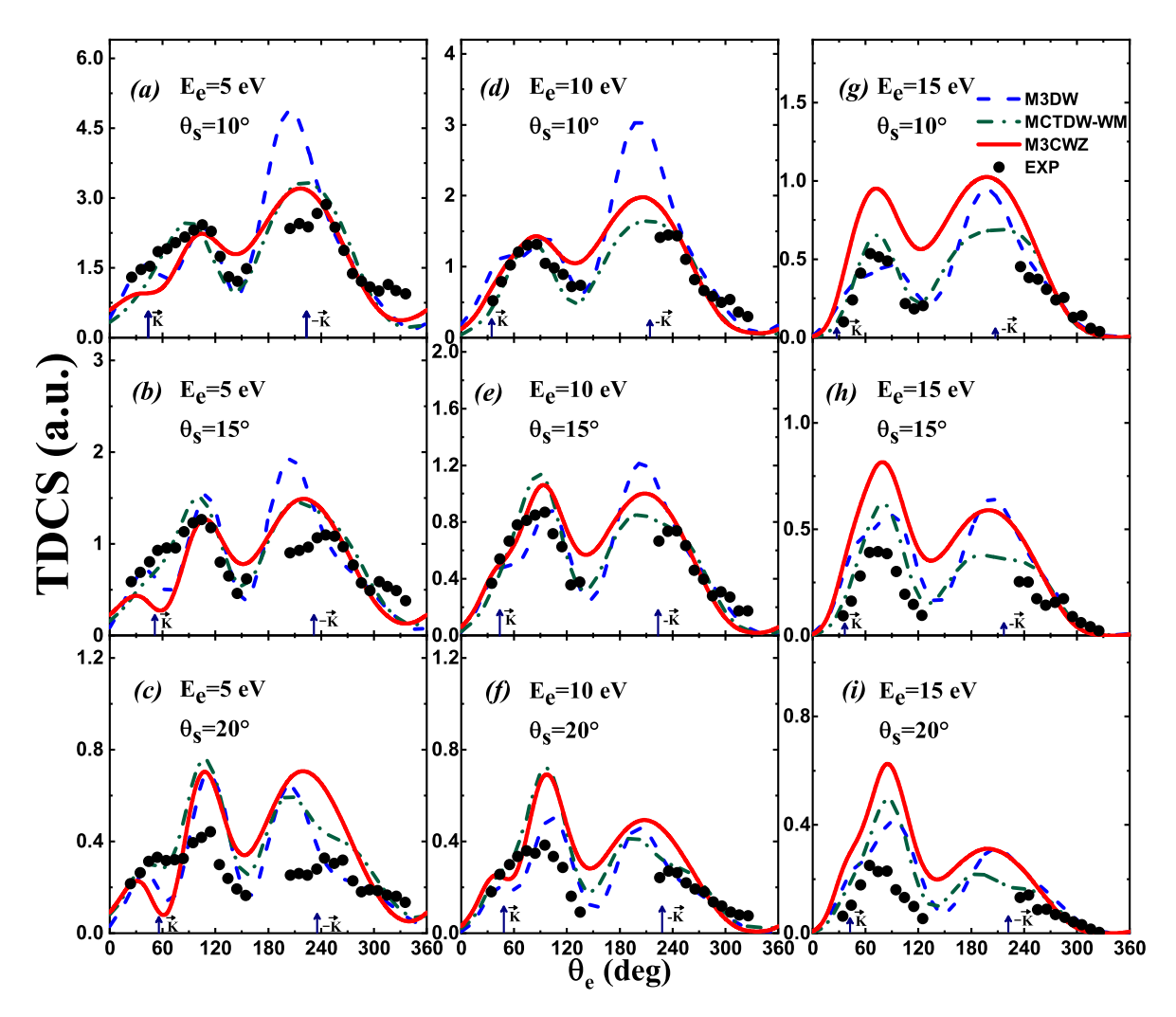


Figure 4.6: Absolute summed TDCS (presented as a cut of the 3D image in the scattering xz plane) for the ionization of  $1b_1$  and  $3a_1$  orbitals of  $H_2O$  as a function of the ejection angle at 65 eV impact energy. The projectile is scattered at angles  $\theta_s = 10^\circ$ ,  $15^\circ$ , or  $20^\circ$  from top to bottom, respectively, in coincidence with the ejected electron with energies  $E_s = 5$  eV (left-hand column),  $E_s = 10$  eV (middle column), and  $E_s = 15$  eV (right-hand column). Theoretical results are red solid line (M3CWZ) [29], blue dashed line (M3DW), [15] and green dashed-dotted line (MCTDW-WM). [15] The absolute experimental data are black circles taken from Ref. [15]. The direction of the momentum transfer  $\mathbf{K}$  and its opposite direction  $-\mathbf{K}$  are both indicated by an arrow.

In the binary region, the peak is strongly shifted relative to the momentum transfer direction. For some kinematics, the M3CWZ and M3DW models exhibit a hint of a double peak structure, which is related to the p-character of the  $1b_1$  and  $3a_1$  orbitals; however, this feature is not observed experimentally. In terms of magnitude, the three theoretical models predict practically the same TDCS amplitude in the binary region at 5 and 10 eV ejection energies, with the exception of the kinematics in Fig. 4.6f, where the M3DW model slightly underestimates the results compared to the other two models (keeping

in mind that, following Ref. [15], the MCTDW-WM calculations have been multiplied by a global factor of 1.8). On the other hand, at 15 eV ejection energy, the M3DW and MCTDW-WM results agree better with the measured data than the M3CWZ predictions. To summarize, in the scattering xz plane the experimental data in the recoil region are overall better reproduced by the M3CWZ and MCTDW-WM models than by the M3DW model. In the binary region, all theoretical results are quite similar, except at 15 eV ejected energy, where the M3DW and MCTDW-WM models are closer in magnitude to the experiments.

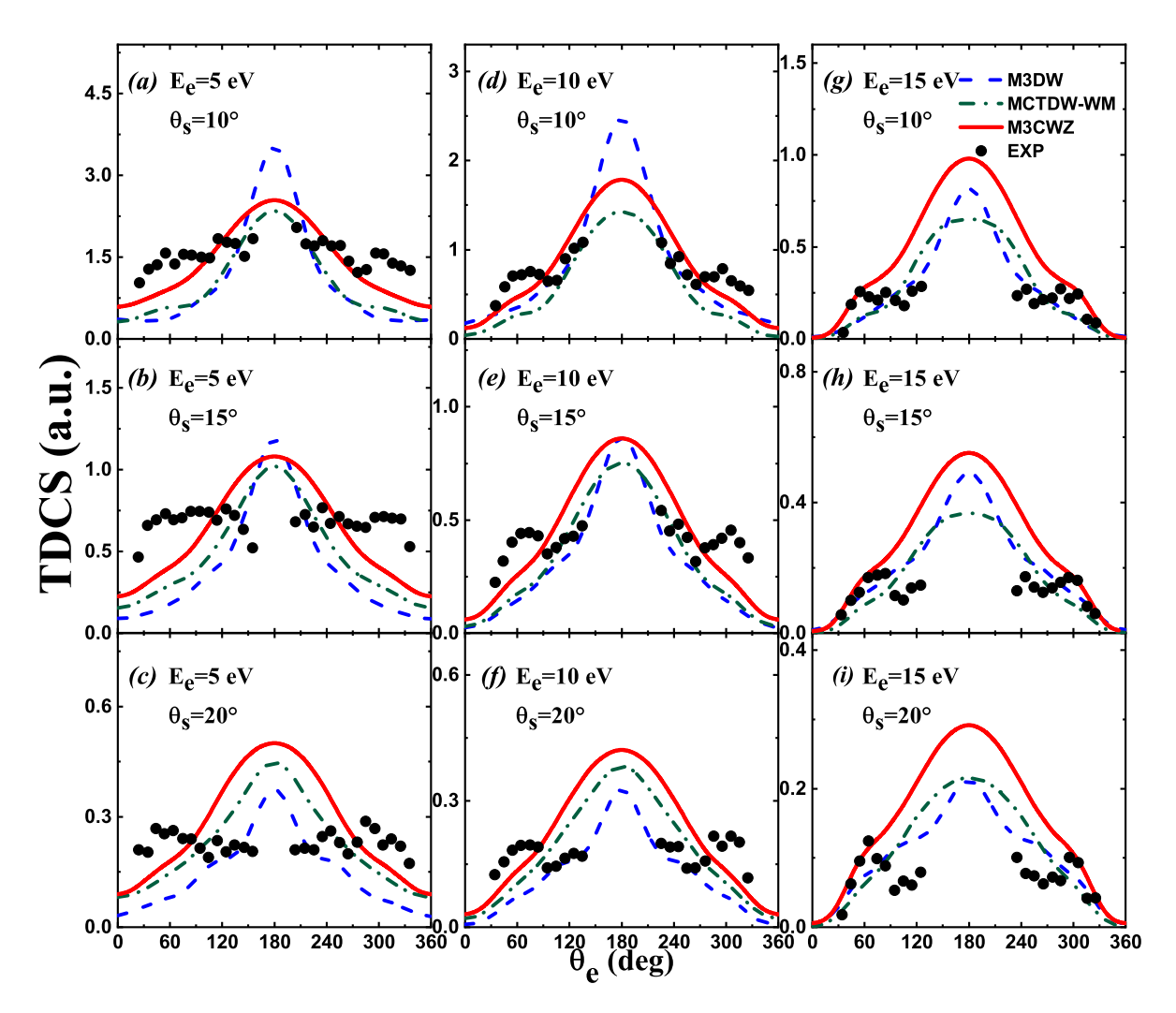


Figure 4.7: Same as Fig. 4.6 for the half perpendicular yz plane.

Figure 4.7 compares the TDCS in the half perpendicular yz plane. The first observation is that both the measured data and the theoretical results exhibit symmetry about  $\theta_s = 180^{\circ}$  (a feature that was absent in the case of argon for 3CWZ in [Fig. 3.8]). Unfortunately, the lack of experimental points around a  $180^{\circ}$  ejection angle does not allow us to firmly

confirm the presence of the clear and broad theoretical maximum; however, a hint of such a maximum can be perceived in Figs. 4.7d and 4.7e. Quantitatively, the M3CWZ results slightly overestimate those of the MCTDW-WM model in all nine cases. When compared with M3DW, the M3CWZ cross sections are rather close in most cases except for Figs. 4.7a and 4.7d although the M3DW model exhibits a sharper maximum in the region around  $\theta_s = 180^{\circ}$ . Overall, the experimental data are reasonably well reproduced by all three models, except at a 5 eV ejection energy [Figs. 4.7a–4.7c], where the theoretical angular distributions differ and substantially underestimate the experimental data for  $\theta_s \leq 100^{\circ}$  and  $\theta_s \geq 250^{\circ}$ .

Figure 4.8 shows the TDCS in the full perpendicular xy plane; here, the measured data cover the entire range of the azimuthal ejection angle  $\varphi_e$ . At a 5 eV ejection energy [Figs. 4.8a–4.8c], the data exhibit up to three maxima. Among the three theoretical models, the M3CWZ model appears to better reproduce both the shape and magnitude of the data, especially in the regions near  $\varphi_e = 0^\circ$  and  $\varphi_e = 360^\circ$ . At higher ejection energies,  $E_e = 10$  and 15 eV, the peak observed at  $\varphi_e = 180^\circ$  for 5 eV progressively disappears and is replaced by a plateau in the region between  $\varphi_e = 90^\circ$  and  $\varphi_e = 250^\circ$ . This evolution in the angular domain is better reproduced by the M3CWZ model and, to some extent, by the MCTDW-WM model, while the M3DW model still yields a clear peak around  $\varphi_e = 180^\circ$ . Outside this middle angular range, the M3CWZ and MCTDW-WM results are similar, but both significantly overestimate the measured data as well as the M3DW calculations.

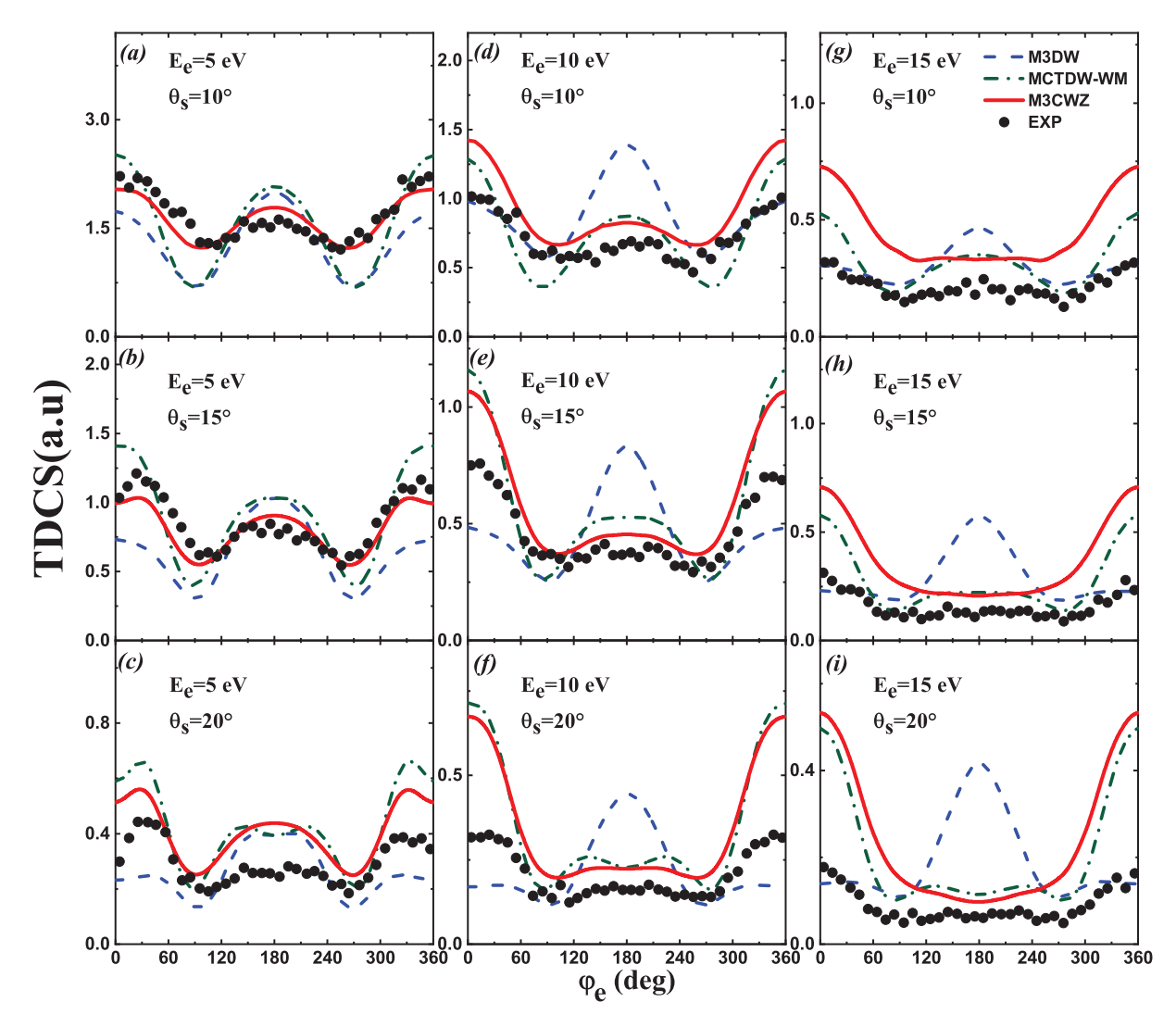


Figure 4.8: Same as Fig. 4.6 for the half perpendicular xy plane.

The theory–experiment comparison at  $65\ eV$  clearly shows that some TDCS features do not match, and no theoretical model achieves perfect agreement with the reported data in all configurations. Although simpler in its formulation and with a lower computational cost, our M3CWZ model globally performs as well as the more sophisticated approaches M3DW and MCTDW.

Now we would like to address a complementary issues concerning the proposed M3CWZ model. The incident, scattered and ejected electron wave functions are represented by Coulomb functions with variable charges and they vary from Z=8 to Z=0 when describing the incident electron wave function and to Z=1 for the outgoing electrons (as seen in Figure.4.2). Another option consists in using instead constant asymptotic charges (Z=0 and Z=1): the M3CWZ reduces then to the well known BBK model [31].

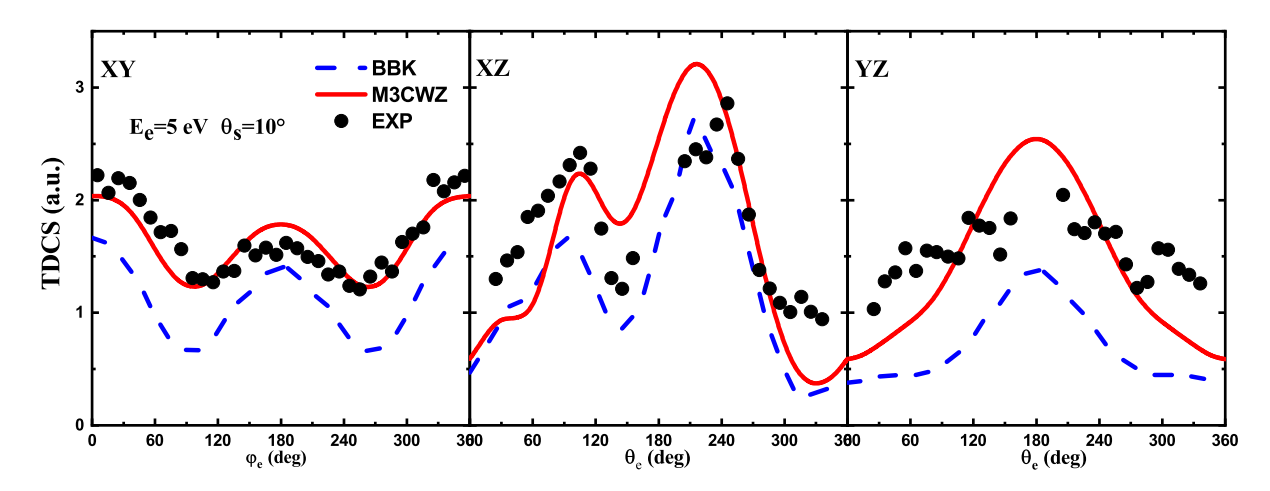


Figure 4.9: Absolute summed TDCS for the ionization of  $1b_1$  and  $3a_1$  orbitals of H2O as a function of the ejection angle at 65 eV impact energy. The projectile is scattered  $\theta_s = 10^{\circ}$  in coincidence with the ejected electron with  $E_e = 5$  eV. Left-hand column: in the full perpendicular (xy) plane; central column: in the scattering (xz) plane; right-hand column: in the half perpendicular (yz) plane. Theoretical results are red solid line (M3CWZ) and dashed blue line (BBK). The absolute experimental data are black circles taken from [15].

A question arises: would such asymptotic charges be sufficient to produce acceptable TDCS angular distributions? The answer is negative. To show the importance of taking into account the molecular distortion, we present in 4.9 a comparison, on absolute scale, at 65 eV impact energy for  $1b_1 + 3a_1$  orbitals [15] for  $E_e = 5$  eV and  $\theta_s = 10^\circ$  in the three orthogonal planes (xy, xz and yz planes). It appears that, in all cases, the M3CWZ reproduces quite well the experiments, while the BBK model underestimates both the M3CWZ results and the data. As already mentioned, such kinematics correspond to the dipolar regime for which it is known that the BBK manages to reproduce the shape but not the absolute magnitude. Outside this kinematical regime, the BBK model fails to reproduce the TDCS angular distribution, in particular in the recoil region as illustrated for the argon atom in [32]. On the other hand the variable charge scheme manages to describe quite well the TDCS shape. Whether for the atomic or the molecular case, the effectiveness of variable charges is, thus, even more visible when the residual ion plays a substantial role in the reaction.

## 4.6 Ongoing work: developing a hybrid approach

In an effort to overcome certain limitations of the M3CWZ, we investigated a modification that incorporates a distorted wave description for the slowest electron. This hybrid strategy is designed to preserve the computational efficiency of the original model while potentially yielding better agreement with experimental data at low-energy kinematics.

#### 4.6.1 Theory

The TDCS for this model is the same in Eq.(2.19) with the direct and exchange terms are written as

$$T_{dir} = \langle \phi_{CW}^{z(-)}(\mathbf{k}_s, \mathbf{r}_0) \phi_{DW}(\mathbf{k}_e, \mathbf{r}_1) | C(\alpha_{01}, \mathbf{k}_{se}, \mathbf{r}_{01}) | \frac{1}{r_{01}} - \frac{1}{r_0} | \phi_{CW}^{z(+)b}(\mathbf{k}_i, \mathbf{r}_0) \Phi_{nlm}(\mathbf{r}_1) \rangle$$
(4.7)

$$T_{exc} = \langle \phi_{CW}^{z(-)}(\mathbf{k}_s, \mathbf{r}_1) \phi_{DW}(\mathbf{k}_e, \mathbf{r}_0) | C(\alpha_{01}, \mathbf{k}_{es}, \mathbf{r}_{10}) | \frac{1}{r_{01}} - \frac{1}{r_0} | \phi_{CW}^{z(+)}(\mathbf{k}_i, \mathbf{r}_0) \Phi_{nlm}(\mathbf{r}_1) \rangle$$
(4.8)

where  $\phi_{DW}$  is the ejected electron's distorted wave, given by

$$\phi_{DW}(\mathbf{k}_e, \mathbf{r}_1) = \frac{4\pi}{(2\pi)^{3/2}} \sum_{\ell,m} i^{\ell} e^{i(\delta_{\ell} + \sigma_{\ell})} \frac{\chi_{\ell}(k_e, r_1)}{k_e r_1} Y_{\ell,m}^*(\hat{k}_e) Y_{\ell,m}(\hat{r}_1)$$
(4.9)

the normalization of  $\phi_{Dw}$ , and the phase shift calculations are detailed in [33]. Initially, this approach was tested for ionization of the inner  $2a_1$  orbital, where the M3CWZ model failed to reproduce the recoil peak illustrated in Figure 4.3. Maintaining the same kinematical conditions, Figure 4.10 displays the TDCS and compared with the normalized experimental data from [13].

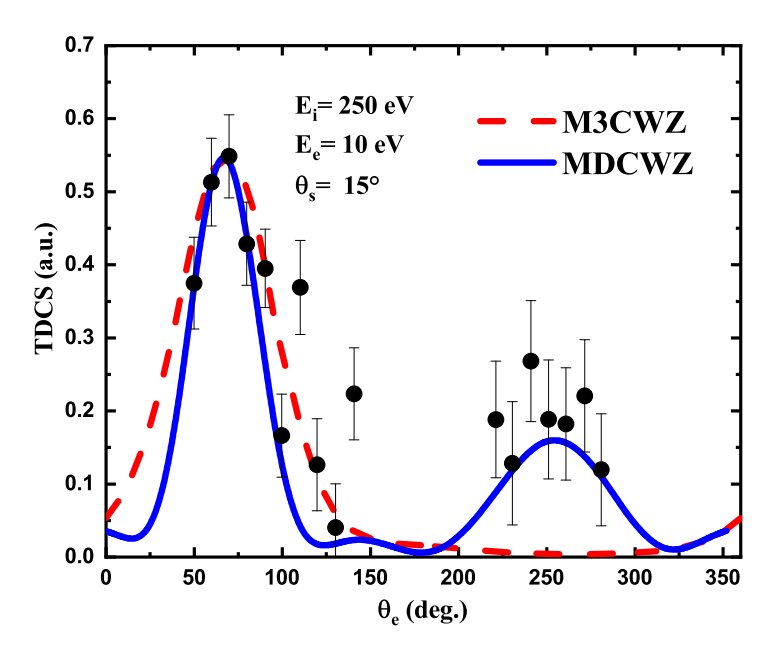


Figure 4.10: TDCS for electron-impact ionization of  $2a_1$  of  $H_2O$  at 250 eV impact energy. The projectile is scattered at an angle  $\theta_s = 15^{\circ}$  in coincidence with the ejected electron with energy  $E_e = 10 \ eV$  (except for  $3a_1$  orbital where  $E_e = 8 \ eV$ ). Theoretical results of M3CWZ model (red dashed line), and MDCWZ model (blue solid line) [29] are compared with the relative scale measurements [13] normalized to the M3CWZ calculation in the binary region.

Figure 4.10 shows that although both models exhibit good agreement in the binary peak region, the new approach manages to reproduce very well the angular distribution, with a very good agreement for the binary to recoil peak ratio, a significant difference from the M3CWZ model, which fails entirely to predict the data in that region.

Another test for the MDCWZ model was performed for low-energy kinematics ( $E_i = 65$  eV) in Figure 4.11, specifically the case where M3CWZ showed significant discrepancies with experimental data (see panel (i) in Figures 4.6, 4.7, and 4.8).

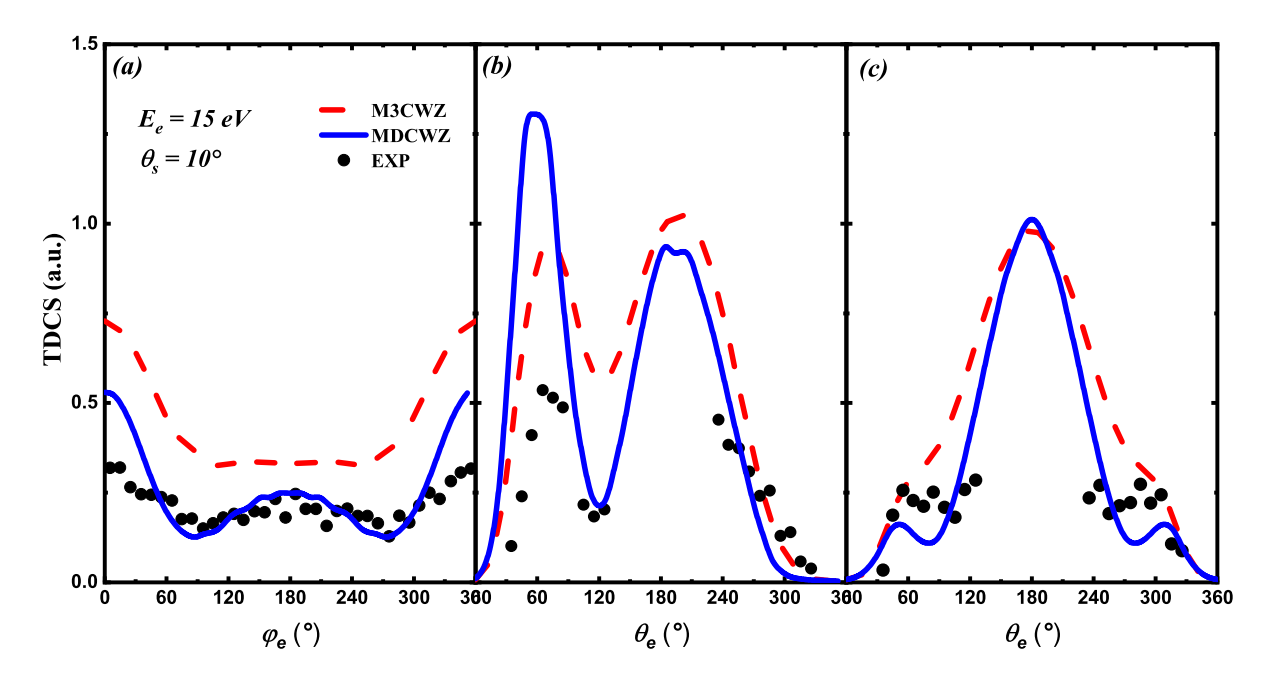


Figure 4.11: Absolute summed TDCS in the xy (a), yz (b), xz (c) planes for the ionization of  $1b_1$  and  $3a_1$  orbitals of  $H_2O$  as a function of the ejection angle at 65 eV impact energy. The projectile is scattered at angles  $\theta_s = 10^\circ$ , in coincidence with the ejected electron with energy  $E_s = 15$  eV. Theoretical results are red dashed line (M3CWZ) [29], blue solid line (MDCWZ). The absolute experimental data are black circles taken from Ref. [15].

Figure 4.11 clearly shows that both models yield rather similar shapes in the xz plane. However, the MDCWZ calculations overestimate the binary peak and show a deeper dip at the 120° emission angle, a feature not observed in the M3CWZ model in any case, as shown in Fig. 4.6. Similarly, for the yz plane, both models exhibit the same shape and magnitude without a noticeable difference. The situation is different for the xy plane: the observed peak at  $\phi_e = 180^\circ$  is completely missing in the M3CWZ calculations, appearing instead as a plateau. In contrast, the MDCWZ model shows very good agreement, specifically in the range  $\phi_e = 90^\circ$  to  $\phi_e = 260^\circ$ . Further tests are clearly required to validate this model.

## 4.7 Conclusion

To summarize this chapter, a model called M3CWZ has been used to investigate the ionization of the  $1b_1$  and  $3a_1$  orbitals of the water molecule at low impact energies. The model is based on a full Coulomb wave description with variable charges derived from the molecular target properties, and it accounts for both PCI and exchange effects. The proposed M3CWZ approach can be readily applied to any other molecule with a heavy center, provided that the variable charges are calculated from a spherically averaged potential associated with the relevant molecular orbital.

The TDCSs calculated using this model have been compared with recent experiments obtained using a COLTRIMS reaction microscope (C-REMI), which covers the full emission solid angle. The data are subsequently presented as cuts in three orthogonal planes providing a 3D image of the TDCS, thereby offering deeper insight into the ionization dynamics. Our results have also been compared with those from the M3DW and MCTDW (or MCTDW-WM) models, which currently represent the best available theories for molecular ionization. Initially, the model was tested at higher-energy kinematics, and then the TDCS was calculated at an 81 eV impact energy; in these kinematics the experimental data were inter-normalized across the measured scattering angles and ejected energies. Our calculations were found to correctly predict the experiments in most configurations, showing overall agreement with the M3DW and MCTDW models and in certain cases, even outperforming them. In a second step, at a 65 eV impact energy the situation is more challenging since the measured data are absolute. In this case, the MCTDW-WM model can be used only for a qualitative comparison of the TDCS shapes, so that the comparison is reduced to the M3CWZ and M3DW models. The results indicate a reasonably good agreement between our theory and the experimental data in both shape and magnitude; the M3CWZ and M3DW models are globally equivalent. This implies that, for the water molecule at least, Coulomb waves with appropriately chosen variable charges derived from a central potential are capable of reasonably describing the multicenter distortion effects of the molecular continuum. The main advantage of the M3CWZ approach is its low computational cost, as one data point can be obtained in a few hours rather than the several days required by the M3DW model.

Since a number of experimentally observed features are not described correctly by any of the available theoretical models, it is clear that more investigations are needed. New absolute scale measurements in other kinematical regimes could provide further stringent tests to challenge theoretical descriptions, and finally lead to a more complete understanding of the ionization dynamics in small molecules. Let us close this chapter by recalling that the study of water molecule continues to attract significant attention due to its radiobiological importance. In this context investigations involving clusters of water molecules instead of single water molecules offer a more realistic picture, in order to better estimate the damage in living tissue [34].

## **Bibliography**

- [1] K. Jung, D. Schubert, D. A. L. Paul, and H. Ehrhardt. J. Phys. B: At. Mol. Opt. Phys., 8:313, 1975.
- [2] L. Avaldi, R. Camilloni, E. Fainelli, and G. Stefani. J. Phys. B: At. Mol. Opt. Phys., 25:3551, 1992.
- [3] J. Yang and J. P. Doering. . Phys. Rev. A, 63:032717, 2001.
- [4] S. Rioual, G. Nguyen Vien, and A. Pochat. . Phys. Rev. A, 54:4968, 1996.
- [5] M. J. Hussey and A. J. Murray. J. Phys. B: At. Mol. Opt. Phys., 38:2965, 2005.
- [6] S. J. Cavanagh and B. Lohmann. J. Phys. B: At. Mol. Opt. Phys., 32:L261, 1999.
- [7] L. Avaldi, R. Camilloni, and G. Stefani. . Phys. Rev. A, 41:134, 1990.
- [8] L. G. Christophorou and J. K. Olthoff. J. Phys. Chem. Ref. Data, 29:267, 2000.
- [9] X. Ren, T. Pflüger, M. Weyland, W. Y. Baek, H. Rabus, J. Ullrich, and A. Dorn. . J. Chem. Phys., 142:174313, 2015.
- [10] E. Ali, X. Ren, A. Dorn, C. Ning, J. Colgan, and Don Madison. . Phys. Rev. A, 93:062705, 2016.
- [11] S. Jia, J. Zhou, X. Wang, X. Xue, X. Hao, Q. Zeng, Y. Zhao, Z. Xu, A. Dorn, and X. Ren. . Phys. Rev. A, 107:032819, 2023.
- [12] A. C. Guyton and J. E. Hall. *Textbook of Medical Physiology*. Elsevier Saunders, Philadelphia, 11th edition, 2006.
- [13] D. S. Milne-Brownlie, S. Cavanagh, B. Lohmann, C. Champion, P. A. Hervieux, and J. Hanssen. . *Phys. Rev. A*, **69**:032701, 2004.
- [14] X. Ren, S. Amami, K. Hossen, E. Ali, C. Ning, J. Colgan, D. Madison, and A. Dorn. Phys. Rev. A, 95:022701, 2017.
- [15] J. Zhou, E. Ali, M. Gong, S. Jia, Y. Li, Y. Wang, Z. Zhang, X. Xue, D. V. Fursa, I. Bray, X. Chen, D. Madison, A. Dorn, and X. Ren. . Phys. Rev. A, 104:012817, 2021.
- [16] E. Wang, X. Ren, W. Baek, H. Rabus, T. Pfeifer, and A. Dorn. Nature Communications, 11:2194, 2020.

- [17] D. D. Macdonald, G. R. Engelhardt, and A. Petrov. . Corros. Mater. Degrad., 3:3, 2022.
- [18] J. L. Fox, M. Benna, P. R Mahaffy, and B. M. Jakosky. . Geophys. Res. Lett., 42:21, 2022.
- [19] D. A. McQuarrie and J. D. Simon. *Physical Chemistry: A Molecular Approach*. University Science Books, Melville USA, 1st edition, 1997.
- [20] R. G. Mortimer. Physical Chemistry. Harcourt Academic Press, California USA, 3rd edition, 2008.
- [21] R. Moccia. J. Chem. Phys., 40:2164, 1964.
- [22] I. Kada. PhD thesis, University Ferhat Abbas Sétif 1, 2009.
- [23] R. Moccia. J. Chem. Phys., 40:2186, 1964.
- [24] M. R. H Rudge. . Rev. Mod. Phys., 40:564, 1968.
- [25] O. Zaidi, A. Mansouri, S. Houamer, A. Tamin, T. Khatir, and C. Dal Cappello. . Eur. Phys. J. D, 78:140, 2024.
- [26] K. Bechane, S. Houamer, T. Khatir, A. Tamin, and C. Dal Cappello. *Phys. Rev. A*, 109:012812, 2024.
- [27] M. Attia, S. Houamer, T. Khatir, K. Bechane, S. Houamer, and C. Dal Cappello. J. Phys. B: At. Mol. Opt. Phys., **56**:075201, 2023.
- [28] T. Khatir, S. Houamer, and C. Dal Cappello. *J. Phys. B: At. Mol. Opt. Phys*, **52**:245201, 2019.
- [29] A. Tamin, S. Houamer, T. Khatir, L. U. Ancarani, and C. Dal Cappello. J. Chem. Phys., 161:164305, 2024.
- [30] M. Gong, X. Li, S. B. Zhang, S. Niu, X. Ren, E. Wang, A. Dorn, and X. Chen. Phys. Rev. A, 98:042710, 2018.
- [31] M. Brauner, J. S. Briggs, and H. Klar. J. Phys. B: At. Mol. Opt. Phys., 22(14):2265–2287, 1989.
- [32] M. Attia, S. Houamer, T. Khatir, K. Bechane, S. Houamer, and C. Dal Cappello. J. Phys. B: At. Mol. Opt. Phys., 56:075201, 2023.

- [33] T. Khatir. PhD thesis, University Ferhat Abbas Sétif 1, 2021.
- [34] Z. Alfaytarouni, P. A. Hervieux, C. Dal Cappello, G. Noel, and Z. El Bitar. *Nucl. Instrum. Methods Phys. Res.*, Sect. B, **549**:165279, 2024.

## Chapter 5

# Electron-Impact Ionization of the Methane Molecule

## 5.1 Introduction

In the previous chapter, the M3CWZ model was successfully applied to the ionization of water molecules, demonstrating a satisfactory agreement with experimental data. Building on these findings, it is natural to investigate other molecular targets and different kinematics. This chapter focuses on electron-impact ionization of methane (CH<sub>4</sub>), one of the simplest yet most significant hydrocarbons. Beyond its fundamental scientific interest, methane has attracted considerable attention in recent years due to its strong influence on global warming. Not only is methane a potent greenhouse gas surpassing carbon dioxide in short-term warming potential but climate change itself is causing larger releases of previously trapped CH<sub>4</sub> into the atmosphere. Furthermore, methane is of practical interest in several other fields, such as astrophysics, radiobiology, and plasma physics [1]. This dual effect underscores methane's growing importance as a research target. Another reason for selecting methane is the abundance of studies and available data (see [2,3] and references therein).

Accordingly, we calculate the triple differential cross section for ionizing the  $1t_2$  and  $2a_1$  orbitals of methane under various kinematic conditions, ranging from intermediate [4, 5] to lower impact energies [6].

The theoretical background of the model was covered in detail in the previous chapter; therefore, this chapter adopts a simpler layout. We provide a brief description of the methane molecule and the employed wave function before moving directly to the results and discussion.

## 5.2 Theoretical description of the methane molecule

Within the MO-LCAO framework, molecular orbitals of methane are constructed as linear combinations of carbon and hydrogen atomic orbitals, accounting for the tetrahedral geometry of CH<sub>4</sub>. Following this theory, the ten electrons in methane's ground state (six from carbon, four from hydrogen) occupy a set of bonding molecular orbitals often labeled as  $(1a_1)^2$ ,  $(2a_1)^2$ , and  $(1t_2)^6$ . Here,  $1a_1$  and  $2a_1$  largely reflect the symmetric combinations of C(2s) and H(1s), while  $1t_2$  captures the degenerate bonding interactions involving C(2p) orbitals. The highest occupied molecular orbital (HOMO) is the  $1t_2$  set

$$1a_1^2 2a_1^2 1t_2^6. (5.1)$$

The orbital  $1t_2^6$  is degenerate and written as:

$$1t_2^6 = 1t_{2x}^2 1t_{2y}^2 1t_{2z}^2 (5.2)$$

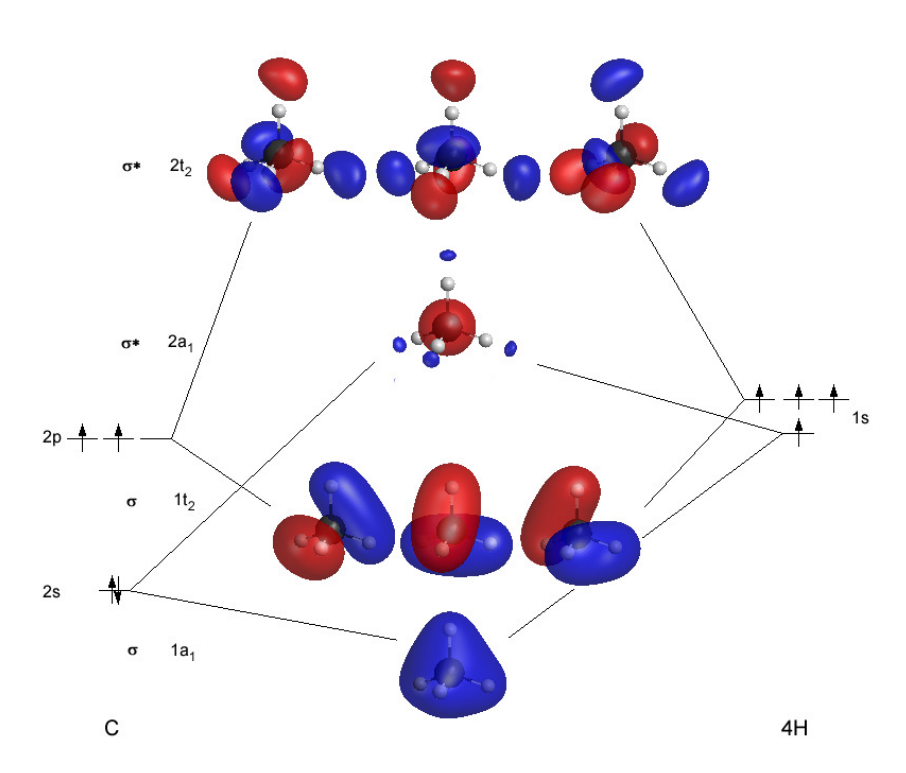


**Figure 5.1:** Molecular orbital diagram of methane  $CH_4$  (Adapted from ChiralJon , licensed under CC BY 2.0) .

#### 5.2.1 The wave function

Similarly to water molecule, we use Moccia monocentric functions (see Chapter 1 section 1.7.2.1). For the  $CH_4$  molecular orbitals, their parameters  $(n_{ik}, l_{ik}, m_{ik}, \xi_{ik}, a_{ik})$  along

with the ionization energies are provided in table 5.1

n	l	m	ξ	$1a_1$	$2a_1$	$1t_{2x}$	$1t_{2y}$	$1t_{2z}$
1	0	0	9.500	0.00877	0.05838			
1	0	0	5.500	-0.21248	0.93837			
2	0	0	1.500	0.98204	0.07150			
4	0	0	2.000	0.05076	-0.03310			
4	0	0	2.000	-0.01799	-0.03118			
7	3	-2	2.900	0.14254	0.00039			
2	1	1	1.373			1.25996		
3	1	1	2.950			-0.05760		
4	1	1	2.950			-0.26740		
7	3	1	2.900			0.05331		
7	3	-3	2.900			-0.06875		
4	2	1	2.400			-0.06694		
4	2	-1	1.900			0.32784		
2	1	-1	1.373				1.25996	
3	1	-1	2.950				-0.05760	
4	1	-1	2.950				-0.26740	
7	3	-1	2.900				0.05331	
7	3	-3	2.900				-0.06875	
4	2	1	2.400				-0.06694	
4	2	-1	1.900				0.32784	
2	1	0	1.373					1.25998
3	1	0	2.950					-0.05762
4	1	0	2.950					-0.26738
7	3	0	2.900					-0.08695
4	2	-2	2.400					-0.06691
4	2	-2	1.900					0.32775
Ior	Ionization energy (a.u.)			11.1949	0.9204	0.5042	0.5042	0.5042

**Table 5.1:** Parameters of Moccia's wave functions and ionization energies for the molecular orbitals of  $CH_4$  [7].

#### 5.2.2 Variable charge

In the case of ionizing the  $1t_2$  molecular orbital, the average potential can be written as

$$U(r_1) = \frac{1}{4\pi} \int \left[ -\frac{4}{R} - \frac{6}{r_1} + 5 \int \frac{|\phi_{1t_2}|^2}{|\mathbf{r} - \mathbf{r}_1|} d\mathbf{r} + 2 \int \frac{|\phi_{2a_1}|^2}{|\mathbf{r} - \mathbf{r}_1|} d\mathbf{r} + 2 \int \frac{|\phi_{1a_1}|^2}{|\mathbf{r} - \mathbf{r}_1|} d\mathbf{r} \right] d\Omega_e = -\frac{Z(r_1)}{r_1}, \qquad (5.3)$$

$$U(r_1) = \frac{1}{4\pi} \int \left[ -\frac{4}{r_1} - \frac{6}{R} + 5 \int \frac{|\phi_{1t_2}|^2}{|\mathbf{r} - \mathbf{r}_1|} d\mathbf{r} + 2 \int \frac{|\phi_{2a_1}|^2}{|\mathbf{r} - \mathbf{r}_1|} d\mathbf{r} + 2 \int \frac{|\phi_{1a_1}|^2}{|\mathbf{r} - \mathbf{r}_1|} d\mathbf{r} \right] d\Omega_e = -\frac{Z(r_1)}{r_1}, \qquad (5.4)$$

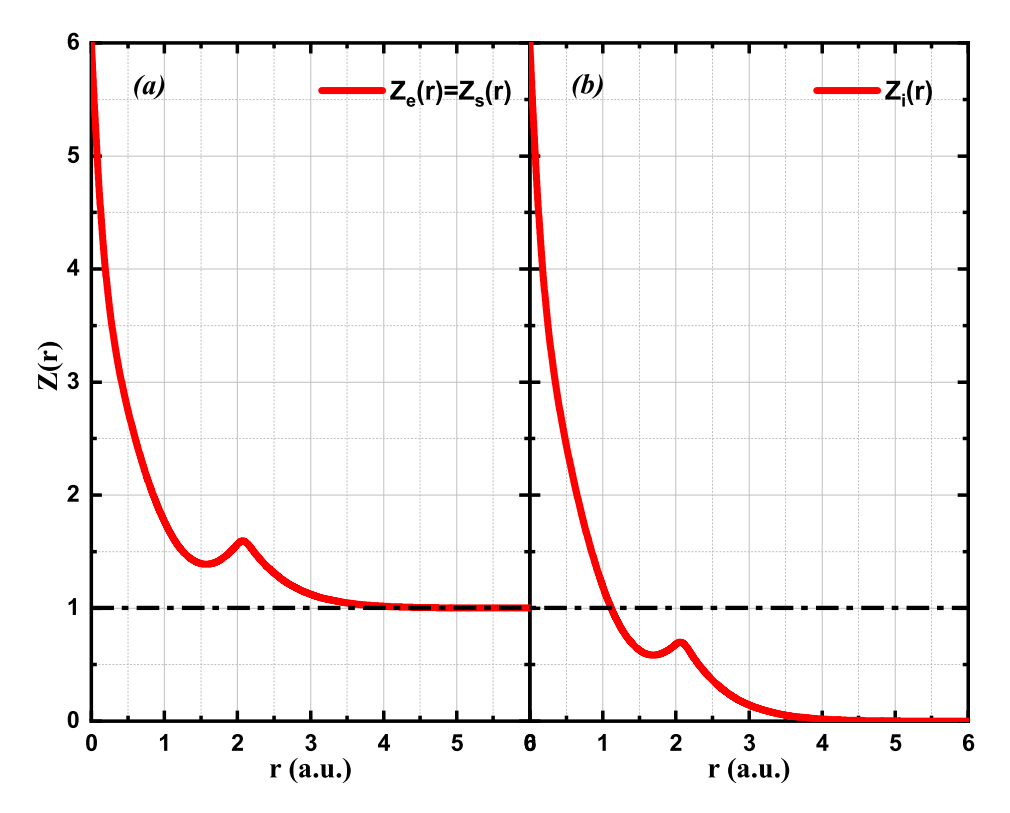


**Figure 5.2:** Variable charge Z(r) felt by the outgoing electrons (a) and the incident electron (b) during the ionization process for the  $1t_2$  molecular orbital of  $CH_4$ .

Figure 5.2 presents the variable charges for the ionization of the  $1t_2$  orbital of CH<sub>4</sub>. It shows a trend similar to that observed for water, where the charge decreases from a maximum value of Z=6 at r=0 to Z=1 for the outgoing electrons and Z=0 for the incident electron. Additionally, near r=R=2.08 au, a kink corresponding to the C-H distance is observed (similarly to the water molecule as presented in Chapter 4, Section 4.4).

## 5.3 Results and discussions

For the intermediate energy range the theoretical study is performed in two energy regimes, several sets of experimental data were used for comparison. We first calculated the TDCS for the ionization of the  $1t_2$  orbital under the kinematic conditions presented by Lahman Bennani et al. [4]. In this experiment, the geometry is coplanar asymmetric: the projectile is scattered with an energy of 500 eV at a scattering angle of  $\theta_s = 6^{\circ}$ , while the ejected electron energies are  $12 \ eV$ ,  $37 \ eV$ , and  $74 \ eV$ . Under these kinematical and geometrical conditions, the TDCS exhibits two distinct peaks: a binary peak and a recoil peak.

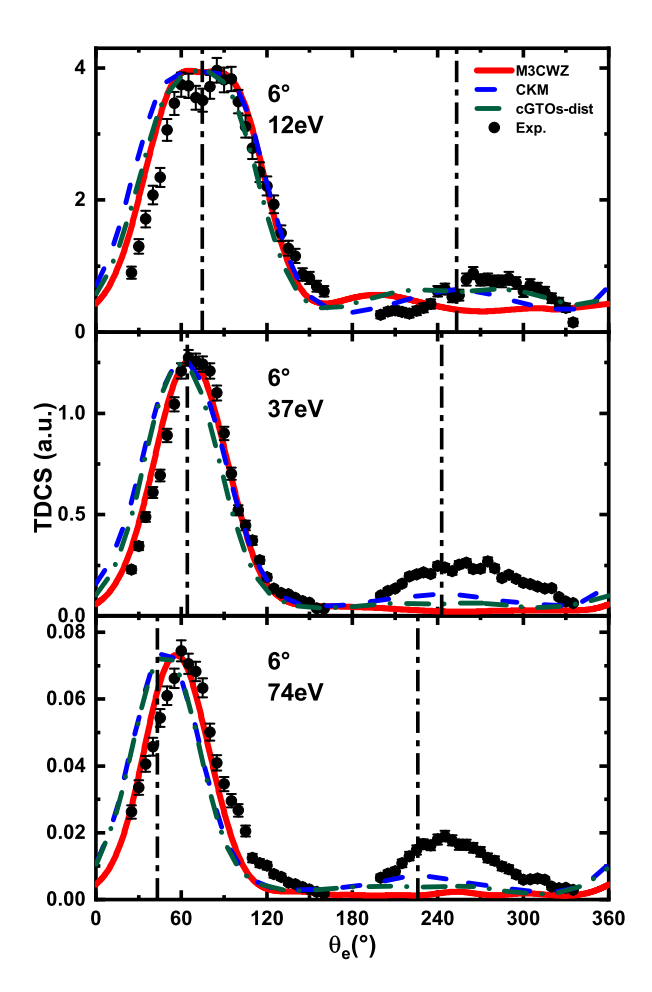


Figure 5.3: TDCS for the ionization of the  $1t_2$  orbital of  $CH_4$  as a function of the ejection angle at 500 eV scattering energy, with scattering angle of 6°. The ejected electron energy are 12 eV, 37 eV, and 74 eV. Theoretical results are represented by the red solid line (M3CWZ), green dot-dashed line for (cGTOs-dist) [2], blue dashed line for (CKM) [8], and experimental data are shown as black circles [4]. The dot-dashed vertical lines indicates the direction of the momentum transfer  $\mathbf{K}$  and its opposite direction  $-\mathbf{K}$ .

The M3CWZ results are presented in Figure 5.3 and compared with the experimental data from [4], and two other theoretical approaches, namely the Complex Gaussian-Type Orbitals with a distorded wave (cGTOs-dist) [2], and the Complex Kohn Method (CKM) [8]. All results are normalized to the binary peak of each panel.

Figure 5.3 shows that all three theoretical models accurately reproduce the binary peak across the examined ejected electron energies and overall follow a similar trend. However, none of the models capture the recoil peak, except for the lowest ejected electron energy  $(12\ eV)$ , as shown in the first panel), where the cGTOs and CKM models recover the recoil peak, which is underestimated in the M3CWZ results.

Another test was conducted under a different kinematical setup, where the incident elec-

tron energy was 250 eV [5], in this part only the outer  $1t_2$  orbital is investigated. The scattering angles were fixed at  $20^{\circ}$ ,  $22.5^{\circ}$ ,  $25^{\circ}$ ,  $27.5^{\circ}$ , and  $30^{\circ}$ , with the ejected electron energy set to either 50 eV or 30 eV. Figure 5.4 shows the M3CWZ results, which are compared with recent experimental data from [5] as well as with the GSF and M3DW results from [9]. Note that the focus is on the binary region only (i.e.,  $\theta_e = 0^{\circ}-140^{\circ}$ ), and the data have been normalized to the M3CWZ curve corresponding to  $\theta_s = 20^{\circ}$ .

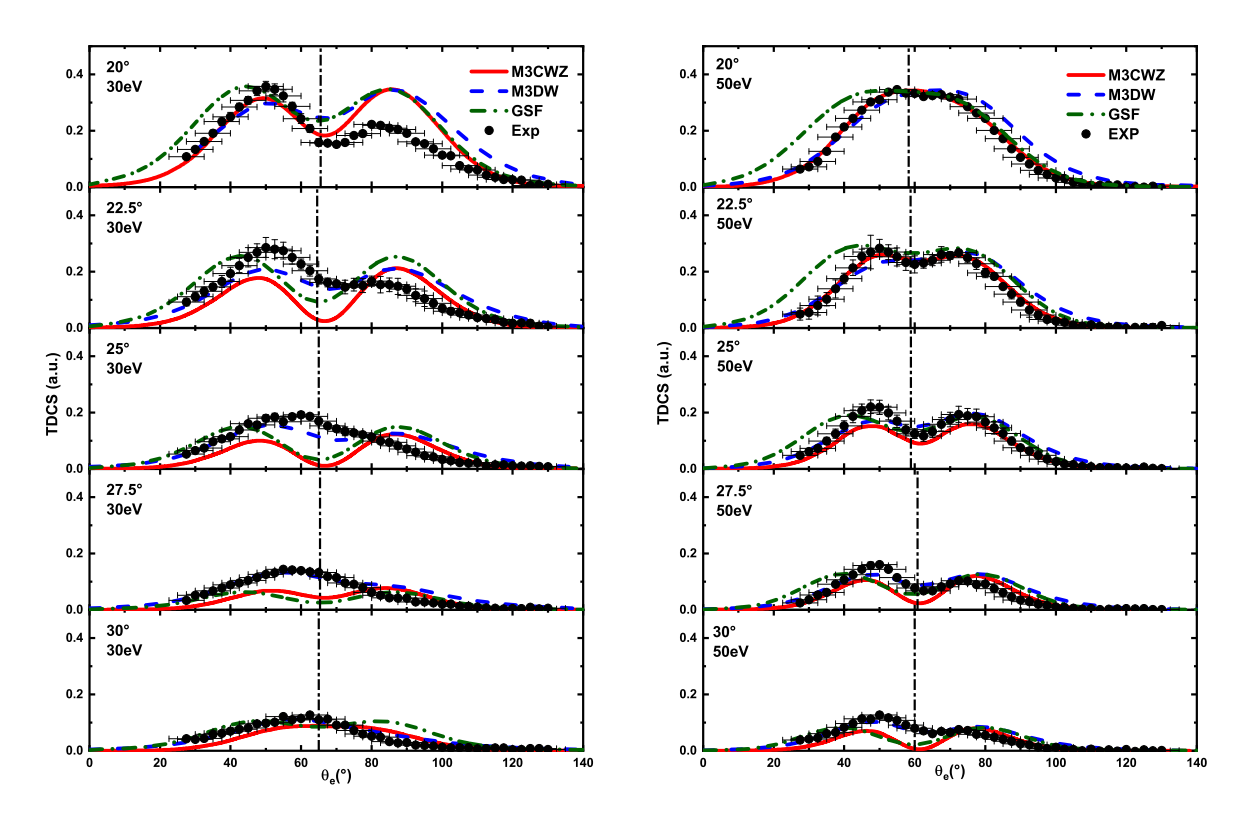


Figure 5.4: TDCS for the ionization of the  $1t_2$  orbital of CH<sub>4</sub> as a function of the ejection angle at 250~eV impact energy. The scattering angles are  $20^{\circ}$ ,  $22.5^{\circ}$ ,  $25^{\circ}$ ,  $27.5^{\circ}$ , and  $30^{\circ}$ . The ejected electron energy is 30~eV for the left panel and 50~eV for the right panel. Theoretical results are represented by the red solid line (M3CWZ), blue dashed line (M3DW) [9], and green dash-dot line (GSF) [9], while experimental data are shown as black circles from [5]. The dot-dashed vertical line indicates the direction of the momentum transfer K

The first notable feature in the TDCS shown in Fig. 5.4 is the splitting of the binary peak into a double-peak structure, which gradually vanishes as the scattering angle increases a behavior observed both experimentally and theoretically. However, at the lower ejection energy of  $30 \ eV$ , the experimental data indicate that this double-peak structure begins to fade starting from a scattering angle of  $22.5^{\circ}$ , whereas all three theoretical models maintain the double peak until  $27.5^{\circ}$ , only fully disappearing at  $30^{\circ}$ . Conversely, at the higher ejection energy of  $50 \ eV$ , both experimental and theoretical results exhibit similar behavior. Overall, the M3CWZ results compare favorably both in shape and the

relative magnitude with the experimental data and align closely with the predictions of the M3DW and GSF models. However, the M3DW model shows slightly better agreement with experimental results, particularly at higher scattering angles.

The final test investigates ionization at even lower-energy kinematics, namely 54.4 eV incident energy, which pose significant challenges for theoretical modeling.

Figure 5.5 presents TDCS for the electron impact ionization of the  $1t_2$  orbital of methane at an incident energy of  $54.4 \, eV$ , with scattered and ejected electron energies fixed at  $30 \, eV$  and  $10 \, eV$ , respectively, for scattering angles  $(\theta_s)$  of  $20^\circ$ ,  $25^\circ$ ,  $40^\circ$ , and  $55^\circ$ . Here, each theoretical calculation and the experimental data set have been independently normalized to unity at the maximum intensity of their respective binary peaks. The performance of our proposed M3CWZ model is evaluated against experimental data [10] and compared with theoretical results obtained using the Molecular 3-Body Distorted Wave (M3DW) model employing both Proper Averaging (PA) [6] and Orientation Averaged Molecular Orbital (OAMO) [10] approaches.

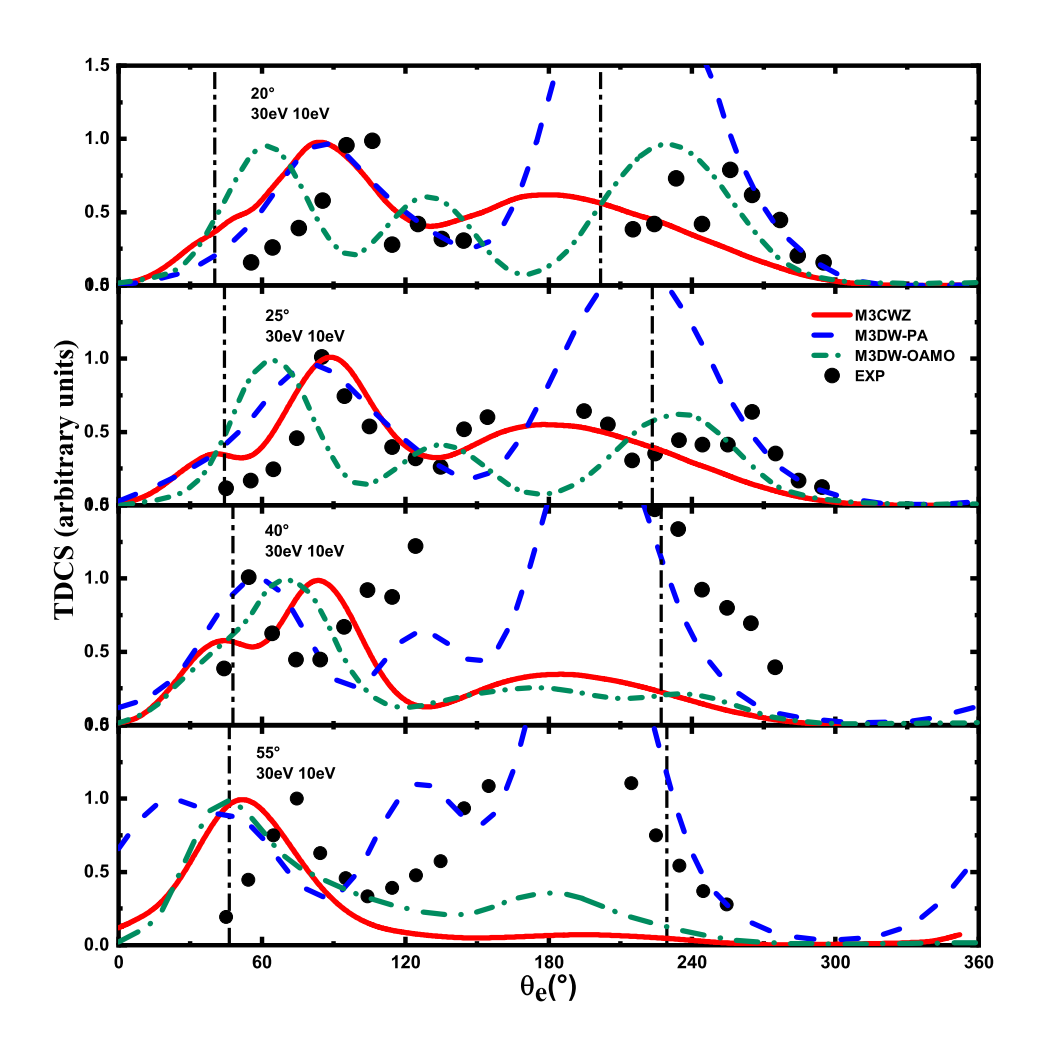
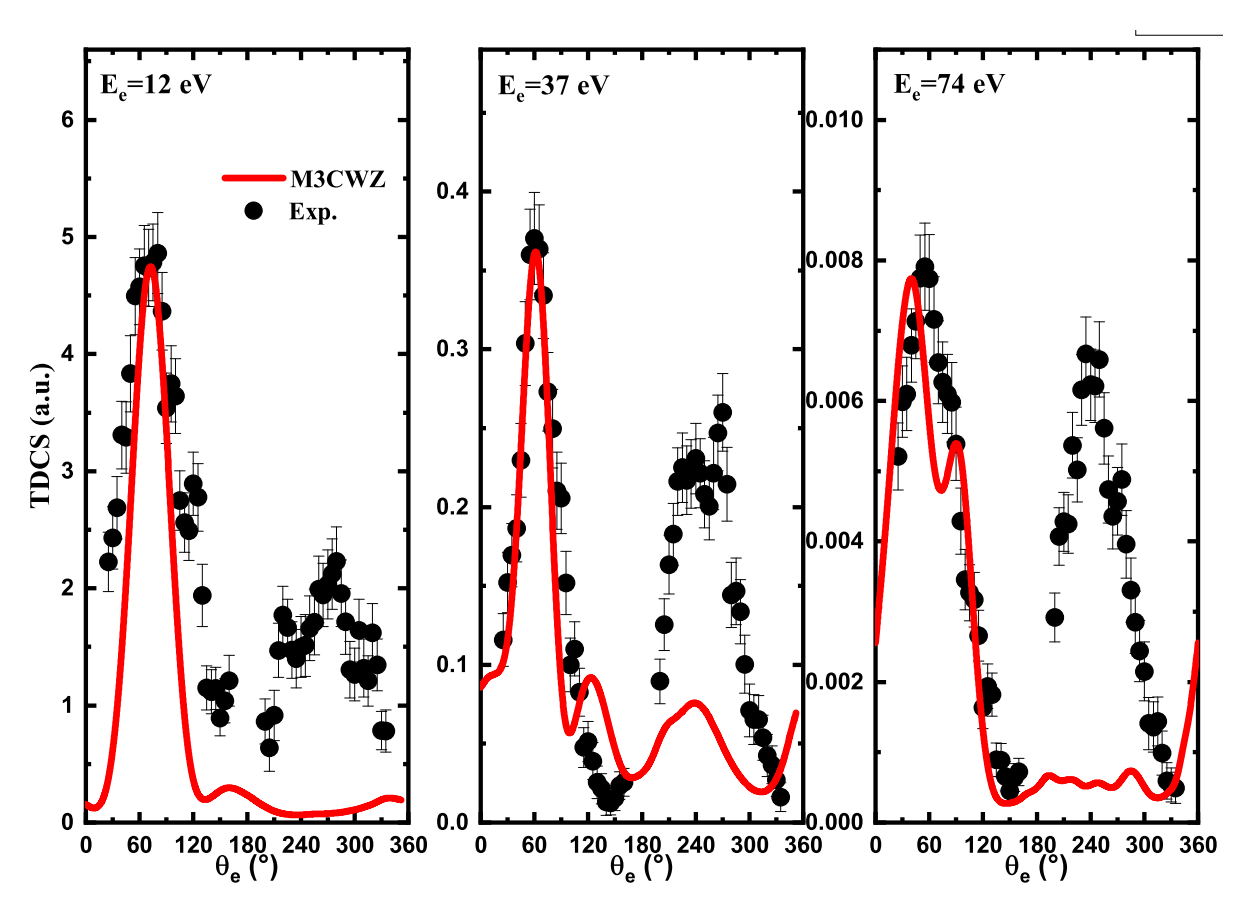


Figure 5.5: TDCS for the ionization of the  $1t_2$  orbital of  $CH_4$  as a function of the ejection angle at 54.4 eV impact energy, with scattering angles of  $20^{\circ}$ ,  $25^{\circ}$ ,  $40^{\circ}$ , and  $55^{\circ}$ . The scattered and ejected electron energies are  $30 \ eV$  and  $10 \ eV$ , respectively. Theoretical results are red solid line (M3CWZ), blue dashed line (M3DW-PA) [6], and green dash-dot line (M3DW-OAMO) [10], while experimental data are shown as black circles [10].

Across all scattering angles, the experimental TDCS exhibits the characteristic two peak structure (binary and recoil), which is qualitatively reproduced by all models. Regarding the binary peak, the M3CWZ model shows good agreement with the experimental peak position at lower scattering angles (20° and 25°). Under these conditions, both the M3CWZ and M3DW-PA models follow similar trends and demonstrate reasonable agreement with the experiment. In contrast, the OAMO approach fails to adequately describe the binary peak in these low-angle cases illustrating the limitation of preforming an orbital angular average versus a proper TDCS average. At higher scattering angles (40° and 55°), the discrepancy between the predicted and experimental binary peak positions becomes more pronounced, and none of the three models accurately capture the experimental peak location. In the recoil region, the model performance is more varied. The

M3CWZ model reproduces a recoil peak at low scattering angles; however, as the scattering angle increases, the recoil peak gradually diminishes, and it is completely absent at 55°. This deficiency is also seen in the OAMO approach. In contrast, the M3DW-PA model consistently reproduces the recoil peak across all scattering angles; however, while the peak's position is reasonably well reproduced, its relative magnitude is consistently and significantly overestimated when compared to the experimental data. Overall, while M3DW-PA provides the most consistent description across all angles, particularly for the recoil peak, none of the models produces a satisfactory agreement with the experimental TDCS. This clearly calls for further theoretical refinement.

Now we would like to address a brief study of the inner  $2a_1$  orbital of  $CH_4$ , we consider the same kinematic conditions discussed in Figure.5.3, and compare with the experimental data presented in [4].



**Figure 5.6:** TDCS for the ionization of the  $2a_1$  orbital of  $CH_4$  as a function of the ejection angle at 500 eV scattering energy, with scattering angle of 6°. The ejected electron energy are 12 eV, 37 eV, and 74 eV respectively. Theoretical results are represented by the red solid line (M3CWZ), and experimental data are shown as black circles [4].

Figure 5.6 shows that the M3CWZ model reproduces the binary peak shape and position across the examined ejected electron energies and overall follows a similar trend, except

at the energy of 74 eV. However, the model does not capture the recoil peak at any of these energies. This discrepancy, which was previously observed for the inner  $2a_1$  orbital of the water molecule (Figure 4.3), confirms the limitation of the M3CWZ model for inner orbitals.

### 5.4 Conclusion

This chapter investigated the electron-impact ionization of the  $1t_2$  orbital of methane  $CH_4$  using our M3CWZ model, comparing theoretical predictions against experimental data and other computational approaches (cGTOs-dist, CKM, GSF, M3DW-PA, M3DW-OAMO) across intermediate and low impact energies. At intermediate energies (500 eV and 250 eV), the M3CWZ model successfully reproduced the main binary peak features observed experimentally. Notably, it captured the characteristic splitting of the binary peak, attributed to the p-type nature of the  $1t_2$  orbital. The model showed favorable comparison in shape and relative magnitude with GSF and M3DW results in the binary region. However, M3CWZ generally underestimates or fails to capture the recoil peak at these energies, similarly to some other models. At the lower impact energy of 54.4 eV, a more challenging regime, the M3CWZ model qualitatively reproduced the characteristic two peak (binary and recoil) structure. It provided good agreement with the experimental binary peak position at lower scattering angles, performing comparably to the M3DW-PA model. However, agreement deteriorated at higher scattering angles, where none of the models accurately matched the experimental peak location. In the recoil region, M3CWZ captured the peak at lower angles but failed for higher scattering angles, a limitation shared with the M3DW-OAMO approach. Overall, while the M3CWZ model demonstrates its capability in capturing key qualitative features of methane ionization, particularly the binary peak structure and its splitting, the comparisons highlight limitations in accurately describing the recoil region across all kinematics, especially at lower energies. The results underscore the complexities of modeling electron-impact ionization for molecular targets like methane. Further theoretical investigations are needed, in particular to explain the large recoil peaks at low impact energy.

## **Bibliography**

- [1] D. Mahato, L. Sharma, A. D. Stauffer, and R. Srivastava. *Eur. Phys. J. D*, **73**:189, 2019.
- [2] A. Ammar, A. Leclerc, and L. U. Ancarani. Phys. Rev. A, 109:052810, 2024.
- [3] C. M. Granados Castro, L. U. Ancarani, G. Gasaneo, and D. M. Mitnik. *J. Phys.: Conf. Ser.*, **635**:112073, 2015.
- [4] A. Lahmam Bennani, A. Naja, E. S. Casagrande, N. Okumus, C. Dal Cappello, I. Charpentier, and S. Houamer. J. Phys. B: At. Mol. Opt. Phys., 42:165201, 2009.
- [5] N. Işık, M. Doğan, and S. Bahçeli. J. Phys. B: At. Mol. Opt. Phys., 49:065203, 2016.
- [6] H. Chaluvadi, C. G. Ning, and D. H. Madison. Phys. Rev. A, 89:062712, 2014.
- [7] R. Moccia. J. Chem. Phys., textbf40:2186, 1964.
- [8] C. Y. Lin, C. W. McCurdy, and T. N. Rescigno. *Phys. Rev. A*, textbf89:052718, 2014.
- [9] E. Ali, C. Granados, A. Sakaamini, M. Harvey, L. U. Ancarani, A. J. Murray, M. Dogan, C. J. Ning, J. Colgan, and D. H. Madison. J. Chem. Phys., textbf150:194302, 2019.
- [10] S. Xu and H. Chaluvadi, X. Ren, T. Pflüger, A. Senftleben, C. G. Ning, S. Yan, P. Zhang, J. Yang, X. Ma, J. Ullrich, D. H. Madison, and A. Dorn. J. Chem. Phys., 14:137, 2012.

## Conclusion

This thesis presents a comprehensive theoretical investigation into the dynamics of electron-impact single ionization ((e,2e) processes) for both atomic and molecular targets across various kinematic regimes. The central objective was to develop and rigorously evaluate theoretical models capable of accurately describing the complex three-body interactions, while also considering computational feasibility. Our study provides an in-depth analysis of the mechanisms involved in electron-impact ionization, highlighting both the theoretical advancements and the ongoing challenges in modeling these intricate phenomena. In particular, the triple differential cross section (TDCS) serves as a critical tool for the detailed description of ionization processes, as it is derived from scattering amplitudes that capture the transition between the initial and final states of the collision. This measurement is essential for exploring both the reaction dynamics and the structural properties of the target. The first part of our research was devoted to the study of ionization by electron impact on atomic and molecular targets in their ground state, a subject of considerable importance in various scientific fields, notably for its strategic applications in studying living matter.

The main focus of our research was the study of molecular target ionization specifically, the water molecule. However, to develop a theoretical model that can be reliably applied to molecular systems, it was necessary first to refine an approach that works well for atomic targets. As such, our initial efforts focused on improving the 3CWZ model for atoms before generalizing it to more complex molecular targets. The efficacy of the 3CWZ and M3CWZ models was systematically evaluated through the calculation of the TDCS. Extensive comparisons were performed against available experimental data for noble gas atoms (neon and argon) as well as key molecular targets (water and methane). These comparisons spanned a range of incident energies from intermediate to low impact energies and diverse kinematic conditions, including both asymmetric coplanar and non-coplanar geometries (scattering, half-perpendicular, and full-perpendicular planes). Furthermore, the performance of the proposed models was benchmarked against predictions from other prominent theoretical approaches, such as the Distorted Wave Born

Approximation (DWBA), the Three-Body Distorted Wave (3DW), the Molecular 3-Body Distorted Wave (M3DW), the Multicenter Three-Distorted-Wave (MCTDW) approach, and the Generalized Sturmian Function (GSF) method.

In Chapter 1, we reviewed the fundamental principles of scattering theory, differential cross sections, and various theoretical frameworks including 3DW, and M3DW. This chapter set the stage by establishing the key concepts and mathematical tools required to analyze collision dynamics.

Chapter 2 delved into the core theoretical development underpinning this work. It traced the evolution of models incorporating variable effective charges, starting from simpler asymptotic descriptions (1CW, BBK) and progressing through intermediate refinements (BBK1CWZ, BBK2CWZ), and revisiting the Three Coulomb Waves with a Variable Charge (3CWZ) model, which had been developed in earlier work. We detailed the model's derivation and highlighted its ability to incorporate variable charge effects in the description of the incident, scattered, and ejected electrons. The primary theoretical contribution of this thesis, the Molecular Three Coulomb Waves with Variable Charge (M3CWZ) model, was formally presented. The methodology for calculating the variable charges based on Hartree potentials and the analytical treatment of molecular orientation averaging within the M3CWZ framework were detailed, highlighting the computational advantages inherent in this approach compared to other treatments.

In Chapter 3, the model was applied to atomic targets namely neon and argon. Extensive experimental data were used to benchmark our calculations, allowing us to assess the model's performance across various kinematic regimes. Our analysis revealed that while the 3CWZ model generally reproduces the binary peak accurately, discrepancies in the recoil peak remain, particularly at higher scattering angles. Comparative studies with other theoretical approaches underscored both the strengths and limitations of the model. Chapters 4 and 5 represent the core of this research, focusing on molecular targets. Chapter 4 presented the major original contribution of this research: the application of the newly developed M3CWZ model to the electron-impact ionization of the water molecule  $H_2O$ . Given the paramount importance of water in biological systems and radiation physics, this served as a critical test case. The M3CWZ model was employed to calculate TDCS for the outer valence orbitals ( $1b_1$  and  $3a_1$ ), comparing results extensively with recent experimental data obtained via COLTRIMS reaction microscopy at low impact energies (81 eV and 65 eV) across the three orthogonal planes (scattering, half-perpendicular, and full-perpendicular). The M3CWZ results were benchmarked against two of the most powerful, but computationally intensive, molecular theories (M3DW and MCTDW-WM). The M3CWZ model demonstrated a remarkable ability to reproduce experimental data both in shape and magnitude across most kinematic conditions studied. Its performance

was found to be overall comparable and in some cases even surpassing the M3DW model, which is particularly impressive given M3CWZ's simplified, single-center treatment of the molecular potential and its significantly reduced computational cost (hours vs. days per data point). This chapter strongly validated the M3CWZ approach as a viable and efficient tool for investigating ionization dynamics in molecules. Chapter 5 further extended the application of the M3CWZ model to another fundamental molecule, methane  $(CH_4)$ . TDCS calculations for the  $1t_2$  orbital were performed for intermediate and low impact energies and compared with available experimental data and theoretical results from GSF, M3DW (PA and OAMO variants), and other models. This investigation confirmed the model's ability to capture characteristic TDCS features for the outer orbital. While generally showing good agreement for outer shells, particularly at intermediate energies, comparisons at the lowest energy (54.4 eV) for methane's outer orbital also revealed challenges where discrepancies and limitations emerged. However, a significant limitation was identified as the M3CWZ model failed to reproduce the data for the inner orbitals of both  $H_2O$  and  $CH_4$ , specifically for the recoil region. While the qualitative agreement with experimental data for outer orbitals was strong, achieving precise quantitative correspondence under certain conditions remained challenging, particularly at very low impact or ejection energies and in the case of the methane molecule. Discrepancies in peak magnitudes, positions, and the exact reproduction of subtle structural features, combined with the failure for inner orbitals, indicate that further refinement is needed in the variable charge approximation. Overall, while the 3CWZ/M3CWZ model shows considerable promise as a tool for modeling (e, 2e) processes, our findings also highlight areas for further theoretical refinement. To address these limitations, a new model is under development which improves the theory by representing the ejected electron as a true distorted wave. Preliminary results show this enhanced model was able to reproduce the data for the inner orbitals; however, further testing is needed to fully validate it.

# Appendix A

# The scattering amplitude in BBK model

We consider the matrix element  $T_{if}$ , which can be expressed as

$$T_{if} = \langle \Psi_f | V | \Psi_i \rangle \tag{A.1}$$

where  $V = -\frac{1}{r_0} + \frac{1}{r_{01}}$  is the Coulomb potential between the incident electron and the active electron,  $\Psi_f$  and  $\Psi_i$  are the final and initial states wave functions respectively, which can be written as

$$\begin{cases}
\Psi_i(\mathbf{k}_i, \mathbf{r}_0, \mathbf{r}_1) = \phi_p(\mathbf{k}_i, \mathbf{r}_0) \psi_{nlm}(\mathbf{r}_1) \\
\Psi_f(\mathbf{k}_s, \mathbf{k}_e, \mathbf{r}_0, \mathbf{r}_1) = \phi_c(\mathbf{k}_s, \mathbf{r}_0) \phi_c(\mathbf{k}_e, \mathbf{r}_1) C(\alpha_{01}, \mathbf{k}_{se}, \mathbf{r}_{01})
\end{cases}$$
(A.2)

with  $\phi_p(\mathbf{k_i}, \mathbf{r_1}) = (2\pi)^{-3/2} e^{i\mathbf{k_i}\mathbf{r_1}}$ ,  $\phi_c$  and  $C(\alpha_{01}, \mathbf{k_{se}}, \mathbf{r_{01}})$  are coulomb wave and the post collision interaction term respectively:

$$\begin{cases}
\phi_c(\mathbf{k}, \mathbf{r}) = \frac{1}{(2\pi)^{3/2}} e^{\frac{\pi\alpha}{2}} \Gamma(1 - i\eta) e^{i\mathbf{k}\cdot\mathbf{r}} {}_1 F_1(i\eta, 1, i(kr - \mathbf{k} \cdot \mathbf{r})) \\
C(\alpha_{01}, \mathbf{k_{se}}, \mathbf{r_{01}}) = e^{\frac{-\pi\alpha_{01}}{2}} \Gamma(1 - i\alpha_{01}) {}_1 F_1(-i\alpha_{01}, 1, -i(k_{se}r_{01} + \mathbf{k}_{se} \cdot \mathbf{r_{01}}))
\end{cases}$$
(A.3)

where  $\eta = Z/k$ ,  $\alpha_{01} = Z_{01}/k_{se}$ , and  $\mathbf{k_{se}} = \frac{1}{2}(\mathbf{k_s} - \mathbf{k_e})$ . Thus, Eq.A.1 can be rewritten as

$$T_{if} = \langle \phi_c(\mathbf{k}_s, \mathbf{r}_0) \phi_c(\mathbf{k}_e, \mathbf{r}_1) C(\alpha_{01}, \mathbf{k}_{se}, \mathbf{r}_{01}) | -\frac{1}{r_0} + \frac{1}{r_{01}} | \phi_p(\mathbf{k}_i, \mathbf{r}_0) \psi_{nlm}(\mathbf{r}_1) \rangle$$

$$= \int \int \phi_c^*((\mathbf{k}_s, \mathbf{r}_0) \phi_c^*((\mathbf{k}_e, \mathbf{r}_1) C^*((\alpha_{01}, \mathbf{k}_{se}, \mathbf{r}_{01}) (-\frac{1}{r_0} + \frac{1}{r_{01}}) \phi_p(\mathbf{k}_i, \mathbf{r}_0) \psi_{nlm}(\mathbf{r}_1)$$
(A.4)

To get rid of the terms in  $\mathbf{r_{01}}$ , we apply the method of Kornberg and Miraglia where the Fourier transforms are used:

$$\begin{cases}
\phi(\mathbf{r}) = \frac{1}{(2\pi)^{\frac{3}{2}}} \int e^{i\mathbf{p}\mathbf{r}} \phi(\mathbf{p}) d\mathbf{p} \\
\phi(\mathbf{p}) = \frac{1}{(2\pi)^{\frac{3}{2}}} \int e^{-i\mathbf{p}\mathbf{r}} \phi(\mathbf{r}) d\mathbf{r}
\end{cases}$$
(A.5)

with using the Fourier transform scheme on the PCI term  $C(\alpha_{01}, \mathbf{k_{se}}, \mathbf{r_{01}})$ 

$$C^{*}(\alpha_{01}, \mathbf{k_{se}}, \mathbf{r_{01}}) = \frac{1}{(2\pi)^{3}} \int e^{i\mathbf{p}\mathbf{r}} \int e^{-i\mathbf{p}\mathbf{r}} C^{*}(\alpha_{01}, \mathbf{k_{se}}, \mathbf{r'_{01}}) d\mathbf{r'} d\mathbf{p}$$
(A.6)

Eq.(A.4) becomes

$$T_{if} = \frac{1}{(2\pi)^3} \int \int \phi_c^*((\mathbf{k_s}, \mathbf{r_0}) e^{i\mathbf{k_i r_0}} d\mathbf{r_0} \int \phi_c^*((\mathbf{k_e}, \mathbf{r_1}) \psi_{nlm}(\mathbf{r_1}) d\mathbf{r_1}$$

$$\times \int (2\pi)^{-3/2} e^{i\mathbf{p_r r_{01}}} \frac{C^*((\alpha_{01}, \mathbf{k_{se}}, \mathbf{r'_{01}})}{r'_{01}} d\mathbf{r'_{01}}$$

$$- \frac{1}{(2\pi)^3} \int \int \phi_c^*((\mathbf{k_s}, \mathbf{r_0}) \frac{e^{i\mathbf{k_i r_0}}}{r_0} d\mathbf{r_0} \int \phi_c^*((\mathbf{k_e}, \mathbf{r_1}) \psi_{nlm}(\mathbf{r_1}) d\mathbf{r_1}$$

$$\times \int (2\pi)^{-3/2} e^{i\mathbf{p_r r_{01}}} C^*(\alpha_{01}, \mathbf{k_{se}}, \mathbf{r'_{01}}) d\mathbf{r'_{01}}$$
(A.7)

by introducing two parameters  $\gamma \to 0$ , and  $\lambda \to 0$ , the matrix element  $T_{if}$  can be expressed as

$$T_{if} = \frac{1}{(2\pi)^3} \lim_{\substack{\lambda \to 0 \\ \gamma \to 0}} \int \left[ \int \phi_c^*(\mathbf{k}_e, \mathbf{r}_1) \psi_{nlm}(\mathbf{r}_1) d\mathbf{r}_1 \int \phi_c^*(\mathbf{k}_s, \mathbf{r}_0) e^{i(\mathbf{k}_i + \mathbf{p}) \cdot \mathbf{r}_0} e^{-\gamma r_0} d\mathbf{r}_0 \right]$$

$$\times \int (2\pi)^{-3/2} \frac{C^*(\alpha_{01}, \mathbf{k}_{se}, \mathbf{r}'_{01})}{r'_{01}} e^{i(\mathbf{k}_{01} - \mathbf{p}) \cdot \mathbf{r}'_{01}} e^{-i\mathbf{k}_{se} \cdot \mathbf{r}'_{01}} e^{-\lambda r'_{01}} d\mathbf{r}'_{01}$$

$$- \int \phi_c^*(\mathbf{k}_e, \mathbf{r}_1) \psi_{nlm}(\mathbf{r}_1) d\mathbf{r}_1 \int \frac{\phi_c^*(\mathbf{k}_s, \mathbf{r}_0)}{r_0} e^{i(\mathbf{k}_i + \mathbf{p}) \cdot \mathbf{r}_0} e^{-\gamma r_0} d\mathbf{r}_0$$

$$\times \int (2\pi)^{-3/2} C^*(\alpha_{01}, \mathbf{k}_{se}, \mathbf{r}'_{01}) e^{i(\mathbf{k}_{se} - \mathbf{p}) \cdot \mathbf{r}'_{01}} e^{-i\mathbf{k}_{se} \cdot \mathbf{r}'_{01}} e^{-\lambda r'_{01}} d\mathbf{r}'_{01} d\mathbf{r}'_$$

# **Electron-impact ionization of water molecules** at low impact energies

Cite as: J. Chem. Phys. 161, 164305 (2024); doi: 10.1063/5.0225885 Submitted: 27 June 2024 • Accepted: 4 October 2024 •







**Published Online: 22 October 2024** 









#### **AFFILIATIONS**

- <sup>1</sup> LPQSD, Department of Physics, Faculty of Sciences, University Sétif 1, Sétif 19000, Algeria
- <sup>2</sup>CRNA, 02, Boulevard Frantz Fanon, Boite Postale 399, Alger RP, Algeria
- <sup>3</sup>LPCT, UMR CNRS 7019, Université de Lorraine, 57000 Metz, France

#### **ABSTRACT**

The electron-impact ionization of water molecules at low impact energies is investigated using a theoretical approach named M3CWZ. In this model, which considers exchange effects and post-collision interaction, the continuum electrons (incident, scattered, and ejected) are all described by a Coulomb wave that corresponds to distance-dependent charges generated from the molecular target properties. Triple differential cross-sections for low impact energy ionization of either the 1b<sub>1</sub> or 3a<sub>1</sub> orbitals are calculated for several geometrical and kinematical configurations, all in the dipole regime. The M3CWZ model is thoroughly tested with an extensive comparison with available theoretical results and COLTRIMS measurements performed at projectile energies of E<sub>i</sub> = 81 eV [Ren et al., Phys. Rev. A 95, 022701 (2017)] and E<sub>i</sub> = 65 eV [Zhou et al., Phys. Rev. A 104, 012817 (2021)]. Similar to other theoretical models, an overall good agreement with both sets of measured data is observed for the angular distributions. Our calculated cross-sections' magnitudes are also satisfactory when compared to the other theoretical results, as well as to the cross-normalized relative scale data at 81 eV impact energy. The 65 eV set of data, measured on an absolute scale, offers a further challenging task for theoretical descriptions, and globally the M3CWZ performs fairly well and comparably to other theories. The proposed approach with variable charges somehow allows to capture the main multicenter distortion effects while avoiding high computational costs.

Published under an exclusive license by AIP Publishing. https://doi.org/10.1063/5.0225885

#### I. INTRODUCTION

Ionization of molecules by electron impact represents one of the most fundamental interactions in nature, whose interest is relevant to a wide range of applications. Kinematically complete (e, 2e) experiments, in which the energies and momenta of all final-state particles are determined, provide the most detailed information on the ionization reaction through the triple differential cross-section (TDCS). Compared to atoms, (e, 2e) studies have been more scarce for molecules. Experimentally, this is due to the difficulties related to the close spacing between electronic states, as well as to the contributions of rotational and vibrational states. Theoretically, the quantal description of multicenter continuum states is quite challenging. This said, during the last decades, there has been significant experimental progress that stimulated the development of powerful theoretical models. Measurements of TDCS have been reported for small molecules<sup>1-4</sup> and gradually for more complex ones.<sup>5</sup>

Molecules of biological interest have, in particular, become privileged targets in several strategic fields, from fundamental science to technological applications in medicine. In biological media, for example, it is established that the production of low-energy electrons is responsible for much of the damage to DNA in living tissue.<sup>12</sup> In the majority of track structure simulations, the focus is on water as the primary species in the system. In addition to the biological interest, the interaction between electrons and water molecules is a topic in various fields such as plasma physics, radiation physics, and chemistry. 13-15 Thus, accurate electron-impact ionization crosssections are needed for all these practical applications; in the last 20 years, the great progress achieved in measuring accurate (e, 2e) TDCS has been complemented by the development of a handful of theoretical models.

At high impact energy, electron momentum spectroscopy (EMS) is a powerful technique for the study of atomic and molecular structure. Pioneered by Weigold and McCarthy<sup>16</sup> and performed

a) Author to whom correspondence should be addressed: s\_houamer@univ-setif.dz

under high-energy Bethe ridge conditions, the EMS has been used for many atoms and molecules, including H<sub>2</sub>O.<sup>17</sup> It is well established now that this technique can provide direct information on momentum densities of each electron bound in a molecule or look at spatial patterns of individual molecular orbital in momentum space; the ionization process is simple enough to be investigated by simple first-order models. 18 At lower impact energies, (e, 2e) experiments are used to study the ionization dynamics, and more comprehensive modeling of the process is needed; this category is usually characterized by asymmetric kinematics, where the outgoing electrons are detected at very different energies and the momentum transfer is small (e.g., see Ref. 19 and references therein). TDCS on the water molecule have been investigated in various asymmetric kinematics and selected geometrical configurations. 20,21 With the emergence of new instrumentations, more efficient measurements, with very high resolution, have become possible. The COLTRIMS reaction microscope (C-REMI) is an imaging device developed to perform (e, 2e) measurements with high efficiency; <sup>22–24</sup> with multicoincidence high-resolution momentum equipment, a nearly full solid angle TDCS collection is achieved. From the 3D pattern, one may simultaneously extract cuts in the scattering plane as well as out of the scattering plane, offering a more severe test for theory, and thus gaining further insight into the collision dynamics.

On the theoretical side, available models for molecules are based on perturbative treatments. Currently, the seemingly most powerful one to describe the electron-impact ionization of molecular targets is the M3DW (molecular three-body distorted waves) model.<sup>25</sup> It is based on a full distorted wave description of the continuum with an isotropic distorting potential and includes PCI (postcollision interaction), which is treated exactly at all orders of perturbation theory. In another recently developed model, called MCTDW (multicenter three-distorted-wave),26 the continuum wave functions are obtained as solutions of a multicenter potential but PCI is not treated exactly. These two theoretical models provide an overall fair description of differential ionization cross-sections on a number of molecules; however, they are computationally expensive.

In a previous publication,<sup>27</sup> some of the present authors reported an investigation of the (e, 2e) process on argon atom, using a model called 3CWZ. In this model, which includes PCI exactly, all the continuum electrons are described by Coulomb waves with variable charges that somehow manage to capture the effect of the atomic distortion potential. Such an approach offers the substantial advantage of obtaining the TDCS for any kinematics at a low computational cost. In this work, we extend the 3CWZ model to molecular targets, maintaining the same numerical advantage. The model, named M3CWZ, is tested here thoroughly with TDCS calculations on the 1b1 and 3a1 orbitals of the water molecule. We analyze recently reported sets of experiments performed at low impact energy, where the data cover nearly the  $4\pi$  solid angle: they are given on a relative scale (at 81 eV impact energy) and on an absolute scale (at 65 eV impact energy). Both cases correspond to the dipole regime, characterized by small momentum transfer. These low-energy kinematics represent, on the one hand, a stringent challenge for theory and, on the other hand, are of crucial practical interest for example in radiation damage in biological systems.

The paper is organized as follows. A description of the M3CWZ model and its implementation is outlined in Sec. II. The calculated TDCS, presented in Sec. III, are confronted with the measured data

and two other theoretical results. Finally, Sec. IV summarizes and concludes this work. Atomic units (a.u.) are used unless otherwise specified.

#### II. THEORY

The electron-impact ionization of water molecule, assumed to be in its ground state, is schematized as

$$e_i + H_2O \rightarrow H_2O^+ + e_1 + e_2,$$
 (1)

where  $e_i, e_1$ , and  $e_2$  represent the incident and the two outgoing (scattered and ejected) electrons with corresponding momentum  $\vec{k}_i$ ,  $\vec{k}_1$ , and  $\vec{k}_2$ , required to fulfill conservation laws.

For highly asymmetric kinematics, the outgoing electrons can be distinguished as one fast scattered and one slow ejected, so that exchange effects can be omitted. At low impact energy, this approach no longer holds, and exchange effects between scattered and ejected electrons have, therefore, to be included. The ionization of the target may also occur through a capture process,<sup>28</sup> whereby the incident electron is captured into a bound state while two initially bound electrons are ejected; this process is generally not considered in (e, 2e) theoretical studies at intermediate to high impact energies. Neglecting capture effects, the fourfold differential cross-section (4DCS) for a particular orientation of the molecule is then given by<sup>2</sup>

$$\sigma^{(4)} = \frac{d^4 \sigma}{d\Omega_{Euler} d\Omega_1 d\Omega_2 dE_1} = (2\pi)^4 \times \frac{k_1 k_2}{k_i} (|T_{dir}|^2 + |T_{exc}|^2 + |T_{dir} - T_{exc}|^2),$$
 (2)

with  $d\Omega_{Euler} = \sin \beta \ d\beta \ d\alpha \ d\gamma$ , where  $(\alpha, \beta, \gamma)$  are the usual Euler

In our approach, we make the frozen core and single active electron approximation for the initial molecular bound wave function  $\Phi_i(\vec{r}_1)$ . The direct  $(T_{dir})$  and exchange  $(T_{exc})$  transition amplitudes

$$T_{dir} = \left\langle \varphi_c^{Z_1(-)} \left( \vec{k}_1, \vec{r}_0 \right) \varphi_c^{Z_2(-)} \left( \vec{k}_2, \vec{r}_1 \right) \right.$$

$$\times \left. C \left( \alpha_{21}, \vec{k}_{21}, \vec{r}_{01} \right) \left| \frac{1}{r_{01}} - \frac{1}{r_0} \left| \varphi_c^{Z_i(+)} \left( \vec{k}_i, \vec{r}_0 \right) \Phi_i(\vec{r}_1) \right|, \quad (3)$$

$$T_{exc} = \left\langle \varphi_c^{Z_2(-)} \left( \vec{k}_1, \vec{r}_1 \right) \varphi_c^{Z_1(-)} \left( \vec{k}_2, \vec{r}_0 \right) \right. \\ \times \left. C \left( \alpha_{21}, \vec{k}_{21}, \vec{r}_{01} \right) \left| \frac{1}{r_{01}} - \frac{1}{r_0} \left| \varphi_c^{Z_i(+)} \left( \vec{k}_i, \vec{r}_0 \right) \Phi_i(\vec{r}_1) \right|,$$
(4)

where  $\varphi_c^{Z(+)}$  and  $\varphi_c^{Z(-)}$ , respectively, represent the incoming and outgoing Coulomb waves given by  $^{30}$ 

$$\varphi_c^{Z(+)}(\vec{k}, \vec{r}) = \frac{\exp\left(i\vec{k} \cdot \vec{r}\right)}{(2\pi)^{3/2}} {}_{1}F_{1}(i\alpha(r), 1, i(kr - \vec{k} \cdot \vec{r}))$$

$$\times \exp\left(\frac{\pi\alpha(r)}{2}\right)\Gamma(1 - i\alpha(r)), \tag{5}$$

$$\varphi_c^{Z(-)}(\vec{k}, \vec{r}) = \frac{\exp\left(i\vec{k} \cdot \vec{r}\right)}{(2\pi)^{3/2}} {}_{1}F_{1}(-i\alpha(r), 1, -i(\vec{k} \cdot \vec{r} + kr))$$

$$\times \exp\left(\frac{\pi\alpha(r)}{2}\right)\Gamma(1 + i\alpha(r)), \tag{6}$$

with  $\alpha(r) = \frac{Z(r)}{k}$  being the Sommerfeld parameter; the variable charge function Z(r) is  $Z_i(r)$ ,  $Z_1(r)$ , or  $Z_2(r)$  according to which electron wave function (incident, scattered, or ejected) one is describing. The details about how these variable charges are obtained for the ionization of a given molecular orbital will be given below.  $C(\alpha_{21}, \vec{k}_{21}, \vec{r}_{01})$  is the final state projectile-ejected electron interaction, the so called PCI, written as

$$C(\alpha_{21}, \vec{k}_{21}, \vec{r}_{01}) = \exp\left(-\frac{\pi\alpha_{12}}{2}\right)\Gamma(1 - i\alpha_{12}) \times {}_{1}F_{1}(-i\alpha_{21}, 1, -i(\vec{k}_{21}.\vec{r}_{01} + k_{21}r_{01})),$$
(7)

where  $\vec{k}_{21} = \frac{1}{2} (\vec{k}_2 - \vec{k}_1)$  and  $\alpha_{21} = \frac{1}{2k_{21}}$ , and  $\vec{r}_{01} = \vec{r}_0 - \vec{r}_1$  is the projectile-electron vector.  $_1F_1$  is a confluent hypergeometric function, while  $\Gamma$  is the Gamma function.  $^{31}$ 

For the initial molecular bound wave function of the target, in this study, we use Moccia's molecular orbitals expanded on a set of Slater-type orbitals centered on the oxygen atom.<sup>32</sup> The use of singlecenter wave functions for molecules of type XHn centered on atom X is fairly justified because of the light hydrogen mass (for more details, we refer to Refs. 33-35). The quality of the molecular orbitals for H<sub>2</sub>O can be assessed by comparing some ground-state properties as calculated by Moccia<sup>32</sup> to the values reported by NIST:<sup>36</sup> Moccia's first ionization potential 0.4954 a.u. is close to the reference 0.463 a.u. value;<sup>36</sup> the dipole moment 0.8205 a.u. differs by about 12% with the reference 0.730 value<sup>36</sup> (Ref. 37); the H-O bond length 1.814 a.u. and H-O-H bond angle 106°32′ agree fairly well with the values 1.809 a.u. and 104°48′36 (Ref. 38). Furthermore, the accuracy of these molecular orbitals has been probed previously through an EMS study:<sup>33</sup> the observed good agreement with experimental TDCS was similar to that obtained with an orbital expanded over more than 100 Gaussian-like terms.1

To compare with the experimental data obtained with randomly oriented molecules, we need to integrate the TDCS over all Euler angles,

$$\sigma_{molecule}^{(3)} = \frac{1}{8\pi^2} \int \sigma^{(4)} d\Omega_{Euler}.$$
 (8)

Within our theoretical framework, this integration is carried out analytically (e.g., see Ref. 33 for more details). As a consequence, in our approach, the TDCS for one emission angle (one point in the angular distributions) is obtained in a few hours: this makes the proposed method very convenient to study the (e, 2e) dynamics for molecular targets. The evaluation of the transition amplitudes (3) and (4) makes use of the Fourier transform formalism, which greatly simplifies the different intermediate calculation steps (e.g., see Ref. 34 and references therein).

The variable charge Z(r) is evaluated analytically by using the spherically averaged potential,

$$U_i(r_1) = \frac{1}{4\pi} \int V_i(\vec{r}_1, \vec{R}_i) d\Omega_1 = -\frac{Z(r_1)}{r_1},$$
 (9)

where  $V_i(\vec{r}_1, \vec{R}_i)$  is taken here to be the standard Hartree potential (or static potential) defined for molecules by

$$V_i(\vec{r}_1, \vec{R}_i) = -\sum_{N=1}^{M} \frac{Z_N}{|\vec{r}_1 - \vec{R}_N|} + \sum_{i=1}^{N_0} N_{ij} \int \frac{|\varphi_j(\vec{r})|^2}{|\vec{r} - \vec{r}_1|} d\vec{r}, \qquad (10)$$

with  $N_0$  being the number of occupied orbitals,  $N_{ij}$  being the number of electrons in the orbital, M being the number of nuclei,  $Z_N$  being their charges, and  $R_N$  being their positions with respect to the molecular center of mass, which is approximately the oxygen atom for  $H_2O$ ;  $\varphi_j(\vec{r})$  are the molecular orbitals that describe the target. In this work, as we are using  $N_0 = 5$  molecular orbitals centered on the oxygen atom, Eq. (10) reads explicitly:

$$V_{i}(\vec{r}_{1}, \vec{R}_{1}, \vec{R}_{2}) = -\frac{8}{r_{1}} - \frac{1}{|\vec{r}_{1} - \vec{R}_{1}|} - \frac{1}{|\vec{r}_{1} - \vec{R}_{2}|} + \sum_{j=1}^{5} N_{ij} \int \frac{|\varphi_{j}(\vec{r})|^{2}}{|\vec{r} - \vec{r}_{1}|} d\vec{r},$$
(11)

where  $R_1$  and  $R_2$  are the bond lengths for  $H_2O$  ( $R_1 = R_2 = 1.814$  a.u.). The spherically averaged potential (9) has been widely used in modeling the interaction between the continuum electrons and the molecular core (e.g., see the ionization studies of  $H_2O$ ,  $NH_3$ , and  $CH_4$  by the impact of photons,  $^{39-42}$  electrons,  $^{39,40,43}$  or ions  $^{44}$ ).

As indicated in a previous work<sup>27</sup> for the argon atom, the variable charge felt by the continuum electrons is Z = N at the center of the target, and asymptotically either Z = 1 (for the outgoing electrons) or Z = 0 (for the incident electron). The difference is that the model is applied here for molecules through Eqs. (9) and (10); from the spherical potential obtained for a given molecular orbital, we obtain the variable charges, called  $Z_i(r)$ ,  $Z_1(r)$ , and  $Z_2(r)$ , attributed to the incident, scattered, and ejected electron wave function, respectively. The incident electron feels the field induced by all ten electrons of the neutral H<sub>2</sub>O molecule, and the corresponding charge is  $Z_i(r)$ . On the other hand, the scattered and ejected electrons move in the field of the residual ion H<sub>2</sub>O<sup>+</sup>, where only nine electrons contribute to the potential, inducing variable charges  $Z_1(r)$  and  $Z_2(r)$ , with  $Z_1(r) = Z_2(r)$ . Expressions of the variable charges  $Z_1(r)$  and  $Z_2(r)$  in the exit channel depend on the ionized orbital.

In Fig. 1, we present the variable charges used in the present model for the ionization of the 1b1 orbital of H2O (the figure is similar for the  $3a_1$  orbital). The charge decreases from Z=8 at r=0to an asymptotic value of Z = 1 for the outgoing electrons  $[Z_1(r)]$ and  $Z_2(r)$ , and to Z=0 for the incident electron  $[Z_i(r)]$ . Near r = R = 1.814 a.u., where R is the bond length of the molecule, the positive charge of the hydrogen nucleus generates a small kink—a feature obviously not observed in the case of atomic targets. The validity of using a variable charge approach in a 3 C waves model has been discussed and justified in previous publications. <sup>27,45</sup> The model, in which the PCI is treated exactly and accounted to all orders of perturbation theory, developed here for H<sub>2</sub>O (and similarly for other molecules XH<sub>n</sub> with a heavy center) is called M3CWZ. In Sec. III, its soundness is thoroughly tested by comparing the calculated TDCS with recent experimental data for low impact energies, and for several kinematical and geometrical arrangements corresponding to the dipole regime; the analysis is completed with a comparison with two other theoretical approaches, namely, the M3DW and the MCTDW,

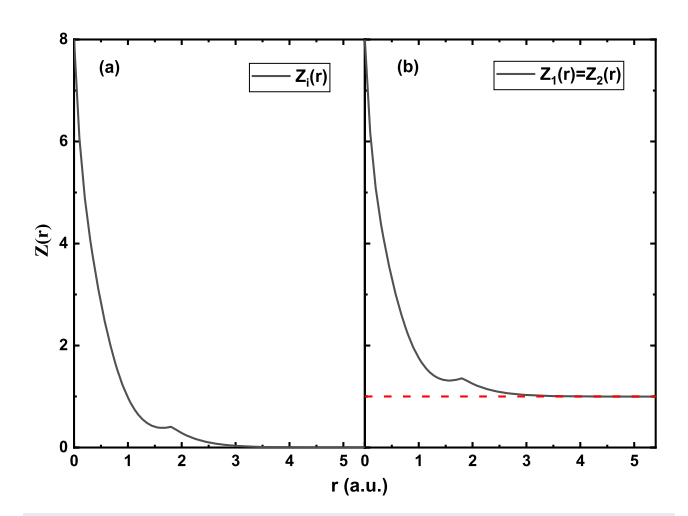


**FIG. 1.** Variable charge Z(r) felt by (a) the incident electron and (b) the outgoing electrons during the ionization process for the  $1b_1$  molecular orbital of  $H_2O$ .

which are currently the best available theories to study molecular ionization.

#### III. RESULTS AND DISCUSSION

A water molecule consists of five molecular orbitals which, classified in the ascending order of binding energies, are 1a1, 2a1, 1b<sub>2</sub>, 3a<sub>1</sub>, and 1b<sub>1</sub>. In this study, we investigate the electron-impact ionization TDCS for a projectile energy of either 81 eV (measurements published in Ref. 46) or 65 eV (measurements published in Ref. 47). The ionization of one of the two highest orbitals 1b<sub>1</sub> and  $3a_1$  leads to the stable cation  $H_2O^+$ , which does not dissociate. Since the binding energies of 1b<sub>1</sub> and 3a<sub>1</sub> are, respectively, 12.6 and 14.7 eV and the energy resolution in the experiments is about 2.5 eV, these orbitals are not resolved. For a meaningful comparison with measured data, we present an equal weight sum of the TDCS corresponding to the two molecular orbitals (as done in Refs. 26 and 46). Both measurements were performed with the COLTRIMS reaction microscope (C-REMI); by achieving a nearly  $4\pi$  collection solid angle, TDCS were obtained in three-dimensional space for several kinematic arrangements (ejected energies  $E_2$  and scattering angles  $\theta_1$ ). Measurements at low impact energies provide a strong test of theoretical models and our understanding of the processes involved in the reaction.

First, we examine the experiences performed at 81 eV impact energy:  $^{46}$  3D images of the TDCS have been measured as a function of the emission solid angle  $\Omega_2=(\theta_2,\varphi_2)$  for scattering angles  $\theta_1=6^\circ$  or  $10^\circ$ , and ejected energies  $E_2=5$  or 10 eV. To make the comparison with the data more comprehensive, three cuts of the 3D TDCSs are presented in three orthogonal planes, namely, the scattering xz plane, the half perpendicular yz plane, and the full perpendicular xy plane.

Our numerical TDCSs are displayed in Fig. 2 and compared with the measured data<sup>46</sup> and the results calculated with the MTCDW and M3DW models, as presented in Ref. 26. We recall here that M3DW treats the PCI exactly, whereas within the MCTDW approach, the PCI is modeled by a simple multiplicative Gamov

factor. Since the measured data are on a relative scale, here, the TDCSs are internormalized across all measured ejection energies as well as scattering angles. In other words, a single common factor is used to fix the relative magnitude of the data and theoretical results. The global scaling factor is obtained by achieving a good visual fit of the data and the M3CWZ results in the full perpendicular xy plane at  $\theta_1$  = 10° and  $E_2$  = 10 eV, according to the choice already made in Ref. 46. This scaling factor is found to be 0.285 and is subsequently applied to the three orthogonal planes in all other kinematics, all experiments are thereby consistently cross-normalized to each other.

In the full xy plane (Fig. 2, left-hand column), the observed angular distributions are overall well reproduced by the M3CWZ model, the best agreement being observed in Fig. 2(d) for  $\theta_1 = 10^{\circ}$ and  $E_2 = 10$  eV. Although no firm statement can be made about the magnitude agreement, once internormalized, the measured data and our theoretical results present an overall agreement that can be considered acceptable. When we compare our TDCS with those obtained with the MCTDW and M3DW models, the situation is rather mixed: in most cases, our results show a better agreement with the measured data except for the kinematics of Fig. 2(b), where the MCTDW shape looks better. For the case of Fig. 2(d), the M3CWZ model reproduces the data in an almost similar way to MCTDW, while the M3DW relatively underestimates the TDCS significantly in the regions of emission angle from  $0^{\circ}$  to  $60^{\circ}$  and from  $250^{\circ}$  to  $360^{\circ}$ . Concerning the absolute scale, the three theoretical calculations are of the same order of magnitude (the largest difference being a factor of about 1.5); our results are closer to those of the M3DW model at an ejection energy  $E_2 = 5 \text{ eV}$  [Figs. 2(a) and 2(b)], and to those of the MCTDW model for  $E_2 = 10 \text{ eV}$  [Figs. 2(c) and 2(d)].

In the scattering xz plane (Fig. 2, middle column), in all four kinematical arrangements, the experimental data exhibit features of binary and recoil lobes, a characteristic of dipole regimes. In these regimes, the momentum transfer  $\vec{K} = \vec{k_i} - \vec{k_1}$  is rather small (in our case,  $K \approx 0.37 - 0.54$  a.u.): as a consequence, the residual ion strongly participates in the collision dynamics and backscatters elastically the ejected electron in the direction opposite to that of the momentum transfer. Furthermore, it has been already pointed out in Ref. 46 that non-first-order effects in the electron-target interaction are present since the observed binary peaks are shifted with respect to the direction of the momentum transfer  $\vec{K}$ ; one such effect is included in our modeling via the PCI to all orders of perturbation theory. One first observation of the figure is that the M3CWZ model exhibits a strong recoil peak in all kinematics, in quite good agreement with experiments. Furthermore, the binary region is fairly well reproduced except for Fig. 2(f), corresponding to  $\theta_1 = 10^{\circ}$  and  $E_2 = 5$  eV, for which the ratio of the binary to recoil heights is underestimated. When a comparison is made between M3DW and MCTDW models, it is clearly seen that the latter features larger recoil peaks. Keeping in mind the way the measured data are internormalized, we may state that they overestimate the recoil with respect to the binary region. A notable difference between the three models appears in the binary region: the M3DW presents a double binary peak in all kinematics, the M3CWZ only in the kinematics of Fig. 2(f), and the MCTDW in none of the four configurations.

In the half perpendicular yz plane (Fig. 2, right-hand column), we first notice that the data are symmetric about  $\theta_2 = 180^{\circ}$ , with two symmetric maxima located close to  $\theta_2 = 90^{\circ}$  and  $\theta_2 = 270^{\circ}$ .

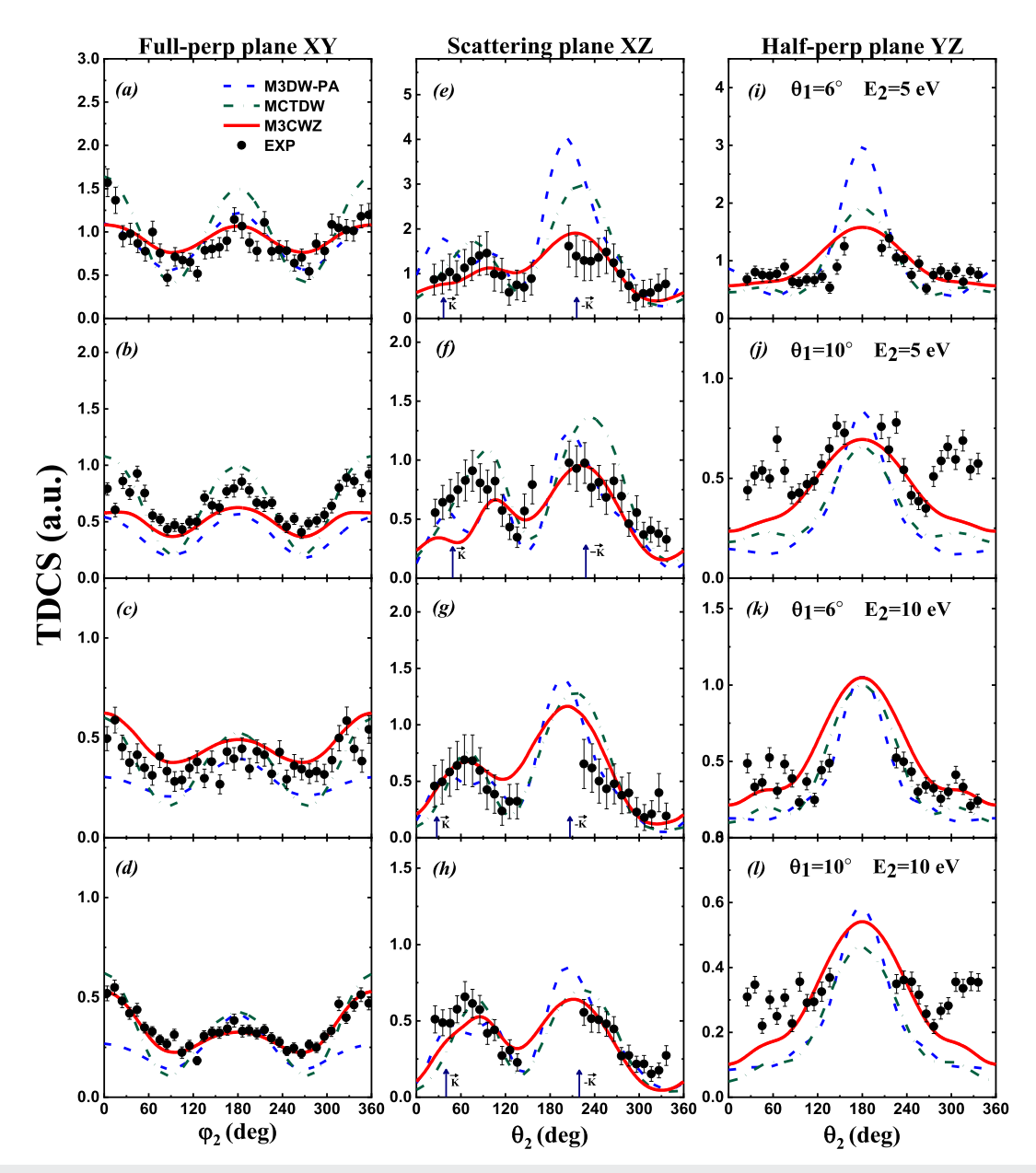


**FIG. 2.** Summed TDCS (presented as cuts of the 3D image) for the ionization of  $1b_1$  and  $3a_1$  orbitals of  $H_2O$  as a function of the ejection angle at 81 eV impact energy. The projectile is scattered at angles  $\theta_1 = (6^{\circ} \text{ or } 10^{\circ})$  in coincidence with the ejected electron with  $E_2 = (5 \text{ or } 10 \text{ eV})$ . Left-hand column: In the full perpendicular (xy) plane. Middle column: In the scattering (xz) plane. Right-hand column: In the half perpendicular (yz) plane. Theoretical results are red solid line (M3CWZ), blue dashed line (M3DW as rescaled in Ref. 26), and green dashed-dotted line (MCTDW).<sup>26</sup> The cross-normalized (see text) experimental data are black circles taken from Ref. 46. In the middle column (scattering plane), the direction of the momentum transfer  $\vec{K}$  and its opposite direction  $-\vec{K}$  are both indicated by an arrow.

The M3CWZ calculations reproduce overall quite well the TDCS shapes; we also have a reasonable agreement in relative magnitudes at a scattering angle  $\theta_1 = 6^{\circ}$  [Figs. 2(i) and 2(k)], while for  $\theta_1 = 10^{\circ}$ , [Figs. 2(j) and 2(l)] the data are somewhat underestimated in the regions of low or high emission angles. In addition, the comparison with M3DW and MCTDW calculations indicates that the three theoretical models predict practically the same TDCS shapes

and magnitudes except for  $\theta_1 = 6^{\circ}$  and  $E_2 = 5$  eV [Fig. 2(i)], where M3DW overestimates substantially the two other models in the central part (from 120° to 220°).

To summarize the results presented in Fig. 2, one can state that the M3CWZ model is overall able to correctly reproduce the measured TDCS shapes at 81 eV impact energy in most kinematics. Moreover, it yielded relative peak heights and overall magnitudes

in the 12 considered configurations that match satisfactorily the internormalized experimental data. In the shape and magnitude comparison with the M3DW and MCTDW results, some common characteristics were observed. However, no definite and general trend could be identified since some specific features seem better described by one or the other of the three models, according to the considered cut and the kinematic configuration.

We now consider the second set of measurements, at 65 eV impact energy:<sup>47</sup> since these data are now provided on an absolute scale, the TDCS can be compared not only in shape but also in magnitude. This provides an even stronger test of the present M3CWZ or any other model. Like the first set of measurements (at 81 eV impact energy), the present kinematics are also characterized by fairly low momentum transfer (from 0.5 to 0.87 a.u.), and, thus, to the dipole regime. Figures 3–5, show the TDCSs in the scattering xz plane, the half perpendicular yz plane, and the full perpendicular xy plane, respectively.

Figure 3 displays the TDCS as a function of the polar ejection angle  $\theta_2$  in the scattering xz plane for several sets of

scattering angles ( $\theta_1 = 10^{\circ}, 15^{\circ}, \text{ and } 20^{\circ}$ ) and ejection energies  $(E_2 = 5, 10, \text{ and } 15 \text{ eV})$ . Our M3CWZ results are compared with experimental data as well as with the TDCS calculated with the M3DW and MCTDW-WM models.<sup>47</sup> We note that while the PCI is included and treated exactly within the M3CWZ and M3DW approaches, in MCTDW-WM, it is included approximately through the Ward-Macek factor. 48 Since this factor is well known to violate the normalization, it is thereby not recommended for comparison with absolute measurements. However, the MCTDW-WM model has been used to investigate ionization under these particular kinematics but with a scaling factor of 1.8 for the best visual agreement with the data (see Ref. 47 for more details); in other words, the MCTDW-WM is used only to test its ability to reproduce qualitatively the TDCS shape. It can be clearly observed in Fig. 3 that both experimental and theoretical TDCSs exhibit an important recoil peak in all cases. The three models yield rather similar shapes and magnitudes, except that M3DW calculations overestimate clearly M3CWZ and MCTDW-WM results from nearly 180° to 220° emission angle in the kinematics of Figs. 3(a)-3(e). In the binary region,

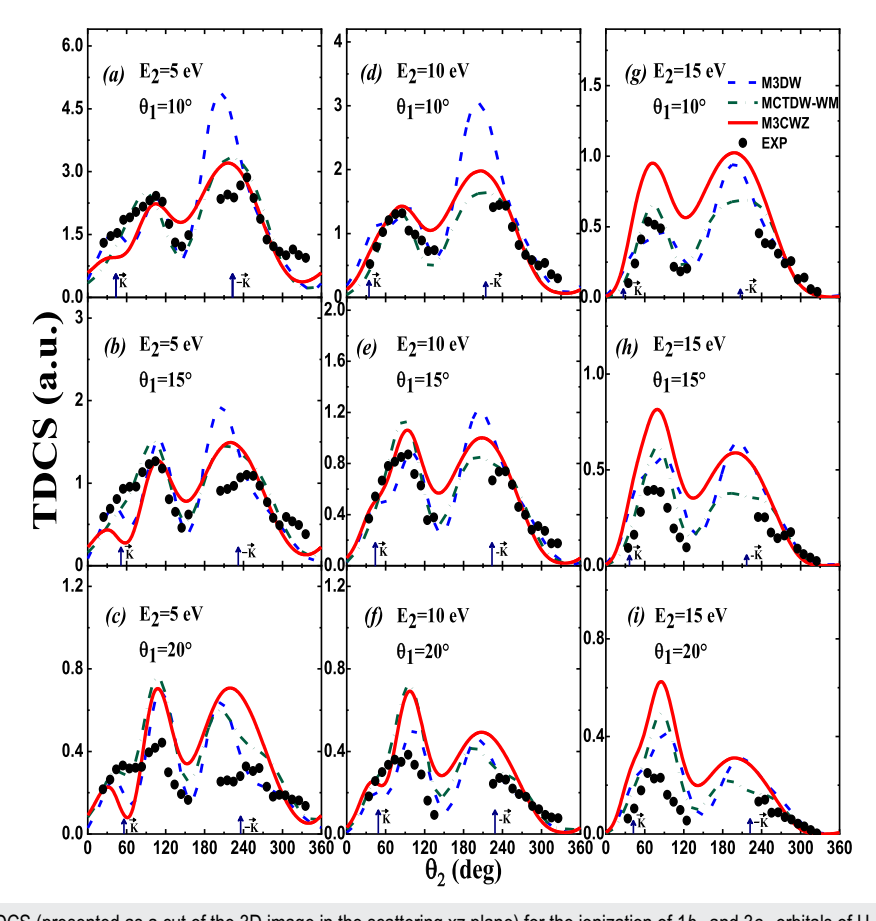
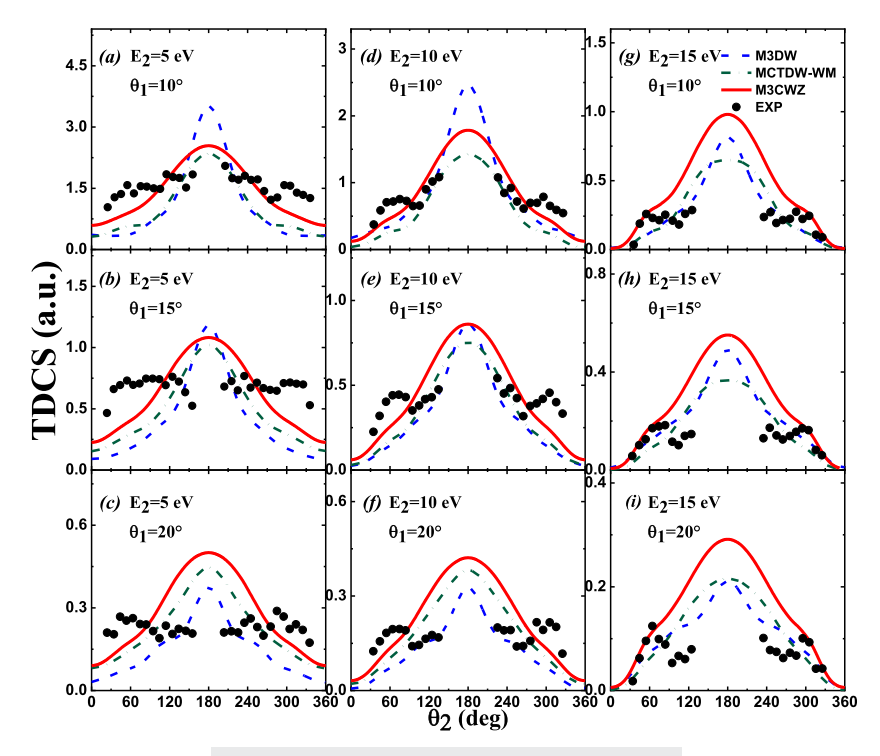
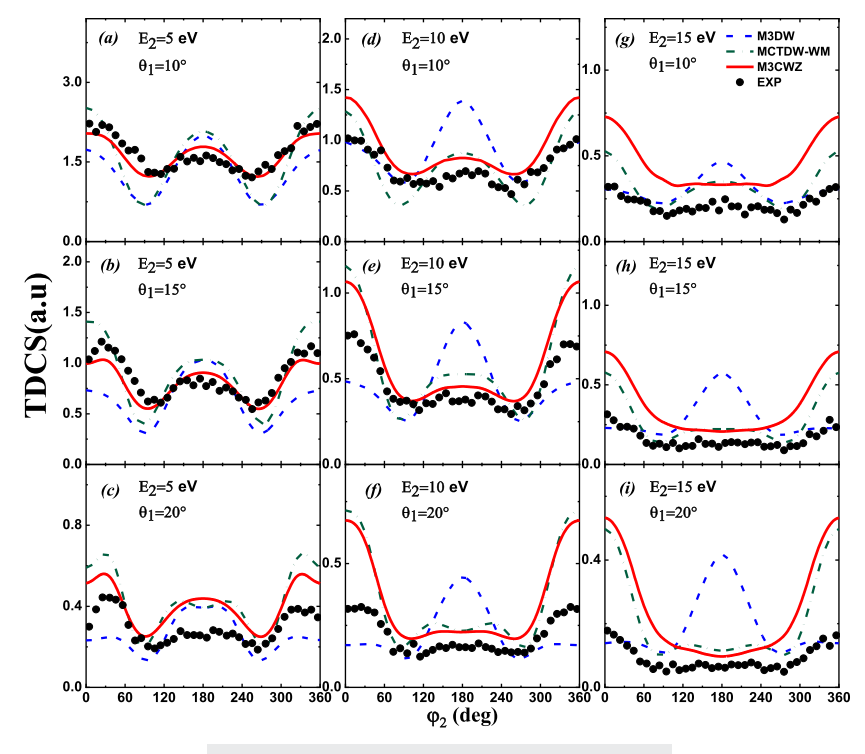


FIG. 3. Absolute summed TDCS (presented as a cut of the 3D image in the scattering xz plane) for the ionization of  $1b_1$  and  $3a_1$  orbitals of  $H_2O$  as a function of the ejection angle at 65 eV impact energy. The projectile is scattered at angles  $\theta_1 = (10^\circ, 15^\circ, \text{ or } 20^\circ)$  from top to bottom, respectively, in coincidence with the ejected electron with energies  $E_2 = 5$  eV (left-hand column),  $E_2 = 10$  eV (middle column), and  $E_2 = 15$  eV (right-hand column). Theoretical results are red solid line (M3CWZ), blue dashed line (M3DW), 47 and green dashed-dotted line (MCTDW-WM). 47 The absolute experimental data are black circles taken from Ref. 47. The direction of the momentum transfer  $\vec{K}$  and its opposite direction  $-\vec{K}$  are both indicated by an arrow.



**FIG. 4.** Same as Fig. 3 for the half perpendicular yz plane.



**FIG. 5.** Same as Fig. 3 for the full perpendicular xy plane.

the peak is strongly shifted with respect to the momentum transfer direction; for some kinematics, the M3CWZ and M3DW models feature a hint of double peak structure that is related to the pcharacter of the 1b1 and 3a1 orbitals; experimentally, this is not observed [at best we see a shoulder in Fig. 3(c)]. In terms of magnitude, the three theoretical models predict practically the same TDCS amplitude in the binary region at 5 and 10 eV ejection energies except for the kinematics of Fig. 3(f), where M3DW underestimates somewhat the two other models (noting anyway that we have kept the choice made in Ref. 47 in which MCTDW-WM calculations have been multiplied by the global factor 1.8). On the other hand, at 15 eV ejection energy, M3DW and MCTDW-WM results are in better agreement with the measured data than M3CWZ. To sum up, we can state that, in the scattering xz plane, the experimental data are overall better reproduced by M3CWZ and MCTDW-WM than by M3DW in the recoil region. In the binary region, all theoretical results seem to be quite similar except at 15 eV ejected energy where M3DW and MCTDW-WM are closer in magnitude to the experiments.

Figure 4 compares the TDCS in the half perpendicular yz plane. The first observation is that both the measured data and the theoretical results exhibit a symmetry about  $\theta_2 = 180^\circ$ . Unfortunately, the lack of experimental points around  $180^\circ$  ejection angle does not allow us to firmly confirm the presence of the clear and broad theoretical maximum; however, for Figs. 4(d) and 4(e), one may perceive a hint. Quantitatively speaking, the M3CWZ results overestimate slightly those of the MCTDW-WM model in all nine cases. When compared with M3DW, it is seen that, except for Figs. 4(a) and 4(d), the M3CWZ are rather close to the M3DW cross-sections although the latter present a sharper maximum in the region around  $\theta_2 = 180^\circ$ . The experimental data are somewhat well reproduced by the three models except at 5 eV ejection energy [Figs. 4(a)–4(c)]

where theories present a different angular distribution and substantially underestimate the experimental data for  $\theta_2 \le 100^{\circ}$  and  $\theta_2 \ge 250^{\circ}$ . Figure 5 shows the TDCS in the full perpendicular xy plane (corresponding to a fixed polar angle  $\theta_2 = 90^{\circ}$ ); here, the measured data cover nicely the whole range of azimuthal ejection angle  $\varphi_2$ . At 5 eV ejection energy [Figs. 5(a)–5(c)], the data exhibit up to three maxima. Of the three theoretical models, the M3CWZ appears to best reproduce the shape and magnitude, especially in the regions near  $\varphi_2 = 0^\circ$  and  $\varphi_2 = 360^\circ$ . At higher ejection energies  $E_2 = 10$  and 15 eV, the peak observed at  $\varphi_2 = 180^{\circ}$  for 5 eV progressively disappears and is replaced by a kind of a plateau in the region between  $\varphi_2 = 90^{\circ}$  and  $\varphi_2 = 250^{\circ}$ . The evolution in this angular domain is better reproduced by M3CWZ and somewhat by MCTDW-WM, while M3DW still yields a clear peak around  $\varphi_2 = 180^{\circ}$ . Outside this middle angular range, the M3CWZ and MCTDW-WM results are similar but seriously overestimate the measured data and also the M3DW calculations.

As for the 81 eV set of data, the theory–experiment comparison at 65 eV clearly shows that some TDCS features do not match, and no theoretical model achieves perfect agreement with the reported data in all configurations. Although simpler in its formulation, and with a lower computational cost, our M3CWZ model globally performs as well as the more sophisticated approaches M3DW and MCTDW.

Before summarizing the presented investigation, we would like to address two complementary issues concerning the proposed M3CWZ model.

The incident, scattered, and ejected electron wave functions are represented by Coulomb functions with variable charges obtained from the molecular properties. As shown in Fig. 1, they vary from Z=8 to Z=0 when describing the incident electron wave function and to Z=1 for the outgoing electrons. Another option consists

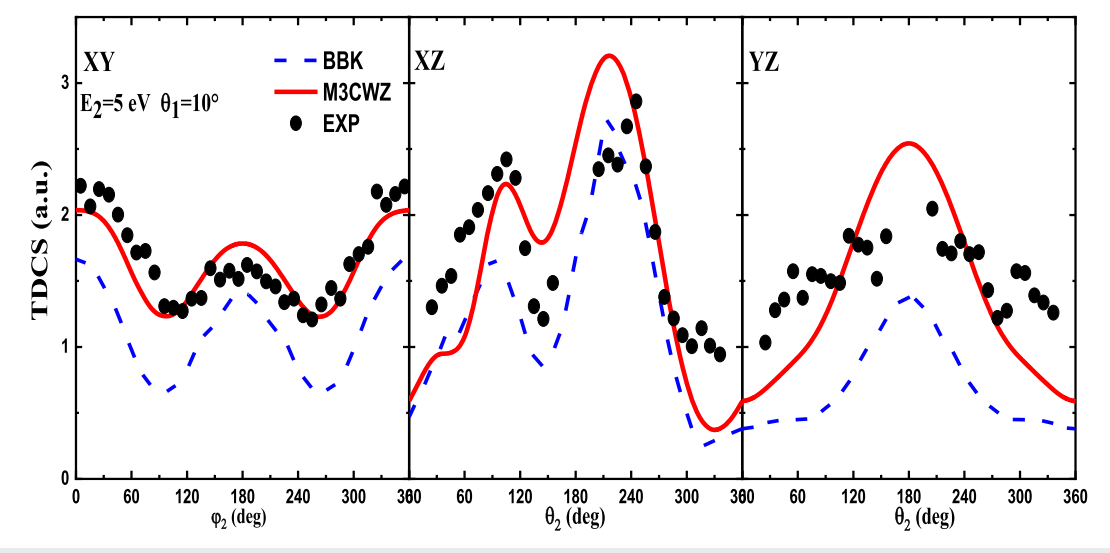


**FIG. 6.** Absolute summed TDCS for the ionization of  $1b_1$  and  $3a_1$  orbitals of  $H_2O$  as a function of the ejection angle at 65 eV impact energy. The projectile is scattered  $\theta_1 = 10^{\circ}$  in coincidence with the ejected electron with  $E_2 = 5$  eV. Left-hand column: in the full perpendicular (xy) plane. Middle column: in the scattering (xz) plane. Right-hand column: in the half perpendicular (yz) plane. Theoretical results are red solid line (M3CWZ) and dashed blue line (BBK). The absolute experimental data are black circles taken from Ref. 47

in using instead constant asymptotic charges (Z = 0 and Z = 1): the M3CWZ reduces then to the well-known BBK model.<sup>49</sup> A question arises: would such asymptotic charges be sufficient to produce acceptable TDCS angular distributions? The answer is negative. To show the importance of considering the molecular distortion, we present in Fig. 6 a comparison, on the absolute scale, at 65 eV impact energy for  $1b_1 + 3a_1$  orbitals<sup>47</sup> for  $E_2 = 5$  eV and  $\theta_1 = 10^{\circ}$ in the three orthogonal planes (xy, xz, and yz planes). It appears that, in all cases, the M3CWZ reproduces quite well in the experiments, while the BBK model underestimates both the M3CWZ results and the data. As already mentioned, such kinematics correspond to the dipolar regime for which it is known that the BBK manages to reproduce the shape but not the absolute magnitude. Outside this kinematical regime, the BBK model fails to reproduce the TDCS angular distribution, in particular, in the recoil region as illustrated for example in a previous work on the 3p orbital of atomic argon. 45 On the other hand, the variable charge scheme manages to describe quite well the TDCS shape. Whether for the atomic or the molecular case, the effectiveness of variable charges is, thus, even more visible when the residual ion plays a substantial role in the reaction.

Another interesting issue is to find whether the proposed M3CWZ model performs well also for the individual orbitals (i.e., 1b<sub>1</sub> and 3a<sub>1</sub> separately), for the inner orbitals, and for larger impact energies. For this specific purpose, but without making an extensive comparative study, we have considered the experiments performed at 250 eV impact energy, where the projectile is scattered at an angle  $\theta_1 = 15^{\circ}$  in coincidence with an ejected electron with energy  $E_2 = 10$  eV for the orbitals  $2a_1$ ,  $1b_2$ , and  $1b_1$ , and  $E_2 = 8$  eV for the 3a<sub>1</sub> orbital.<sup>20</sup> In these measurements, the momentum transfer is about 1.1 a.u.; all orbitals were resolved, and TDCSs have been measured—on a relative scale—for 1b1, 1b2, 3a1, and 2a1 orbitals separately. The calculated M3CWZ cross-sections are presented in Fig. 7, and compared to the experimental data normalized, in each panel, at the binary peak. While nothing can be stated about the absolute value, the shape agreement is overall good for the outer orbitals, while for the inner orbital (2a1), the recoil peak is not reproduced. As a matter of fact, the case of inner orbitals such as 2a<sub>1</sub> for H<sub>2</sub>O has been discussed in a previous publication:<sup>35</sup> the observed disagreement is attributed to the employed frozen core approximation in which the outer valence electrons are treated as part of the frozen core and are thus inactive. The study of inner

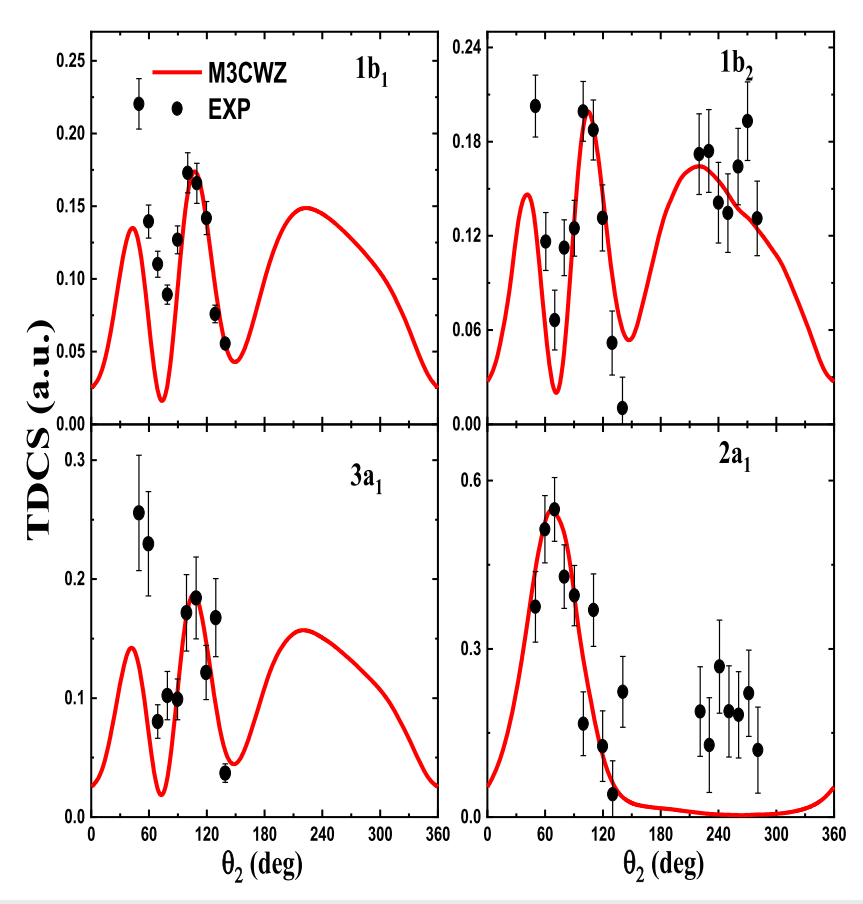


**FIG. 7.** TDCS for electron-impact ionization of molecular orbitals of  $H_2O$  at 250 eV impact energy. The projectile is scattered at an angle  $\theta_1 = 15^{\circ}$  in coincidence with the ejected electron with energy  $E_2 = 10$  eV (except for  $3a_1$  orbital where  $E_2 = 8$  eV). Theoretical results of M3CWZ model (red solid line) are compared with the relative scale measurements<sup>20</sup> normalized to the M3CWZ calculation in the binary region.

orbitals requires further treatment, beyond the frozen core approximation. No comparison with the M3DW and MCTDW models can be made since, as far as we know, no results have been published for such kinematics. An extensive comparison with other models is beyond the scope of the present manuscript. However, we can briefly and qualitatively compare with the TDCS obtained, e.g., with the complex Kohn<sup>50</sup> or the DS3C<sup>33</sup> (a BBK model with dynamic screening charges) approaches; also available are the less-sophisticated Coulomb-Born calculations in Refs. 33, 40, and 50. Note that in the Kohn or Coulomb approaches, the incident and scattered wave functions are described by plane waves, and exchange effects are ignored; the resulting TDCSs are necessarily symmetric with respect to the momentum transfer direction. In the DS3C and our M3CWZ calculations, this symmetry is broken. Concerning the TDCS magnitude, we observe in Ref. 33 that, for all four orbitals, the M3CWZ and DS3C models produce quite similar values. On the other hand, the magnitude obtained with the Kohn method,<sup>50</sup> is about 1.5 times larger than the M3CWZ result in the binary region, except for the 2a<sub>1</sub> orbital for which it is 2.5 smaller. From Fig. 7, we observe that the angular distributions for the 1b1 and 3a1, considered separately, are pretty similar both experimentally and within the M3CWZ model. For the 1b2 orbital, the M3CWZ model manages to produce an overall good shape, including a recoil peak as important as the binary one in agreement with the measured data; this feature is not observed, for example, in Ref. 50. On the other hand, for the inner orbital 2a<sub>1</sub>, the complex Kohn calculation manages to reproduce very well the angular distribution, with a very good agreement for the binary to recoil peak ratio; this may probably be attributed to an initial molecular state description, which is superior to Moccia's single-center wave function. The cases presented in Fig. 7 show that the M3CWZ model is also applicable to individual orbitals and kinematical situations other than those of the COLTRIMS data (at 81 and 65 eV incident energy) investigated in detail in this manuscript.

#### IV. SUMMARY

To summarize this work, a model called M3CWZ has been put forward and used to investigate the (e, 2e) reaction for the 1b1 and 3a<sub>1</sub> orbitals of the water molecule at low impact energies in a series of kinematical configurations. The model is based on a full Coulomb wave description with variable charges issued from the molecular target properties; it takes into account PCI and exchange effects. The proposed M3CWZ approach can be easily applied to any other molecule with a heavy center, once the variable charges are calculated from a spherically averaged potential associated with a given molecular orbital. The TDCSs calculated using this model have been compared to recent experiments obtained with a COLTRIMS reaction microscope (C-REMI), which can cover the full emission solid angle. The data are subsequently shown as cuts in three orthogonal planes enabling more insight into the ionization dynamics. Our results have also been compared to M3DW and MCTDW (or MCTDW-WM) models, which represent currently the best available theories for molecular ionization. In a first step, the TDCS has been calculated at 81 eV impact energy; in such kinematics, the experimental data have been internormalized across the measured scattering angles and ejected energies. Our calculations were found to correctly predict the experiments in most configurations, and they are overall at the same level of agreement when compared to M3DW and MCTDW models, and even better in certain cases. In a second step, at 65 eV impact energy, the situation is more challenging since the measured data are absolute. In this case, the MCTDW-WM model can be used only for comparison in TDCS shapes, the competition is then reduced between only the M3CWZ and M3DW models. The results show overall a reasonably good agreement between our theory and the data in shape and magnitude; the M3CWZ and M3DW models are globally equivalent (it is worth recalling that both treat PCI exactly). This means that, for water molecule at least, the Coulomb waves with adequate variable charges issued from a central potential somehow manage to describe reasonably the multicenter distortion effects of the molecular continuum. The main advantage of the M3CWZ approach is the low cost in computation time since one point is provided in a few hours instead of a few days for M3DW.

The present study suggests that further investigations in other kinematics and on other molecular targets should be carried out. From an experimental point of view, absolute measurements of TDCS provide the most stringent test. Theoretically, although they are not expected to change substantially the present results, it would be interesting to explore the role of the capture process in which the incident electron is captured into a molecular bound state and the two initially bound electrons are ejected into the continuum through a double ionization of the target. This entails, in the calculation of the fourfold differential cross-section (2), adding appropriately (see Ref. 28) a capture amplitude  $T_{capture}$  on top of the direct  $T_{dir}$ and exchange  $T_{exc}$  amplitudes. When the incident energy is relatively larger than the target bound state energies, this process is not expected to contribute significantly. Thus, capture effects are not considered in any of the theoretical approaches currently used to study (e, 2e) reactions. However, they could play a role especially should one go to lower incident impact energies.

Let us finish by noting that water molecule still attracts increasing attention due to its radiobiological importance. More realistic modeling are currently being developed where, for example, clusters of water molecules instead of single water molecule are investigated to estimate damage in living tissue.<sup>51</sup>

#### **ACKNOWLEDGMENTS**

This work was supported by the Direction Générale de la Recherche Scientifique et du Développement Technologique (DGRSDT-Algeria), PRFU (Grant No. B00L02UN190120200003).

#### **AUTHOR DECLARATIONS**

#### **Conflict of Interest**

The authors have no conflicts to disclose.

#### **Author Contributions**

**A. Tamin**: Software (lead); Visualization (lead). **S. Houamer**: Conceptualization (equal); Formal analysis (equal); Methodology (equal); Supervision (equal); Validation (equal); Writing – original draft (equal); Writing – review & editing (equal). **T. Khatir**: Software (equal); Visualization (equal). **L. U. Ancarani**: Writing – review &

editing (equal). **C. Dal Cappello**: Conceptualization (equal); Formal analysis (equal); Methodology (equal); Writing – review & editing (equal).

#### **DATA AVAILABILITY**

The data that support the findings of this study are available from the corresponding author upon reasonable request.

#### **REFERENCES**

- <sup>1</sup>K. Jung, D. Schubert, D. A. L. Paul, and H. Ehrhardt, J. Phys. B: At. Mol. Phys. 8, 1330 (1975).
- <sup>2</sup>L. Avaldi, R. Camilloni, E. Fainelli, and G. Stefani, J. Phys. B: At., Mol. Opt. Phys. 25, 3551 (1992).
- <sup>3</sup> J. Yang and J. P. Doering, *Phys. Rev. A* **63**, 032717 (2001).
- <sup>4</sup>S. Rioual, G. Nguyen Vien, and A. Pochat, Phys. Rev. A 54, 4968 (1996).
- <sup>5</sup>M. J. Hussey and A. J. Murray, J. Phys. B: At., Mol. Opt. Phys. **38**, 2965 (2005).
- <sup>6</sup>S. J. Cavanagh and B. Lohmann, J. Phys. B: At., Mol. Opt. Phys. **32**, L261 (1999).
- <sup>7</sup>L. Avaldi, R. Camilloni, and G. Stefani, Phys. Rev. A 41, 134 (1990).
- <sup>8</sup>L. G. Christophorou and J. K. Olthoff, J. Phys. Chem. Ref. Data **29**, 267 (2000).
- <sup>9</sup>X. Ren, T. Pflüger, M. Weyland, W. Y. Baek, H. Rabus, J. Ullrich, and A. Dorn, J. Chem. Phys. **142**, 174313 (2015).
- <sup>10</sup> E. Ali, X. Ren, A. Dorn, C. Ning, J. Colgan, and D. Madison, Phys. Rev. A 93, 062705 (2016).
- <sup>11</sup>S. Jia, J. Zhou, X. Wang, X. Xue, X. Hao, Q. Zeng, Y. Zhao, Z. Xu, A. Dorn, and X. Ren, Phys. Rev. A **107**, 032819 (2023).
- <sup>12</sup>B. Boudaiffa, P. Cloutier, D. Hunting, M. A. Huels, and L. Sanche, Science 287, 1658 (2000)
- <sup>13</sup>L. Campbell and M. J. Brunger, Plasma Sources Sci. Technol. 22, 013002 (2012).
- <sup>14</sup>E. Wang, X. Ren, W. Y. Baek, H. Rabus, T. Pfeifer, and A. Dorn, Nat. Commun. 11, 2194 (2020).
- <sup>15</sup>D. Ascenzi, E. Erdmann, P. Bolognesi, L. Avaldi, M. C. Castrovilli, R. Thissen, C. Romanzin, C. Alcaraz, I. Rabadan, L. Mendez, S. Diaz-Tendero, and A. Cartoni, Phys. Chem. Chem. Phys. 25, 24643 (2023).
- <sup>16</sup>I. E. McCarthy and E. Weigold, Phys. Rep. 27, 275 (1976).
- <sup>17</sup>A. O. Bawagan, C. E. Brion, E. R. Davidson, and D. Feller, Chem. Phys. **113**, 19 (1987).
- <sup>18</sup>Z. Rezkallah, S. Houamer, C. Dal Cappello, I. Charpentier, and A. C. Roy, Nucl. Instrum. Methods B 269, 2750 (2011).
- <sup>19</sup> A. Lahmam-Bennani, J. Phys. B: At., Mol. Opt. Phys. 24, 2401 (1991).
- <sup>20</sup> D. S. Milne-Brownlie, S. Cavanagh, B. Lohmann, C. Champion, P. A. Hervieux, and J. Hanssen, Phys. Rev. A 69, 032701 (2004).
- <sup>21</sup> C. Kaiser, D. Spieker, J. Gao, M. Hussey, A. Murray, and D. H. Madison, J. Phys. B: At., Mol. Opt. Phys. 40, 2563 (2007).

- <sup>22</sup> H. Schmidt-Böcking, J. Ullrich, R. Dörner, and C. L. Cocke, Ann. Phys. 533, 2100134 (2021).
- <sup>23</sup> X. Ren, A. Senftleben, T. Pflüger, A. Dorn, K. Bartschat, and J. Ullrich, Phys. Rev. A 83, 052714 (2011).
- <sup>24</sup>X. Ren, T. Pflüger, J. Ullrich, O. Zatsarinny, K. Bartschat, D. H. Madison, and A. Dorn, Phys. Rev. A 85, 032702 (2012).
- <sup>25</sup>J. Gao, D. H. Madison, and J. L. Peacher, J. Chem. Phys. **1232**, 204314 (2005).
- <sup>26</sup>M. Gong, X. Li, S. B. Zhang, S. Niu, X. Ren, E. Wang, A. Dorn, and X. Chen, Phys. Rev. A 98, 042710 (2018).
- <sup>27</sup> K. Bechane, S. Houamer, T. Khatir, A. Tamin, and C. Dal Cappello, Phys. Rev. A 109, 012812 (2024).
- <sup>28</sup> M. R. H. Rudge, Rev. Mod. Phys. **40**, 564 (1968).
- <sup>29</sup>D. H. Madison and O. Al-Hagan, J. At. Mol. Phys. **2010**, 367180.
- <sup>30</sup>L. D. Landau and E. M. Lifshitz, Quantum Mechanics: Non-relativistic Theory (Pergamon Press, Oxford, 1981), p. 570.
- <sup>31</sup>M. Abramowitz and I. A. Stegun, *Handbook of Mathematical Functions with Formulas, Graphs, and Mathematical Tables* (Dover, New York, 1972).
- <sup>32</sup>R. Moccia, J. Chem. Phys. **40**, 2186 (1964).
- <sup>33</sup>C. Champion, C. D. Cappello, S. Houamer, and A. Mansouri, Phys. Rev. A 73, 012717 (2006).
- <sup>34</sup> M. Chinoune, S. Houamer, C. D. Cappello, and A. Galstyan, J. Phys. B: At., Mol. Opt. Phys. 49, 205201 (2016).
- 35<sup>T</sup>. Khatir, S. Houamer, and C. Dal Cappello, J. Phys. B: At., Mol. Opt. Phys. 52, 245201 (2019).
- <sup>36</sup>See https://www.nist.gov/ for National Institute of Standards and Technology (NIST).
- <sup>37</sup>S. L. Shostak, W. L. Ebenstein, and J. S. Muenter, J. Chem. Phys. **94**, 5875 (1991).
- A. R. Hoy and P. R. Bunker, J. Mol. Spectrosc. 74, 1 (1979).
   C. M. Granados-Castro and L. U. Ancarani, Eur. Phys. J. D 71, 65 (2017).
- <sup>40</sup>C. M. Granados-Castro, "Applications of generalized Sturmian bases to molecular systems," Ph.D. thesis, Université de Lorraine, Metz, 2016.
- <sup>41</sup>C. M. Granados-Castro, L. U. Ancarani, G. Gasaneo, and D. M. Mitnik, Adv. Quantum Chem. 73, 3 (2016).
- <sup>42</sup> A. Ammar, L. U. Ancarani, and A. Leclerc, J. Comput. Chem. **42**, 2294 (2021).
- <sup>43</sup> A. Ammar, A. Leclerc, and L. U. Ancarani, Phys. Rev. A **109**, 052810 (2024).
- <sup>44</sup>L. Fernández-Menchero and S. Otranto, Phys. Rev. A 82, 022712 (2010).
- <sup>45</sup>M. Attia, S. Houamer, T. Khatir, K. Bechane, and C. D. Cappello, J. Phys. B: At., Mol. Opt. Phys. **56**, 075201 (2023).
- <sup>46</sup>X. Ren, S. Amami, K. Hossen, E. Ali, C. Ning, J. Colgan, D. Madison, and A. Dorn, Phys. Rev. A 95, 022701 (2017).
- <sup>47</sup>J. Zhou, E. Ali, M. Gong, S. Jia, Y. Li, Y. Wang, Z. Zhang, X. Xue, D. V. Fursa, I. Bray, X. Chen, D. Madison, A. Dorn, and X. Ren, Phys. Rev. A 104, 012817 (2021).
  <sup>48</sup>S. J. Ward and J. H. Macek, Phys. Rev. A 49, 1049 (1994).
- <sup>49</sup> M. Brauner, J. S. Briggs, and H. Klar, J. Phys. B: At., Mol. Opt. Phys. **22**, 2265 (1989).
- <sup>50</sup>C. Y. Lin, C. W. McCurdy, and T. N. Rescigno, Phys. Rev. A **89**, 012703 (2014).
- <sup>51</sup> Z. Alfaytarouni, P. A. Hervieux, C. Dal Cappello, G. Noel, and Z. El Bitar, Nucl. Instrum. Methods Phys. Res., Sect. B **549**, 165279 (2024).